Max-Planck-Institut
für Kohlenforschung

UNIVERSITÄT
DUISBURG
ESSEN

Offen im Denken

Investigation of a purely ionic device for electronic switching and amplification

Dissertation

Zur Erlangung des akademischen Grades

Doktor der Naturwissenschaften (Dr. rer. nat.)

vorgelegt an der Fakultät für Der Fakultät für Physik

der Universität Duisburg-Essen

von

Elalyaa Mohamed

aus Fayoum, Ägypten

Erstgutachter Priv.-Doz. Dr. Frank Marlow

Zweitgutachter: Prof. Dr. Ferdi Schüth

Tag der mündlichen Prüfung

09. Juli 2024

Die vorliegende Arbeit wurde am Max-Planck-Institut für Kohlenforschung in Mülheim an der Ruhr in der Arbeitsgruppe Nanostrukturen und Optische Materialien in der Abteilung für Heterogene Katalyse unter Anleitung von Herrn Priv.-Doz. Dr. Frank Marlow angefertigt.

Referent: Priv.-Doz. Dr. Frank Marlow

Korreferent: Prof. Dr. Ferdi Schüth

Hiermit versichere ich, die vorliegende Dissertation selbstständig, ohne fremde Hilfe und ohne Benutzung anderer als den angegebenen Quellen angefertigt zu haben. Alle aus fremden Werken direkt oder indirekt übernommenen Stellen sind als solche gekennzeichnet. Die vorliegende Dissertation wurde in keinem anderen Promotionsverfahren eingereicht. Mit dieser Arbeit strebe ich die Erlangung des akademischen Grades Doktor der Naturwissenschaften (Dr. rer. nat.) an.

Duisburg, den 15. 2. 2024

“I am among those who think that science has great beauty. A scientist in his laboratory is not only a technician; he is also a child place before natural phenomenon, which impress him like a fairy tale.”

- Marie Curie

Acknowledgment

First and foremost, I would like to express my gratitude to my supervisor Dr. Frank Marlow. I am deeply grateful for his advice, motivation, and support since the first day I am in the institute. Thank you for the guidance and the freedom you give me to do research as well as our regular talks about science and other things. I have learned a lot from you during my PhD and all that I learned I will cherish in the future. Thank you very much!

I am very thankful to my second supervisor Prof. Dr. Ferdi Schüth for the laboratories, equipment, and the support of the project

I would like to thank Prof. Dr. Axel Lorke for the discussions we had that helped me a lot. I thank Dr. Wolfgang Schmidt for the critical reading.

A big part of this thesis would be very difficult to achieve without the help of several people. I would like to thank Hendrik Köster for the help in the experimental parts especially the construction of the IVESTs. I thank Ursula Petrat for the support in the lab and part of the experimental work. I would like to thank Nico Tchorz for the help in the improvement of the building of the devices I used during this project. I thank the fine mechanics, workshop and especially Ralph Tomas for providing me with the required electronic parts to go on with this work.

I would like to thank all the former and current members of the Marlow group for such nice atmosphere, discussions, great time in the lab, and all the activities. Special thanks goes to Tillmann Koehler, Dr. Sabine Josten, Hendrik Köster, Ursula Petrat, Dr. Akilavasan Jeganathan, Dr. Marco Rehosek, Nico Tchorz, Lisanne Messmer, Stephen Peuleke and Michel Nunnenkamp.

I would like to thank all the members of Heterogeneous catalysis department for the nice atmosphere and activities.

I thank my family and friends for the emotional support they always give me, with special thanks to Papa, Mama, Abdu, Younis, Sara, Nada, Zahra, Lina, my grandparents, Aisha, and Leila. I want to express my heartfelt gratitude to my parents for believing in me, and their encouragement to follow this path.

Finally yet importantly, I would like to thank my husband Abdelrahman for his support, understanding and patience when the work got too much of my attention and time.

I am grateful for the financial support of the Erasmus+ program (KA1-Student mobility) of the European Commission in the beginning of the project.

Abstract

In this dissertation, a new iontronic device called Ionic Voltage Effect Soft Triode (IVEST) is reported and investigated. In the first part, the device was built with different construction methods. The device was constructed and characterized with intention to be based on interfacial ion adsorption and redox oxidizer depletion. The IVEST was built in a simple manner with no need for sophisticated or expensive materials. It does not utilize the control of a semiconducting channel, but an electrolyte. In different electrical circuit configurations, it can show amplification or memory effects. The device had an electrical current amplification reaching 52 and memory effects in the electrical resistance lasting for up to 6 h. These values were achieved by tuning the electrode interface, the electrolyte and diffusion properties.

In the second part, the IVEST was optimized, tuned and embedded into a memory application concept. The device is an electrochemical micro-cell, consisting of a top electrode and two bottom electrodes. The device controls the concentration and diffusion of ions by the voltage applied on the top electrode. The IVEST showed a memory effect lasting up to 6 hours. Despite the remarkably large stability time, the memory contrast was small in the first device versions. Now, we have increased the memory contrast by introducing a new external electrical circuit layout combined with a new operation protocol. The new investigation also reveals peculiarities of the memory and showed that the IVEST can be used in applications connected with memories. These iontronic memories show a secondary information storage connected with the read-out frequency.

In the third part, the IVEST was converted to an opto-ionic device. Opto-ionic devices have not been extensively studied yet, and there is a need for the production of more devices capable of converting optical signals to ionic signals. The ability of the IVEST to convert the optical signal to an ionic signal is explored. Additionally, we also refer to the characterization of the opto-IVEST, which can be applied in various applications. The opto-IVEST showed the ability to detect and memorize the optical signal. Furthermore, the device exhibited synaptic learning behavior and a hybrid logic gate (AND) function.

Zusammenfassung

In dieser Dissertation wird ein neues iontronisches Bauelement namens Ionic Voltage Effect Soft Triode (IVEST) vorgestellt und untersucht. Im ersten Teil wurde die Vorrichtung mit verschiedenen Konstruktionsmethoden gebaut. Das Bauelement wurde mit der Absicht konstruiert und charakterisiert, auf der Adsorption von Ionen an der Grenzfläche und der Verarmung von Redox-Oxidationsmitteln zu beruhen. Das IVEST wurde auf einfache Weise gebaut, ohne dass anspruchsvolle oder teure Materialien benötigt wurden. Er nutzt nicht die Kontrolle eines Halbleiterkanals, sondern eines Elektrolyten. In verschiedenen elektrischen Schaltkreiskonfigurationen kann es Verstärkungs- oder Speichereffekte aufweisen. Die Vorrichtung wies eine Stromverstärkung von bis zu 52 und Gedächtniseffekte beim elektrischen Widerstand auf, die bis zu 6 Stunden anhielten. Diese Werte wurden durch Abstimmung der Elektrodenschnittstelle, des Elektrolyten und der Diffusionseigenschaften erreicht.

Im zweiten Teil wurde das IVEST optimiert, abgestimmt und in ein Speicheranwendungskonzept eingebettet. Das Gerät ist eine elektrochemische Mikrozelle, die aus einer oberen Elektrode und zwei unteren Elektroden besteht. Das Gerät steuert die Konzentration und Diffusion von Ionen durch die an der oberen Elektrode angelegte Spannung. Die Vorrichtung zeigte einen Speichereffekt, der bis zu 6 Stunden anhielt. Trotz der bemerkenswert langen Stabilitätszeit war der Gedächtniskontrast in den ersten Versionen der Vorrichtung gering. Jetzt haben wir den Speicherkontrast durch ein neues externes elektrisches Schaltungslayout in Kombination mit einem neuen Betriebsprotokoll erhöht. Die neue Untersuchung deckt auch Besonderheiten des Speichers auf und zeigt, dass der IVEST in Anwendungen, die mit Speichern zusammenhängen, eingesetzt werden kann. Diese iontronischen Speicher weisen eine mit der Auslesefrequenz verbundene sekundäre Informationsspeicherung auf.

Im dritten Teil wurde das IVEST in ein opto-ionisches Bauelement umgewandelt. Opto-ionische Geräte sind noch nicht umfassend untersucht worden, und es besteht ein Bedarf an der Herstellung weiterer Geräte, die in der Lage sind, optische Signale in ionische Signale umzuwandeln. Die Fähigkeit des IVEST, das optische Signal in ein ionisches Signal umzuwandeln, wird erforscht. Außerdem wird auf die Charakterisierung des opto-IVEST eingegangen, das in verschiedenen Anwendungen eingesetzt werden kann. Das opto-IVEST

zeigte auch die Fähigkeit, das optische Signal zu erkennen und zu speichern. Darüber hinaus zeigte das Gerät ein synaptisches Lernverhalten und eine hybride Logikgatterfunktion (AND).

Contents

1. General Introduction

1.1 Iontronics

Iontronics is a wide concept of using ions to transmit, generate, store, and receive signals. It is a wide disciplinary connecting different research area like biology, electronics, electrochemistry, physics, and chemistry. After the invention of the conjugated polymer that won the Nobel Prize 2000, the word iontronic was used to explain the coupling of the ions and the electrons in the polymers turning them to a semiconductor material.[1] Iontronics then became widely known when it was introduced in 2011 in a book titled "Iontronics: Ionic Carriers in Organic Electronic Materials and Devices."[2] The mentioned book was concerned about organic electronics and using polymer in different electronic devices. In the beginning, the main idea of iontronics was to control electronic devices with ions. With time, the concept became wider, and recently, the attempts toward purely ionic devices are gaining more interest. [3] Purely ionic devices can be advantageous in avoiding semiconductors, such as silicon. In most devices, there is a need for semiconductor materials forming a channel for the charge carriers that requires sophisticated fabrication processes with high costs.[4, 5]

When we are talking about using ions to control signals, the first question that comes to mind is why? As electrons move faster than ions in the very most cases, iontronic devices are expected to be unable to match the speed of classical electronics. However, most of the biological systems in nature work with ions. The biological systems function by controlling biomolecules (such as proteins, nucleic acids, and phospholipids) at the nanoscale, from the human brain, the most complex and powerful creature that can carry many tasks more than any electronic device, to the small worm that can analyse sensoric signals and make decisions [6]. Many complex functions and sensing of the biological systems are made through ions. [7, 8] There must be a reason for nature's ultimate selection for ions in biological systems. Likely, this could be linked to the low-energy consumption.[9] Another attractive characteristic of the ions that they are heavier than electrons that they cannot be easily affected by electrical or magnetic noise. Ions have also variety regarding sizes, polarizabilities, and other properties. This makes ions able to build different and diverse devices.[10] Iontronic devices also hold

great potential for various applications due to their affordability, ability to interface with biological systems, and capacity to carry chemical information for the selective regulation of different functions and processes. Although electronic devices exhibit exceptional performance, they still have limitations when used as building blocks in neuromorphic devices and systems. [11] These limitations arise from the fact that electronic devices work with electrons, while biological systems work with ions. The different working principles create limitations in some applications, especially those connected with the human-machine interface. Since ions are the language of nature and nearly every biological system works with ions, mimicking biological systems with iontronic devices will have fewer limitations and may lead us to gain another aspect of understanding nature and biological systems. Figure 1.1 shows various interesting aspects that can be achieved with one iontronic device[12]. The tree shown in Figure 1.1 is based on the electric double layer transistor (EDLT), which is discussed in section 1.2.5. This device with its high carrier density, large capacitance, fluidity and high electric field was the base for inventing further related devices and discovering new concepts. .

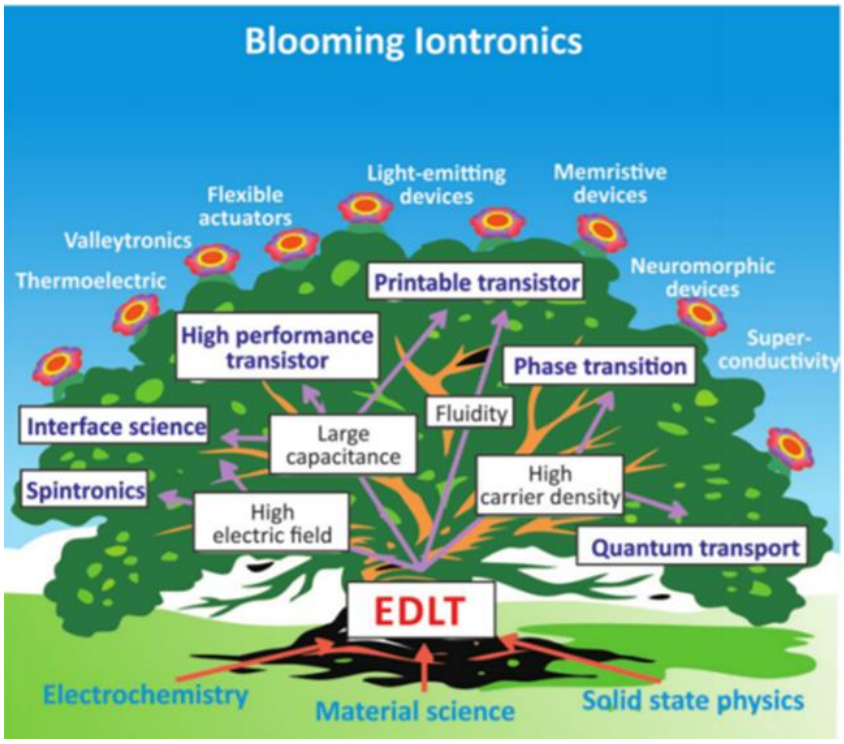

Figure 1.1 The interdisciplinary nature of ion-controlled electronics propels their progress into various realms of emerging science and practical applications, with some of these areas still awaiting full realization as described in ref. [12] This picture is based on the EDLT an important iontronic device. Copyright Wiley-VCH GmbH. Reproduced with permission

Beside the mentioned advantages, one important thing is that most of the iontronic devices are powered with low voltage in comparison to electronic devices. [3, 12] This highlights the potential impact of iontronics in addressing the energy security issue. With iontronic devices the energy consumption of the information-processing devices might be reduced and new technologies of generating and harvesting energy might be discovered based on iontronics.[13, 14]

1.2 Background

1.2.1 Redox couple electrolytes

In iontronics, electrolytes play the key role in the construction of many devices. Electrolytes are substances that contain both positive and negative ions. [15] When a salt is dissolved, it dissociates into anions and cations. The conductivity of an electrolyte depends on the diffusion of these ions. In this thesis, a redox couple electrolyte of triiodide/ iodide is used. The triiodide/ iodide electrolyte is preferable in dye sensitized solar cells (DSSCs) as it allows efficient and fast regeneration of the dye molecules, has a good solubility, adsorbs a minimal amount of light, has a tunable redox potential by changing the concentration of the solution and it is stable.[16, 17] This type of electrolyte is widely used in dye sensitized solar cells (DSSCs) where the idea of iontronics can be noted as the transportation of the charge is depending on the motion of the ions. In DSSCs, the charge transfer and the motion of the ions controls the energy conversion.[17] A redox shuttle is used to transfer electrons from the counter electrode to the oxidized dye as shown in Figure 1.2. When the dye adsorbs light, it moves form the ground state to an excited state. The excited dye then inject electrons into the conduction band of the titanium dioxide layer on the working electrode. These injected electrons diffuse from the working electrode through the external circuit to the counter electrode. On the counter electrode I_3^- is reduced to I^-. The ground state of the dye is regenerated by the acceptance of electrons from I^- ion redox mediator, and I^- is oxidized to I_3^-. Finally, the oxidized I_3^- diffuses towards the counter electrode and undergoes reduction to form I ions as shown in Eqn. 1.1.[18]

$$I_3^- + 2e \rightleftharpoons 3I^- \qquad (1.1)$$

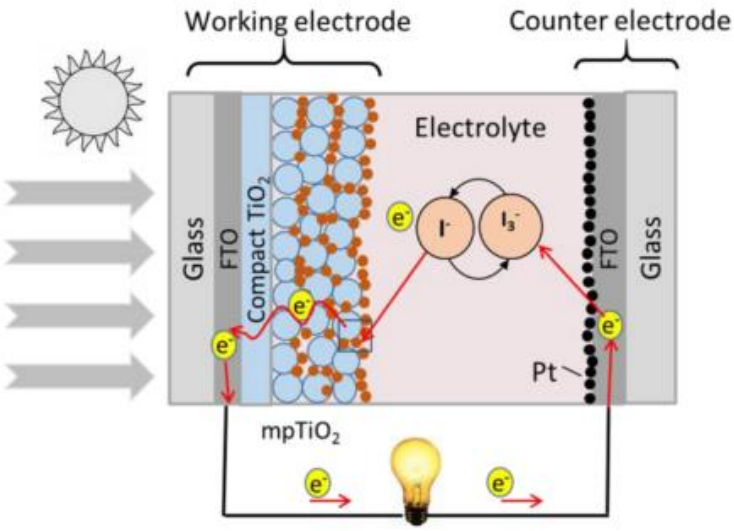

Figure 1.2 A DSSC with the redox couple electrolyte iodide/triiodide.[19] Copyright © [2020] IEEE

This electrolyte has many advantages like the chemical stability and the fast redox reaction.[20] Beside this it was well investigated and used many times in literature.[21, 22]

1.2.2 The Butler-Volmer Equation

One of the fundamental theories in electrochemistry related to the electrode interface is the Butler-Volmer theory[23]. Butler-Volmer theory describes the progress of electrochemical reactions. This theory provides a framework for understanding the reactions at electrode surfaces [24]. The Butler-Volmer equation describes the relation between the current passing through an electrode and the potential difference across it in an electrochemical system as shown in Eqn 1.2. [25] The equation consists of two terms, one for the forward reaction (oxidation) and one for the reverse reaction (reduction).

$$i = i_o \left\{ e^{\left[\frac{\alpha_a nF(E-E_0)}{RT}\right]} - e^{\left[\frac{-\alpha_c nF(E-E_0)}{RT}\right]} \right\} \qquad (1.2)$$

where i is the current density passing through the electrode, i_o is the exchange current density, α_a and α_c are the forward (anodic) and reverse (cathodic) transfer coefficients, E is the potential difference across the electrode in V, E_o is the equilibrium potential in V, n is the number of electrons involved in the reaction, F is Faraday's constant, R is the gas constant, and T is temperature in K.

The Butler-Volmer equation induces the S-shape of many *JV* curves and is used in many applications related to both research and industry. [26, 27]

1.2.3 Schottky junctions

When a metal comes in contact with a semiconductor, and the work function of the semiconductor material is less than the work function of the metal (φ_m) a Schottky junctions is created. Let us consider a junction formed between a metal and n-type semiconductor with work function (φ_n), as shown in Figure 1.3. The Fermi level of the semiconductor is higher than the metal. Electrons start to move to the conduction band (CB) of the metal leaving a positive charge in the semiconductor material. This positive charge on the semiconductor leads to a depletion region (W_D) and a band bending in the semiconductor.

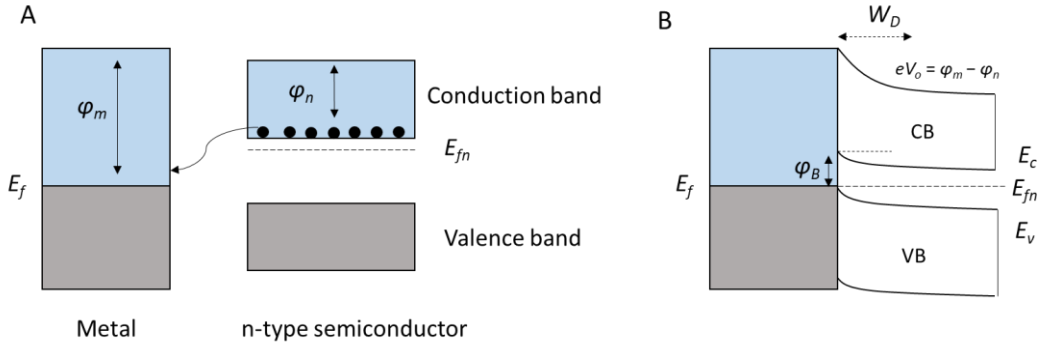

Figure 1.3 (A) Metal and n-type semiconductor energy levels before contact and (B) Schottky junction between the metal and the n-type semiconductor after contact. W_D is the width of the electronic depletion zone. Adapted from [28]

Once the junction is formed between the metal and the semiconductor, the Fermi level lines up. The resulting bending is in the direction of the electric field in the n-type semiconductor. Bands bend up going from n-type semiconductor to metal, as shown in Figure 1.3B. The built-in potential in the junction is the difference in the work functions (V_o) as shown in Figure 1.3B.

1.2.4 Electric double layers

The electric double layer EDL formation at the interface between two different materials is one of the important processes in iontronics. At small potential differences, the EDL acts as a capacitor with a big capacitance.[29] Beside the capacitance, it has the advantage of combining both the ionic and the electronic current in two unlike media. This combination of electronic and ionic media and using the EDL as an important process in iontronic devices can enable an ionic-electronic transducer and opens the door for a wide range of functionality and applications. [30-32] Helmholtz first proposed the idea of the electric double layer in 1853. He proposed that the electrode/electrolyte interface consists of two planes with equal but different charges. As the electrode is charged, the electrolyte tries to compensate these charges by

accumulating ions with opposite charge, forming the Helmholtz layer. The electric double layer model proposed by Helmholtz was then upgraded by Gouy and Chapman. They described the inhomogeneous distribution of different ions close to the electrode interface (Diffuse layer). Additionally, they employed the Poisson−Boltzmann theory as ions in the electric double layer are subjected to electrical and thermal fields. Stern combined the Gouy-Chapman model and Helmholtz model. He divided the electrolyte side into two parts. The first part is the part closer to the electrode called Stern layer or Inner Helmholtz layer .The second part is the inhomogeneous diffuse layer consisting of different types of ions as shown in Figure 1.4. [24, 33] In Stern's model the inner layer consists of ions, which are called specifically adsorbed ions, and solvent molecules. The plane which is going through the center of the specifically adsorbed ions is called inner Helmholtz plane (IHP). The outer layer in the solution is called diffuse layer where solvated ions both cations and anions are distributed. The plane which is going through the center of the solvated ion which is the closest to the electrode is called outer Helmholtz plane (OHP).[24]

Then the capacitance of the EDL (C_{dl}) consists of the series circuit of two capacitances the inner Helmholtz layer capacitance (C_H) and the diffusion layer capacitance (C_{diff}) as described in Eqn 1.3.

$$\frac{1}{C_{dl}} = \frac{1}{C_H} + \frac{1}{C_{diff}} \qquad (1.3)$$

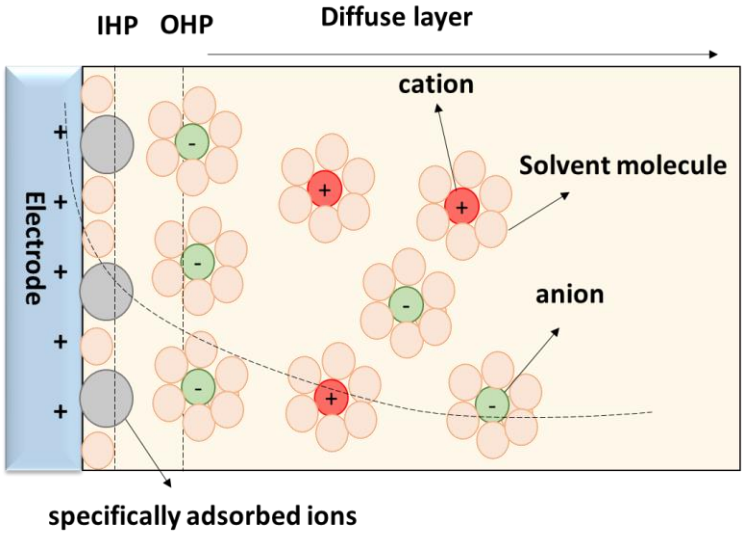

Figure 1.4 Schematic diagram of the electrical double layer at the electrode-electrolyte interface according to Stern's model.

1.2.5 Iontronic devices and applications

Despite the fact that iontronics is a new research direction, there was very old attempts toward coupling ions with electronic devices. In 1946, Brattain and Ginley tried to use electrolytes to control the current flow in a transistor.[34] One year later Shockley, Bardeen, and Brattain invented the all solid-state transistor and the golden era of transistor started. Therefore, the older work was forgotten a bit. Some years later in 1971 Bergveld removed the gate of a transistor and immersed it in electrolyte. He noticed a change in conductivity of the semiconductor as a result of ion adsorption into the insulating layer of the transistor.[35] Since then, more research is concentrated on using ions to control electronic devices, which led to the invention of one of the most important ionic devices: the electric double layer transistor, shown in Figure 1.5B.

Figure 1.5 shows the difference between an electronic (field effect transistor) and an iontronic (electric double layer transistor). The field effect transistor consists of three electrodes: gate, source and drain. The drain and source are placed on the top of a semiconductor material. A thin insulator layer is placed between the three electrodes as shown in Figure 1.5A. When for example a negative voltage is applied on the gate the resulted electric field attracts the positive charge in the semiconductor material creating a channel between the drain and the source. On the other hand, the electric double layer transistor consists also of three electrodes. On top of a semiconductor material, the drain and source are placed. The gate is separated from the semiconductor with the electrolyte. Two electric double layers are formed: one at the interface between the gate and the electrolyte, and the other at the interface of the semiconductor and the electrolyte shown in Figure 1.5B. Different types of electrolyte are being used in the EDLT like polymer electrolytes, ionic liquids and ionic gels. [36-38] The electric double layer transistor has large capacitance, high sensitivity, low power consumption and scalability that allows it to be fabricated in nanoscale dimensions.[39, 40]

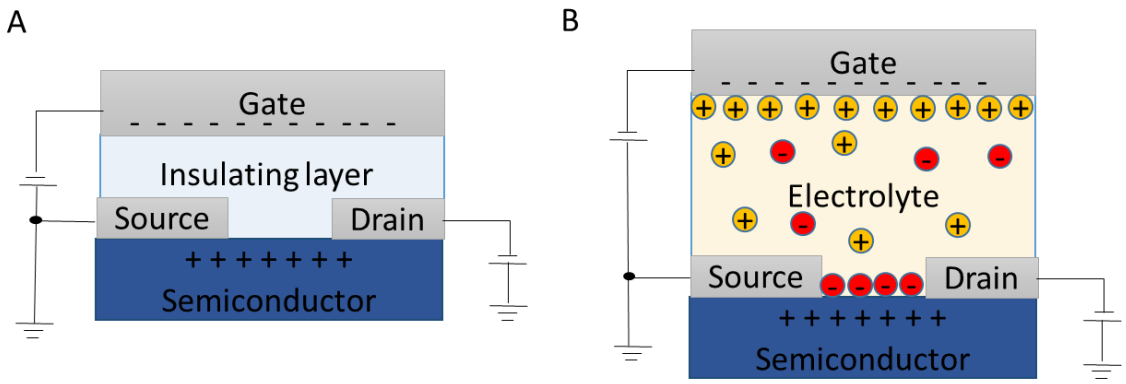

Figure 1.5 (A) Schematic description of the Field effect transistor configuration (B) Schematic description of the Electric double-layer transistor configuration

Nowadays memories based on semiconductor materials are very important in electronics. Every computer is based on the von Neumann architecture, which consists mainly of two units processing unit and a memory unit. In this architecture as shown in Figure 1.6, the data are transferred between these two units. There are many drawbacks of von Neumann architecture but the main drawback is the von Neumann bottleneck shown in Figure 1.6A.[41] The von Neumann bottleneck is becoming more and more critical to be solved with the increasing demand of data processing especially in the currently exploding artificial intelligence era (AI)[42]. Another problem is the memory wall, which is a term used to explain the difference in speed between the memory and the processing units[41, 43]. This problem arises because the processor operates faster than the memory, including RAM (Random Access Memory) and secondary storage devices such as hard drives or SSDs (Solid State Drives). Because of this speed difference when the processing unit requires data from the memory, waiting to fetch data from a slightly slower memory subsystem tends to be longer. In general, the performance of the system may suffer because of this delay. [44] Beside the resulted latency a high power consumption is also resulted from moving the data between the processor and the memory unit. [45]

A possible solution to the von Neumann architecture is the neuromorphic computing. Neuromorphic systems are a non-von Neumann computing systems that its function and structure is inspired by the human brain.[46-49] Another attractive feature of the natural neurons in the human brain is the energy consumption as they can often operate on orders of magnitude less power than normal computing systems.[50] In neuromorphic devices, ions can be used to mimic the behavior of neurons and synapses. With the help of iontronics, new devices

controlled by ions can be provided. Together, iontronics and neuromorphics are capable of creating systems that can mimic natural processes and develop new technologies.[11]

In-memory computing is considered another promising solution to break the von Neumann bottleneck. In the in-memory computing the processing and memorizing of the data take place in the same unit minimizing the data movement. Figure 1.6B shows a schematic description for in-memory computing. A resistive switching memory or a memristor is considered to be a key element in the in-memory computing systems [51]. A memristor is a combination of a memory and a resistor, a device that can remember the history of its resistance. [52] There are different types of memristors one type is the memristors based on ions and apply iontronic concepts or iontronic memristors. [53-55]

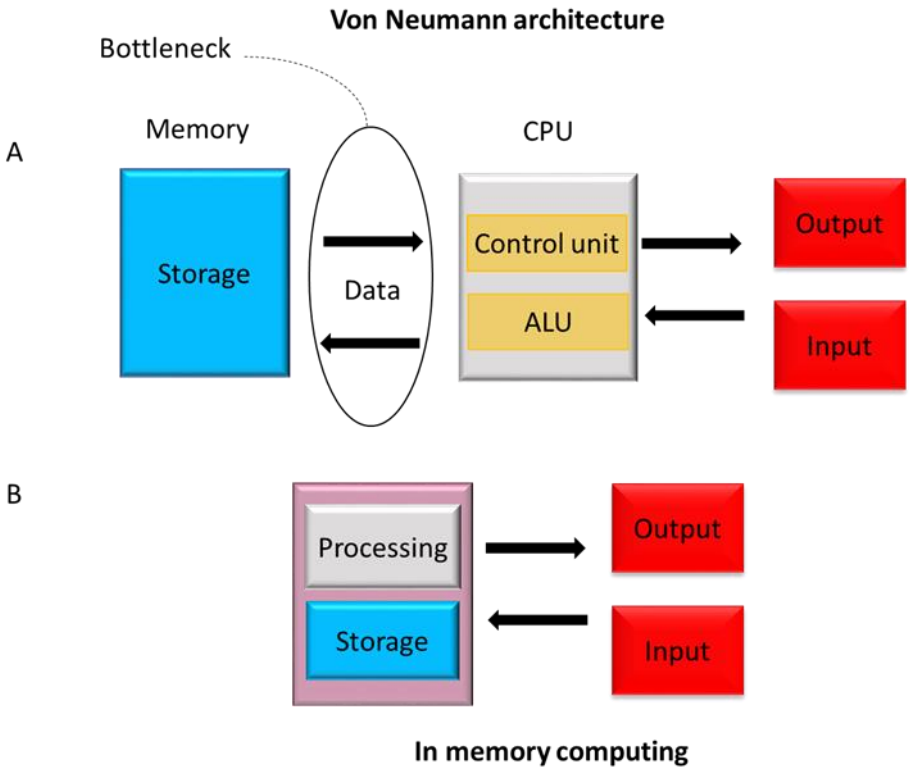

Figure 1.6 (A) Von Neumann architecture and the bottleneck of transferring date between the storage and the CPU that contains a control unit and a ALU which is a combinational digital circuit that makes arithmetic and bitwise operations on integer binary numbers. (B) In-memory computing.

Using memristors as logic gates is gaining more attention to reach a state where it can be used in the in memory computing as an alternative computing architecture for the von Neumann architecture [56, 57].

With the working principle of iontronics that based on ions like the human body, the iontronic devices can revolutionize the health care technology, neuromorphic computing or in memory computing. Through these advantages, iontronics can be the base for the development of artificial intelligence and emerging soft robotics, in addition to Internet of Things (IoT).

1.3 Aim of the thesis

Yet more iontronic devices needs to be invented. Not only more devices needs to be developed, but also more investigations of what happens inside the devices is important.

The main aim of this thesis is, therefore, to investigate a newly invented purely iontronic device called ionic voltage effect soft triode (IVEST). Through the chapters of the thesis, it is described how the device was built, characterized, tuned, and modified. The aims of the thesis are summarized as follows:

1) Detailed description of the construction of a purely iontronic device. To reach a stable device mechanically and better in performance, different construction methods need to be tested.

2) Comprehensive characterization of the ionic voltage effect soft triode (IVEST). As a new device, trust worthy characterization methods should be developed to discover the effects the device can possess.

3) Understanding the mechanism inside the device. To be able to use the device in applications or to tune its performance, the mechanism should be investigated and understood.

4) Investigating the opto-IVEST. Since the structure of the IVEST allows a wide range of modifications, testing one of them and turning the device into an optoionic device was selected as most interesting. With the modification of the device, it can be pushed more towards applications especially in neuromorphic computing.

2. A purely Ionic Voltage Effect Soft Triode

Most of the content of this chapter was published as "A purely ionic voltage effect soft triode" Mohamed, E., Josten, S., & Marlow, F. (2022) Phys. Chem.Chem. Phys, 24(14), 8311-8320. The parts of the text, as well as the figures of the following section, are reprinted and reproduced, with permission from Royal Society of Chemistry.[56]

2.1 Introduction

The phenomenon of ionic amplification or amplification of a signal using ions was observed for the first time in a microfluidic ionic bipolar junction transistor.[58] This type of transistor achieved a current gain of 10, by applying an emitter gain voltage of 4V. Another type of ionic transistors are the ionic field effect transistors. Ionic field effect transistors represent a class of ionic transistors where ionic or molecular species in micro or nano fluidic systems are controlled by an electric field on the gate electrode of the transistor.[5, 59] Most of these devices have the ability to work as amplifiers. However, the majority of these transistors utilize semiconductors or semiconducting polymers as their channels, which require complex materials and construction methods. Despite the development of numerous ionic devices,[60] there has been no research on signal amplification within purely ionic systems.

Another crucial aspect in the field of iontronics is the ionic memory. Different types of new memory devices exist, but the resistive switching memory, also known as memristor, appears to be more intriguing. A resistive switching memory is characterized by low energy consumption, rapid operation, and a simple structure.[61-63] These memories are expected to open a new door for computing systems and biological applications as they have common working principles like the biological systems.[11, 64] In memristors information processing and storage at the same physical place (non von Neumann computer architectures) and are believed to be the building block for realizing the brain-inspired hardware.[65, 66] Memristors have various working mechanisms such as, electrochemical reactions,[62] vacancy-based resistance changes/charge trapping,[67] and phase-change materials.[68] The most famous structure of memristors is to use an insulator between two metals (MIM).[69] They show interesting non-linear behavior in circuits, but they also present challenges in terms of stability

and device integration.[70] [71] Iontronic resistive switching memories are important for the field of neuromorphics to mimic the function of the brain and to avoid the von Neumann bottleneck described in the previous section. Recently several memristors were reported.[60, 72]

Inspired by DSSCs, a new, purely ionic device with amplification behavior and memory functions called Ionic Voltage Effect Soft Triode (IVEST) was invented.[73] This device is a simple electrochemical micro-cell, which consists of a top electrode and two or more bottom electrodes. The basic idea of this device is to control the concentration of ions by the voltage applied on the top electrode. This is where the words (Ionic Voltage Effect) come from in the name of the device. This top electrode is made of porous TiO_2, a material that can adsorb ions depending on its potential. The advantages of this device are the ability to be used as an amplifier or a memory, the ease of manufacturing, the low power consumption and the avoidance of any ultra-pure semiconducting material. The need for eco-friendly devices is increasing and using abundant materials and less sophisticated manufacturing methods is a challenge nowadays.

In this chapter, the construction of the IVEST with different approaches is explained. The amplification and the memory effects of the device are investigated and tuned.

2.2 Device construction and other experimental details

When the IVEST was first built, three different structures were investigated. We started with what we called sc(sc||sc) where the three electrodes were covered with semiconductor layer of mesoporous TiO_2. The second construction was m(sc||sc) where the top electrode is a metal mesh covered with a 1 nm of platinum, and the two bottom electrodes are metal wires covered with a mesoporous TiO_2 layer. The final construction investigated was sc(m||m) where the top electrode is a metal mesh of stainless steel covered with a mesoporous TiO_2 layer. The stainless steel has the advantage of lower cost and is already investigated in the DSSCs. [74] The bottom electrodes are metal wires covered with 1 nm platinum as shown in Figure 2.1A. The third construction sc(m||m) showed the most interesting performance in terms of both memory effect and amplification. For this reason, we continued our investigation on the sc(m||m) construction.

All the devices in this dissertation are built with the sc(m||m) construction unless mentioned.

Figure 2.1A shows a schematic description of the IVEST in its sc(m||m) version. As mentioned before it consists of three electrodes: a top electrode covered with a mesoporous TiO_2 layer as a semiconductor material, and two bottom electrodes covered with platinum. A polypropylene spacer is used between the electrodes to avoid short circuit between the electrodes. Finally, redox couple electrolyte is injected inside the device. Figure 2.1B shows the symbol used for the device in the circuits and different configuration used.

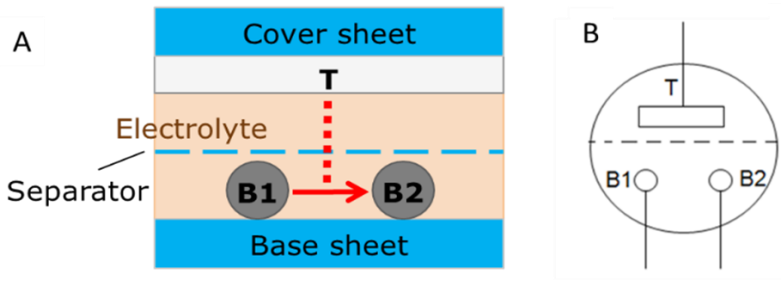

Figure 2.1 (A) Schematic description of the IVEST (B) Symbol of the device. [56]

Each part of the device was prepared separately as follows, and then combined together to build the device.

2.2.1 Solutions

To prepare the mesoporous layer covering the top electrode, a solution of titanium isopropoxide is prepared and another TiO_2 suspension is prepared as following. This recipe was adapted from DSSCs [21, 74, 75]

Titanium isopropoxide solution: 0.34 mL titanium isopropoxide (Acros Organics) and 0.23 mL 2 M HCl (Prolabo) were dissolved in 98 mL isopropanol (Merck LC-MS grade) under argon stream and stirred for 24 h.

TiO_2 particle (TP) suspension: A non-optimized suspension was used in the preparation of the top electrodes in the devices of chapter 2. Starting from chapter 3, an optimized suspension was used to prepare the top electrodes in the devices.

Non-Optimized suspension: First, an α-terpineol-ethylcellulose mixture was prepared by melting 47.5 g α-terpineol (Sigma Aldrich) in a round flask in oil bath under stirring. When reached 70 °C the heating rate was slowed down, and then 3.7 g ethylcellulose (Sigma Aldrich) was added gradually. The mixture was kept stirring overnight. To 35.36 g of terpineol-ethylcellulose mixture, 9.02 g nano anatase powder (Sigma Aldrich), 1.5 mL concentrated

acetic acid (J. T. Baker) and 14.29 mL isopropanol were mixed in a TopiTec mixer for 30 minutes at 2000 rpm. Finally, the resulting viscous paste was diluted by appropriate amounts of the terpineol-ethylcellulose mixture and isopropanol to reach different layer thickness on the top electrode.

Optimized suspension: First, an α-terpineol-ethylcellulose mixture was prepared by melting 47.5 g α-terpineol in a round flask in oil bath under stirring. When reached 70 °C the heating rate was slowed down, and then 3.7 g ethylcellulose was added gradually. The mixture was kept stirring overnight. Again a 35.16 g of terpineol-ethylcellulose mixture, was added to 20 mL ethanol, 1.05 mL acetic acid, 6.7 g anatase and 5.55 mL water. All the components were mixed in a TopiTec mixer for 30 minutes at 2000 rpm [21].The optimization work was carried out in a series of experiments (UNA-UA-326) by Ursula Petrat and Frank Marlow.

3. Electrolytes

In this work, three electrolytes were tested in the construction of the IVEST. The first electrolyte is the B13-1 electrolyte. [20] The second electrolyte is B13-1L (L = light) which is the same as B13-1 but with less chemicals. Finally, an electrolyte based on ethylene glycol was tested.

B13-1 Electrolyte: B13-1 is a redox couple electrolyte and is the main electrolyte used in this thesis adapted from ref.[20] To prepare the electrolyte, in 3-methoxypropionitrile (Sigma Aldrich) 0.05 M I_2 (Fisher Scientific), 0.8 M 1-methyl-3-propylimidazolium iodide (Sigma Aldrich), 0.3 M benzimidazole (Sigma Aldrich) and 0.05 M guanidinium thiocyanate (Sigma Aldrich) were dissolved and left on the stirrer for 2 h. After stirring, the solution was stored in dark in a brown glass bottle. The conductivity of this electrolyte was 8.64 mS/cm measured with a conductivity meter (MT Seven Compact). In some experiments, the electrolyte was diluted with appropriate amounts of the solvent described by the electrolyte dilution factor X_e.

The B13-1 electrolyte showed the best performance and stability. This electrolyte was used in most of the devices in this dissertation unless mentioned.

B13-1L Electrolyte: B13-1 electrolyte was mainly designed for the dye-sensitized solar cells. It contains different chemicals that are necessary to be compatible with the used dye in the DSSC. The electrolyte was tested without the benzimidazole and 0.05 M guanidinium thiocyanate. Same preparation method as the B13-1 electrolyte was used to produce the B13-1L electrolyte. This electrolyte gives good result, however it has some issues with the stability.

The stability of the electrolyte was not good in terms of the measured resistance between the two bottom electrodes on the long term.

MH12 Electrolyte: The electrolyte used for the first time in Mülheim 2012 is ethylene glycol-based. This electrolyte is simpler and contains fewer chemicals. To prepare this electrolyte in 100 ml Ethylene glycol purity 99.9, 1.274 g of I_2 and 6.67 g of LiI were added. The solution was left for stirring until it is dissolved.

The conductivity of the three mentioned electrolytes was measured at different dilutions (X_e) using a conductivity meter (MT Seven Compact). As presented in Figure 2.2, B13-1 has the highest conductivity values. The lowest conductivity is for MH12 electrolyte. As expected, the conductivity decreases with dilution. Based on the results on Figure 2.2, B13-1 was further used in the IVEST.

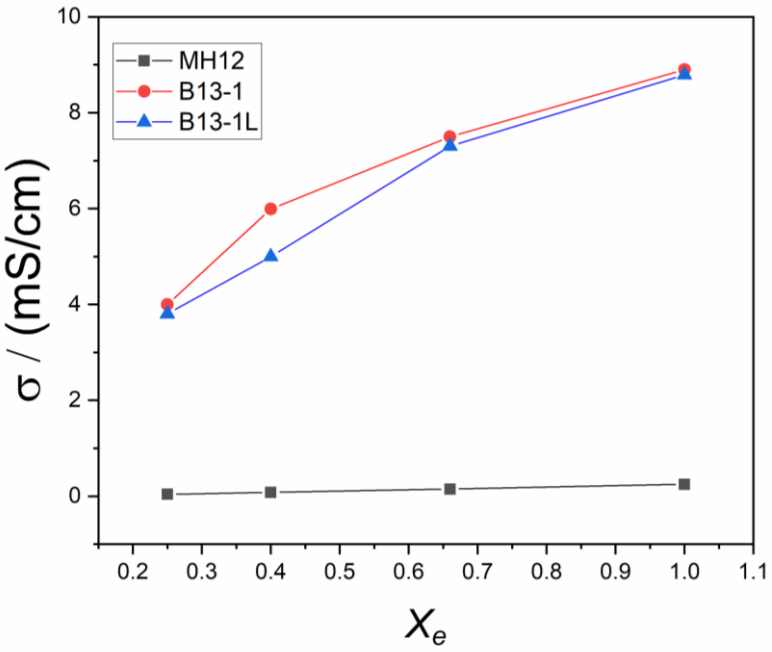

Figure 2.2 Conductivity of the used electrolytes at different dilutions

2.2.2 Electrodes preparation

Here the electrodes preparation for the sc(m||m) structure is explained.

Top Electrode: The top electrode is a stainless steel mesh (type Ti316 from HAVER&BOECKER). The stainless steel mesh gives flexibility to the device. The dimension of the top electrode is 7×5 mm^2. To clean the meshes a Labosol and in a NaOH-EtOH solution were used. The meshes were left in each solution for 30 min. Then the meshes were rinsed with

water, and dried in nitrogen stream. The blocking layer or the compact layer was coated on the top electrode after cleaning by dipping in the titanium isopropoxide solution (climate chamber WK-340/40, Weiss Umwelttechnik GmbH, 25–28 % rH, 22 ^{o}C), drying in oven at 120 ^{o}C for 1 h. This blocking layer is used to stick the mesoporous TiO_2 layer to the metal mesh, to prevent the electron back flow, and to reduce the possibility of the reaction between the electrode and the electrolyte. Finally, the meshes were dipped in mesoporous (mp) TiO_2 solution and calcinated at 450 ^{o}C for 15 min. The number of layers of titanium dioxide paste suspension on the top electrode is represented by X_{TiO2}. Figure 2.3 Shows the resulted Layer on the top electrode under SEM using the optimized TiO_2 suspension [21]. Figure 2.3A shows a smooth layer of TiO_2 on the meshes

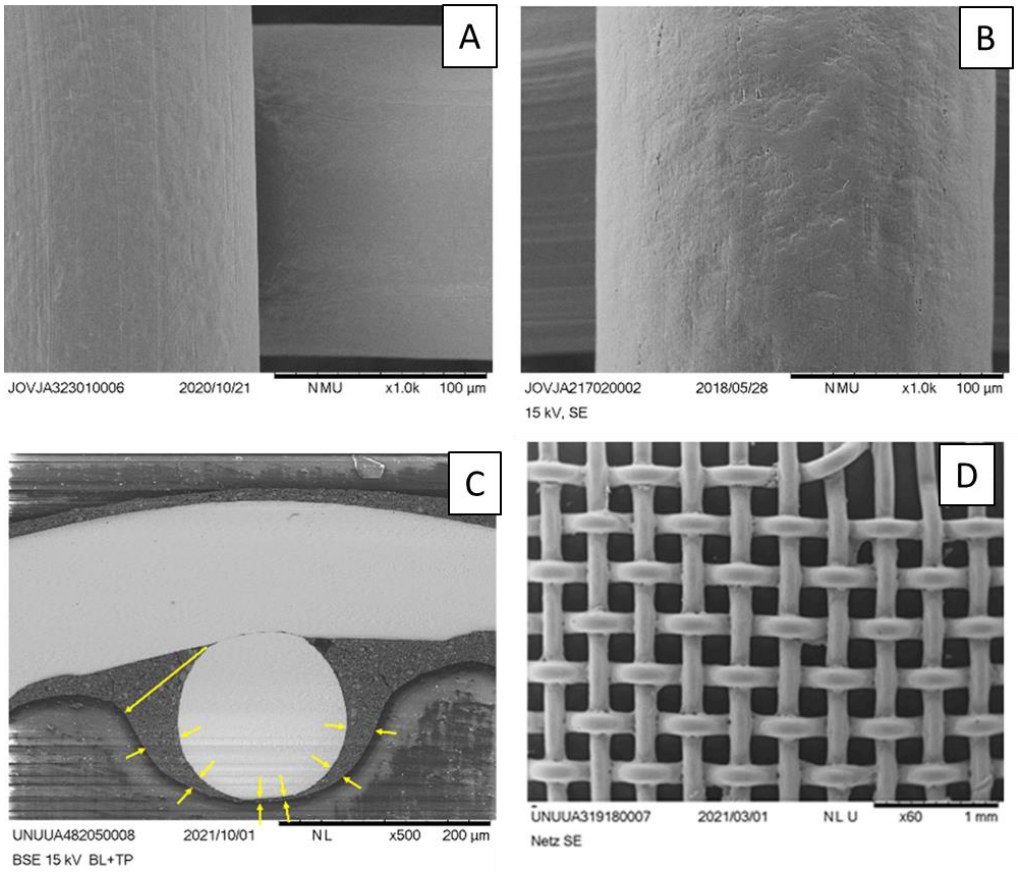

Figure 2.3 (A) SEM of the metal meshes after cleaning (B) SEM pictures of the top electrode with blocking layer (C) Cross section of the top electrode with optimized mesoporous TiO_2 layer (D) TiO_2 coating of the top electrode [21, 74].

In contrast Figure 2.4 shows a rough layer of TiO_2 on the mesh with excess of TiO_2 particles between the wires of the mesh when the non-optimized suspension is used.

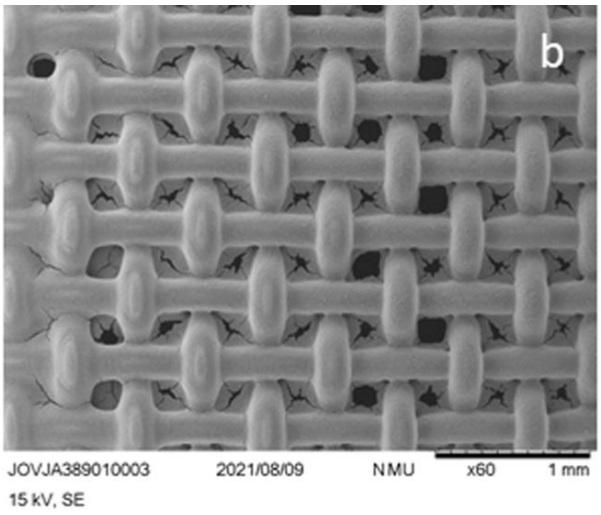

Figure 2.4 Metal mesh covered with TiO_2 layer using the non-optimized suspension [21]

Bottom Electrodes: To make the bottom electrodes, two metal wires, composed of the same stainless steel material as the top electrode (Ti316) 0.15 mm, went thorough cleaning process utilizing Labosol and a NaOH-EtOH solution. After that, the wires were rinsed with water and dried using a nitrogen stream. Finally a thin layer of platinum = 1 nm of platinum was deposited on both sides of the wires using a sputtering machine (Q150T S, manufactured by Quorum GmbH).

To make a bottom electrode covered with TiO_2 layer for m(sc||sc) or sc(sc||sc) structure, same procedure as mentioned in section 2.2.2. For a top electrode covered with platinum to use in the m(sc||sc) structure, same procedure as in 2.2.2 is used with the metal meshes.

2.3 Device Fabrication

2.3.1 Fabrication method A

This fabrication method was used only for the devices of chapter 2.

To build the device a polypropylene film with a thickness of 30 μm was first used as base for the device. The two bottom electrodes were put on it. A polypropylene mesh (Franz Eckert GmbH) with a typical thickness of 200 μm or a membrane was put on the top of the bottom electrodes as a spacer and separator. The top electrode was placed on the top of the spacer as shown in Fig. 2.1A. In addition, a polypropylene top layer was used for encapsulation and the system was glued together using a hot press (Lotus Transpresse LTS 12S) at 110 °C. The electrolyte was injected inside the device using a syringe. Finally, the device opening was sealed

using a metal hot spot (Wetekom soldering station) at 150 °C. A final optical look of the device is shown in Fig 2.5.

This method of fabrication had some drawbacks. It was challenging to have the same geometry for every device and the mechanical stability of the bottom electrodes was not the best. As the wires were connected to the measurement, circuit the possibility of destructing the device or move one of the wires from its place was high. For this reason an optimized fabrication method was developed. Nevertheless, fabrication method A gave acceptable results and had the advantage of a lower number of steps.

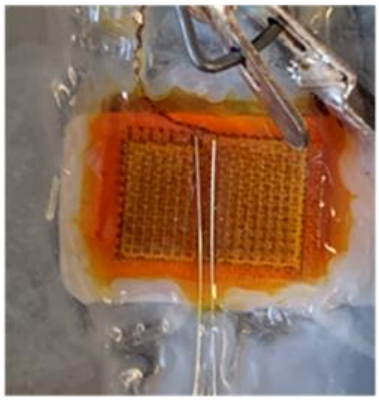

Figure 2.5. Optical look of the IVEST built with the fabrication method A [56]

2.3.2 Fabrication method B

Fabrication method B was developed to improve the fabrication method A. The main difference from the previous method, was using a frame to stabilize the geometry of the device and fixing the device on an electronic breadboard.[76] This method was developed in a separate series of experiments (MLW-AC-148.1).

After preparing each part separately, all the parts were combined together, to form the device as follows. First, a polypropylene foil with 30 µm thickness was used as a base of the device. Parafilm® from Bemis® was placed on the polypropylene foil. A plastic ribbon with a thickness of 0.5 mm was placed on the polypropylene as a frame to assure a fixed known geometry. The top electrode was then fixed on the plastic ribbon. A spacer was placed on the top electrode then the bottom electrodes were located on the top of the spacer. Finally, another piece of parafilm® was placed and a layer of polypropylene foil was used to close the device. The device was glued together using a hot press (LTS 12S, Lotus Transfer Press Solutions GmbH) at 110 °C. The electrolyte was injected inside the device using a cannula. To close the opening after

injecting the electrolyte a metal hot spot (Wetekom soldering station) at 115 °C was used. At the end, the device was fixed on a standard breadboard for electronic devices. Figure 2.6 shows the final look of the device.

The fabrication method B improved the mechanical stability and the reproducibility of the IVEST significantly.

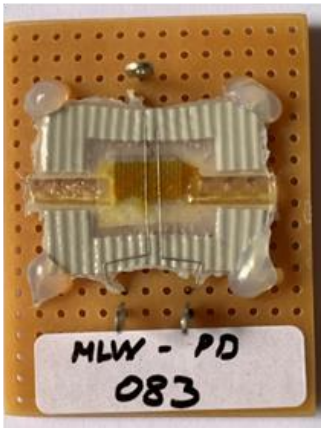

Figure 2.6 Final look of the IVEST using fabrication method B [76]

2.3.2.1 Device Stability

After using fabrication method B, the lifetime of the devices increased. Besides the lifetime, the fluctuation of the resistance between the two bottom electrodes decreased. For the device built with the optimized fabrication process and with the same TiO_2 layer thickness and same electrolyte concentration, the fluctuation is less than the devices built with the non-optimized fabrication method A.

Figure 2.7 shows the effect of the construction method, electrolyte concentration (X_e) and the thickness of the TiO_2 layer (X_{TiO2}) on the resistance between the two bottom electrodes. The open violate circles in Figure 2.7 represent devices built with fabrication method A explained in section 2.3.1 and the non-optimized TiO_2 suspension explained in section 2.2.1.

Figure 2.8 presents the stability of different devices built with fabrication method B. Varity of devices with different number of TiO_2 layers on the top electrode and different electrolyte concentration were observed over more than 200 days.

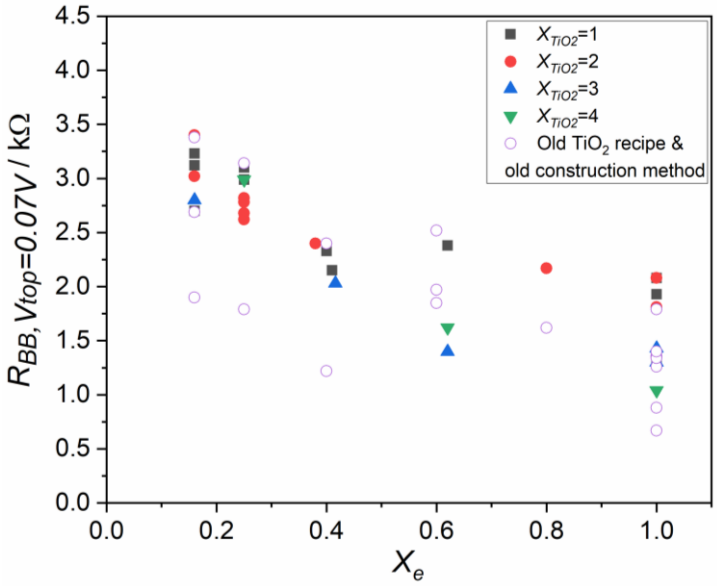

Figure 2.7 The new construction method (fabrication method B) clearly decreased the scatter around the systematic trend for the thickness of TiO_2 layer (black and read data points) in comparison to the old construction method (fabrication method A) [76]

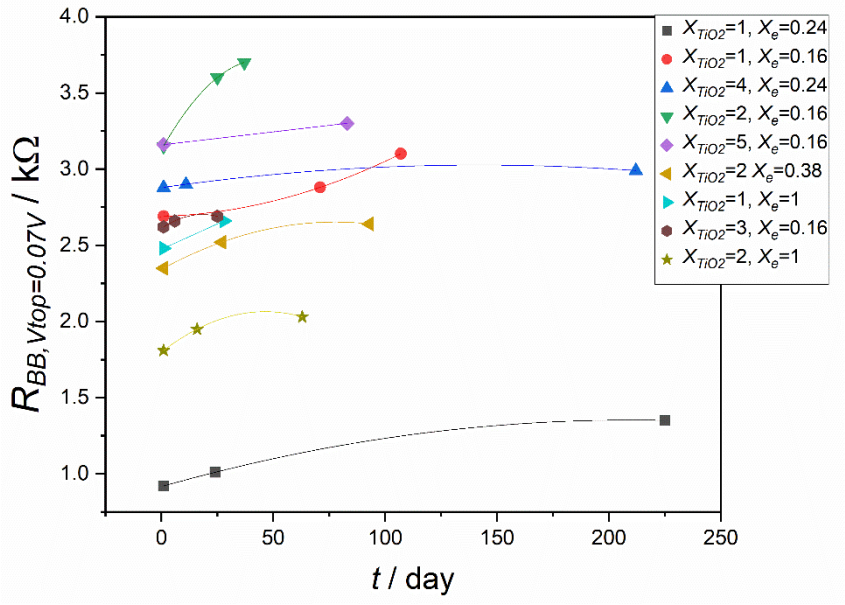

Figure 2.8 Stability of some of the devices after improving the construction method. Devices with different electrolyte dilution factors X_e and different TiO_2 thickness on the top electrode (described by X_{TiO2}). Each curve represents one device over time.[76]

2.3.3 Alternative Fabrication Methods

2.3.3.1 Printing

Printing technologies are widely used in many fields. In electronics, 3D, inkjet and screen-printing are used to fabricate many devices. [77-79]. Compared to screen printing, and inkjet printing, 3D printing provides new possibilities but also new challenges.[80] In 3D printing 2D layers are stacked together to create a three-dimensional object using a digital model designed in computer-aided design (CAD) software.[81] The commercial 3D printers are able to make a structure ranges from a few millimeters to centimeters.[82] The IVEST could be printed by either 3D, inkjet or screen-printing. The main advantage of printing the IVEST is it will allow the construction of the device in smaller scales.

With the help of Hendrik Köster the 3D printing possibility of the IVEST was investigated. Using a 3D printer (Creality Ender 7) and a Polyethylene Terephthalate Glycol (PETG) filament, a caddy for the IVEST was printed as shown in Figure 2.9. The 3D printed caddy consisted of different layers of Polyethylene Terephthalate Glycol. The design of the caddy gives a place for the bottom electrodes and the top electrode. The design shown in Figure 2.9 allows more than two bottom electrodes (a pentode). On the top of the caddy, two ports were made. One to inject the electrolyte and the other one to let the air out during injection. However, there is some challenges regarding the compatibility of the electrolyte with the filament. In some samples, there was leakage after injecting the electrolytes.

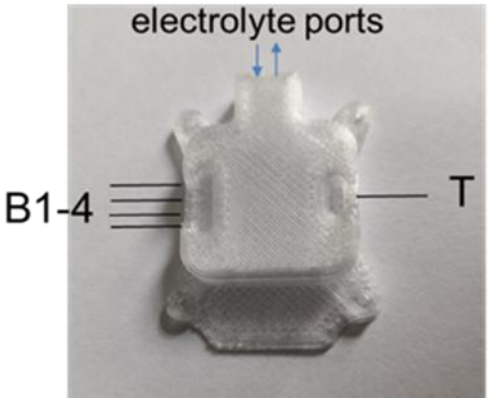

Figure 2.9 A 3D printed IVEST (MLW-PD-097)

As the caddy consists of layers of the filament, there were some holes letting the electrolyte out after injection. To come over the leakage problem, before injecting the electrolyte the caddy was placed on the oven for 10 min on 75 ^{o}C. Then, after injecting the electrolyte, the ports was

soldiered using soldering gun. This made the situation better; however, the electrolyte seems to be not compatible with PETG.

2.3.3.2 Sputtered bottom electrodes

Another alternative fabrication method is to sputter the bottom electrodes using a pattern as shown in Figure 2.10. In this fabrication method, a sputtering machine (Q150T S, Quorum GmbH) was used to sputter 10 nm Pt electrodes. The construction steps differs a little bit from the steps mentioned in previous sections. In this method, the encapsulation of the device was challenging as the bottom electrodes should be handled with care to avoid scratching them. Figure 2.10A gives a schematic description of the construction of the device with a sputtered bottom electrodes.

A polypropylene foil was used as a base and on the same time, the bottom electrodes were sputtered on it using the sputtering machine and a pattern. A separator made of polypropylene was placed on the top of the bottom electrodes. After that, the top electrode was placed on the top of the spacer. Finally, a polypropylene foil used to close the device and a metal hot spot (Wetekom soldering station) at 115 °C was used to seal it. The mechanical handling and connecting the device to the circuit was difficult as the wires were very easy to be destroyed. The resulted device is shown in Figure 2.10B.

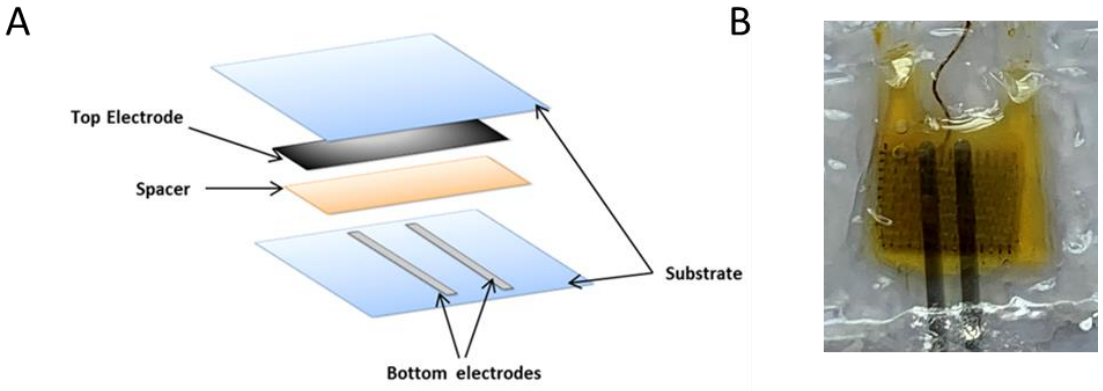

Figure 2.10 (A) Schematic description of the sputtered bottom electrode IVEST. (B) Sputtered bottom electrodes.

The main benefit of using this particular approach lies in its ability to effectively control the overall size of the device. By using smaller patterns, the dimensions of the bottom electrodes can be controlled, thereby offering greater flexibility in terms of the number of sputtered electrodes and the whole size of the device.

It is important to note that while this method was not extensively utilized, a few devices were constructed to demonstrate that the IVEST could be built using alternative techniques. It is also worth to mention that the devices constructed using the sputtered bottom electrodes method exhibited normal amplification and memory behavior. Likely the bottom electrodes can also be inkjet printed, which allows more flexibility in the size and geometry of the device.

2.3.3.3 Commercial electrodes: Humidity sensors

Commercial bottom electrodes were also tested. In this fabrication, a humidity sensor (EFS-10) from B+B sensors was used. As shown in Figure 2.11A the humidity sensor consists of platinum wires on top of a ceramic plate covered with a polymer layer. To use this sensor it was first cleaned using WD-40 spray to remove the sensitive polymer layer as shown in Figure 2.11B (UNA-UA-218). To build the device a polypropylene foil was used as a base, then the humidity sensor electrodes was placed on top of it. A polypropylene separator was placed on the top of the sensor. The top electrode of a metal mesh covered with TiO_2 layer as mentioned before was placed on the top of the spacer. Finally, another polypropylene foil was placed on the top of the metal mesh. A metal hot spot (Wetekom soldering station) at 115 °C was used to seal the device. The electrolyte was injected using a syringe. The final look of the device is shown in Figure 2.11C.

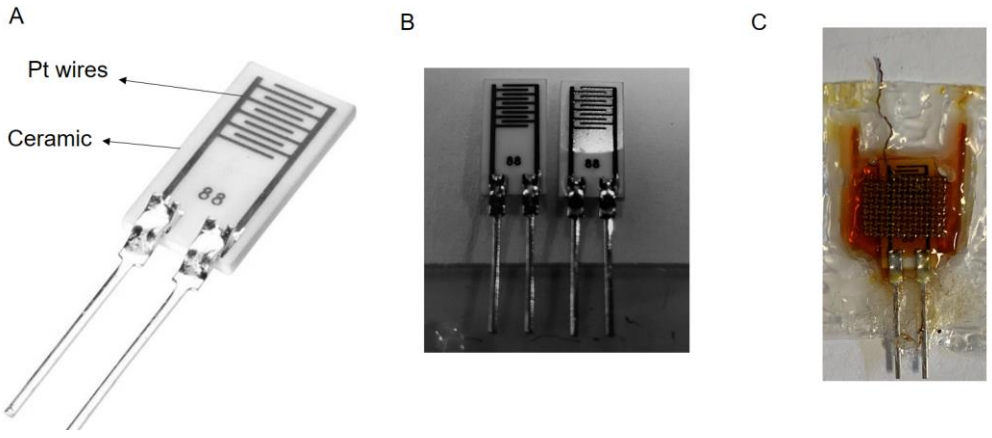

Figure 2.11 (A) Humidity sensor (EFS-10) from B+B sensors [83] (B) Humidity sensor before and after removing the polymer layer (UNA-UA-218) (C) IVEST build with humidity sensor as bottom electrodes.

The resulted device showed the same characteristics as a normal IVEST. However, the sealing of the device was challenging because of the thickness of the used sensor that caused the electrolyte to dry out.

In general, the IVEST can be fabricated with different methods. This gives the possibility for reducing the size of the IVEST and to commercially using the device.

2.4 Device Characterization

The IVEST can be considered as a two-gate device with input and output. To characterize the device different configurations were used. The used configuration for characterizing the IVEST were inspired by how does the dye sensitized solar cells and transistors are characterized.[75, 84]

2.4.1 Common B1 configuration

The first configuration used to characterize the IVEST is common B1 configuration. This configuration was adapted from the configurations used for the transistors as shown in Figure 2.12. [84] The input of the device was measured between the top electrode and B1. The output was measured between the two bottom electrodes. To measure the input of the device, a *JV* analyzer was connected to the top electrode and one of the bottom electrodes. A controlled voltage was applied between the bottom electrodes (Figure 2.12A). The *JV* analyzer is used to measure the current with relation to a changing voltage. The *JV* analyzer used in this thesis was developed in Marlow group. The measurement was carried out using a LabVIEW measurement program (Characteristic measurement_20180716 V2.07 beta 3 extended.vi) written by H. Köster. [74] To measure the output, the control voltage was connected to the top electrode and one of the bottom electrodes, while the *JV* analyzer was connected between the two bottom electrodes (Figure 2.12B).

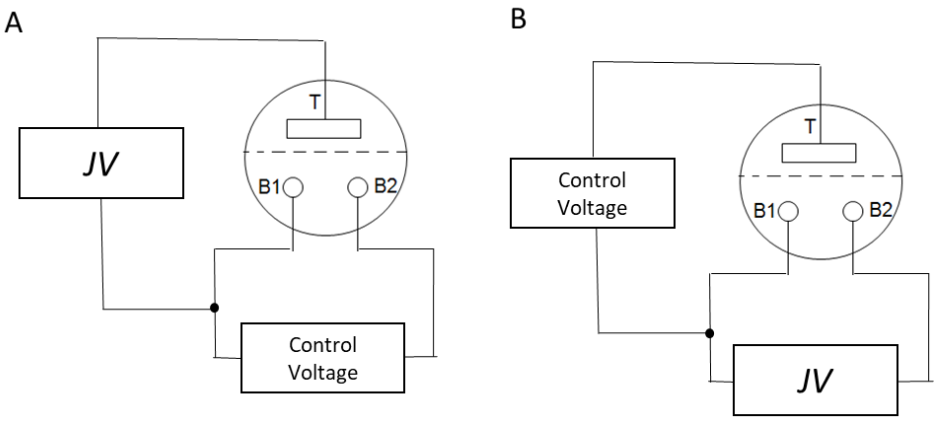

Figure 2.12 (A) input characterization with common B1-cofiguration. (B) Output characterization with common B1-configuration

2.4.1.1 Common B1 characterization for m(sc||sc) and sc(sc||sc) structures

The circuit in Figure 2.12A was used to measure the input current. The input characteristics of the m(sc||sc) structure is shown in Figure 2.13. The input current decreases by increasing the voltage applied between the bottom electrodes. There is an upward shift with increasing the top voltage. The result is noisy but we can see that when the voltage applied on the top electrode is less than 0.3 V, the input current is neatly zero in most cases. When the top voltage increases the input current increases as shown in Figure 2.13.

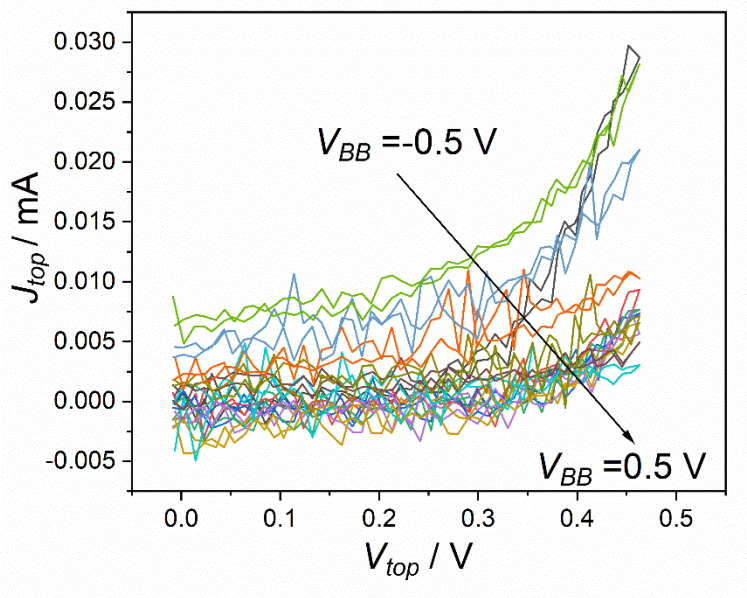

Figure 2.13 Input characteristic using B1 configuration for device with m(sc||sc) structure

The output characterization was carried out using the layout in Figure 2.12B. As shown in Figure 2.14 there is an offset in the beginning of the measurement. This is a reason of the TiO_2 layer on the bottom electrodes. As a semiconductor material the TiO_2 has a specific voltage (threshold voltage) needs to be exceeded to allow the current to pass through the electrodes. Figure 2.14 also shows that by increasing the positive voltage on the top electrode the output current decreases till it reaches nearly zero. This characterization maybe interesting for some application, however we did not investigate it further. The device can switch between nearly 0.2 mA to 0 mA by varying the top voltage at specific conditions. This offset and the complex measurement make it difficult to interpret this result or to take it further. Most of the application does not require the offset in the beginning of the measurement. This can be also a drawback of this structure.

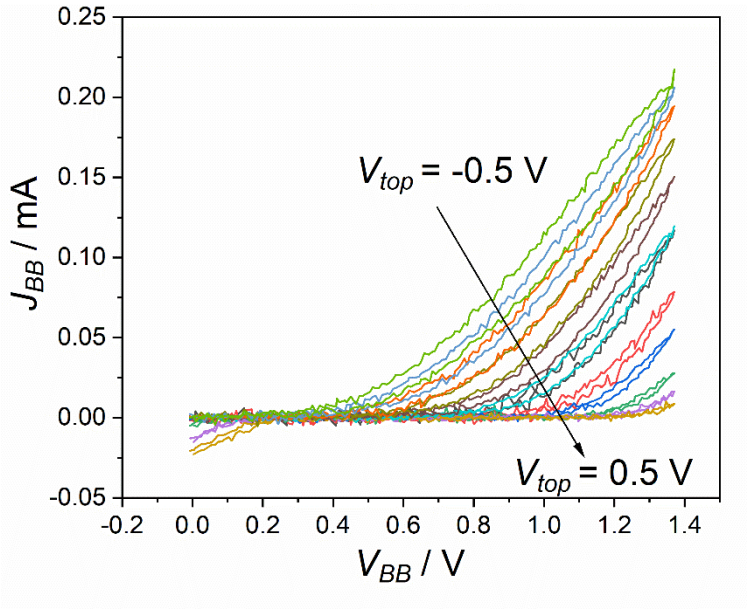

Figure 2.14 Output characteristics using the B1 configuration for the device with the m(sc||sc) structure

The second tested structure was sc(sc||sc). To measure the input, the configuration in Figure 2.12A was used. Figure 2.15 shows the resulted input characteristics. The input current decreases by increasing V_{BB} in the positive direction. The input current J_{top} is nearly zero till V_{top} = 0.25 V then it increases and reaches higher values J_{top}= 0.025 mA at V_{BB} = 0.07 V

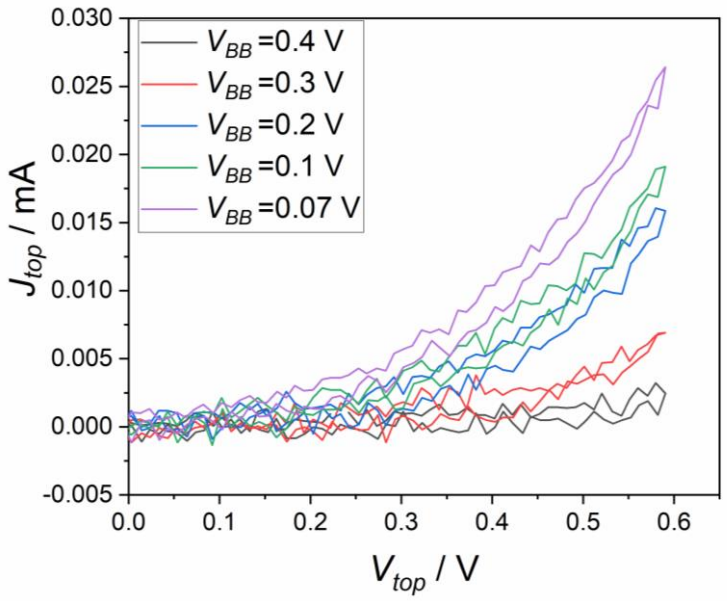

Figure 2.15 Input characteristics of sc(sc||sc) structure by common B1 configuration

To analyze the output, the configuration shown in Figure 2.12B was used. From Figure 2.16 an offset is observed in the beginning of the measurement. By increasing the voltage applied to the top electrode, the output current gradually decreases until it approaches zero. Conversely, when negative top voltage values are applied on the top electrode, the output current increased up to approximately 0.25 mA.

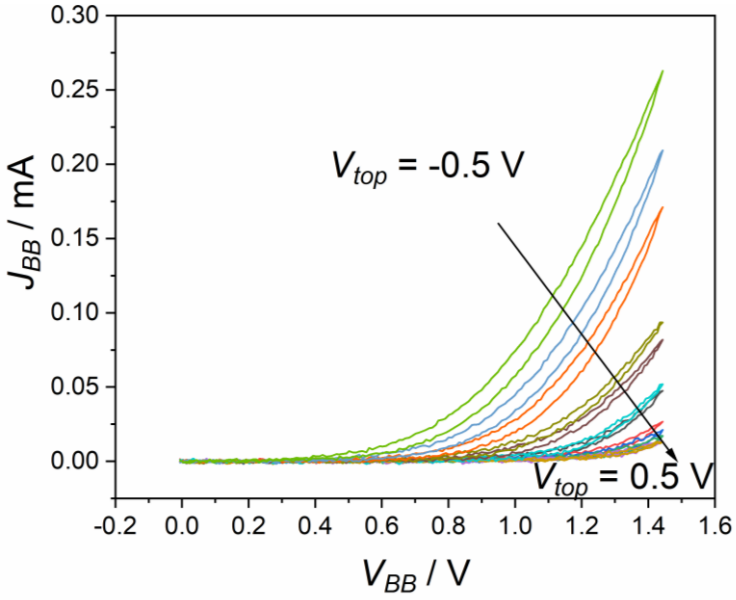

Figure 2.16 Output characterization of structure sc(sc||sc) using common B1 configuration.

2.4.1.2 Common B1 characterization for sc(m||m) structure

Now let us discuss the last structure sc(m||m). To measure the input, the configuration in Figure 2.12A was used. As shown in Figure 2.17 the input current is low even with increasing the voltage applied on the top electrode. This input is lower in comparison to the input of other structures sc(sc||sc) and m(sc||sc). However, the input current shown in Figure 2.17 has bigger hysteresis in the left side of the graph.

Figure 2.18 shows the output characteristics of the sc(m||m) structure. It shows a hysteresis especially when a lower top voltage is applied. When the voltage applied on the top electrode and increases in the positive direction, the hysteresis gets narrower, and the output current changes. However, the change in the output current with varying the top voltage is not big. Based on this result the sc(m||m) looked more promising from application point of view than the other two structures. To understand the mechanism inside the sc(m||m) structure, more investigations were carried out.

In the common B1 characterization method, the two bottom electrodes were not symmetric during the measurements. As a result, it was a complex configuration and difficult to understand the mechanism. Therefore, we left it back and did not use it further in this chapter. However, we are going to use it again in a modified version in chapter 3.

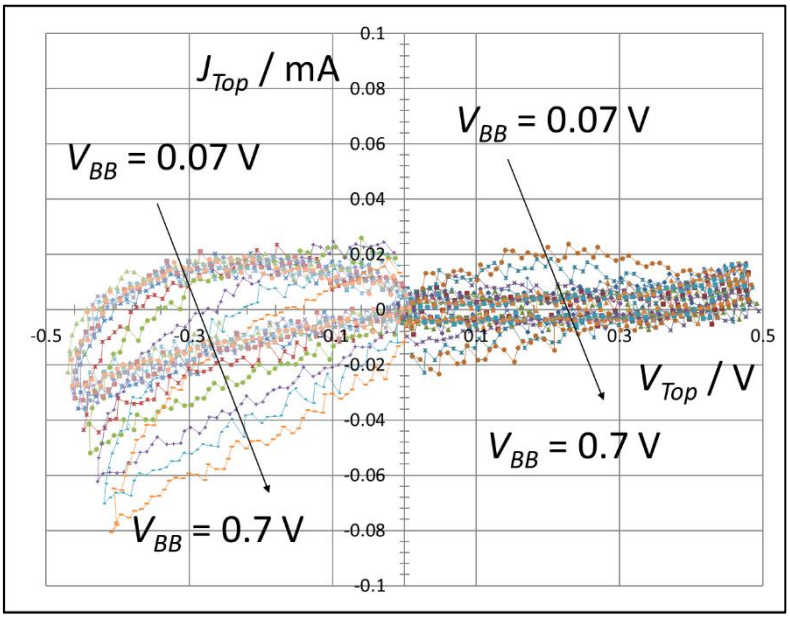

Figure 2.17 Common B1 input characteristics. V_{Top} was scanned with the *JV* analyzer, while fixed V_{BB} values were applied from 0.07 V to 0.7 V

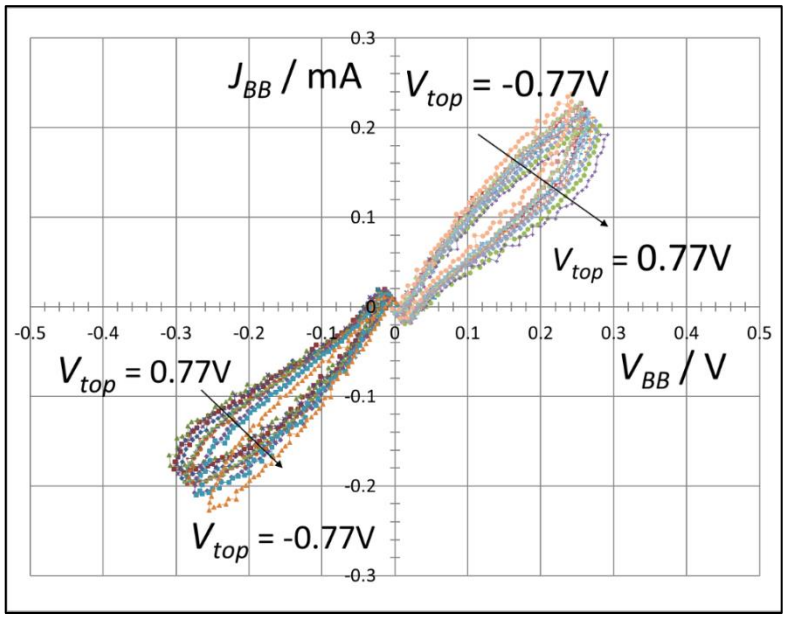

Figure 2.18 Output characteristics of an IVEST using common B1 configuration

The common B1 configuration gave useful but limited information and introduced the effect of the asymmetry between the two bottom electrodes. Because of the strong influence of the hysteresis and the deviation from the known transistors characteristics a new method of characterization was developed.

2.4.2 Symmetric-BB configuration

The aim of this configuration (called Sym-BB) was to have a simpler characterization layout to be able to understand the device. To entangle the measurement made by the common B1 configuration, the first thing to do is to measure symmetric bottom electrodes. In this configuration, two 2 kΩ resistors were incorporated between the two bottom electrodes. These resistors were included to ensure symmetrical bottom electrodes, thereby making the interpretation of the results less complex. In this and the following sections only sc(m||m) structure is used.

2.4.2.1 *JV* analyzer measurements

In order to investigate the device's behavior, both the output and input were measured using a *JV* analyzer and a measurement run controlled by LabVIEW. [74]Two different configurations, namely Figure 2.19 A and B, were employed to measure the input and output. For measuring the input, the configuration shown in Figure 2.19A was utilized. In this configuration, the *JV* analyzer was connected to the top electrode, while a power supply was connected between the two bottom electrodes to maintain a controlled voltage. The input current, denoted as J_{Top}, was

determined by applying a fixed voltage between the two bottom electrodes and employing the *JV* analyzer to measure the resulting current.

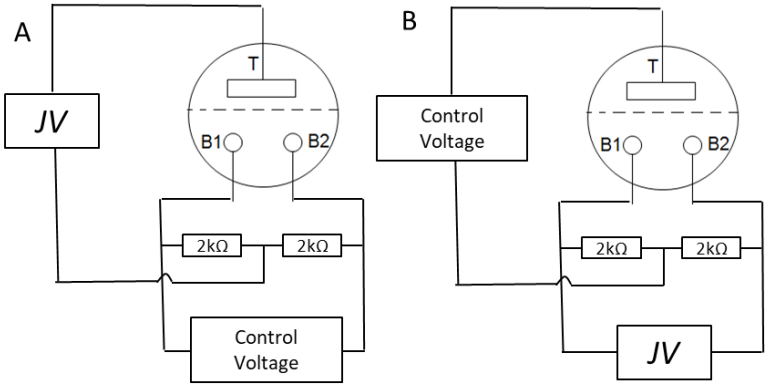

Figure 2.19 (A) Sym-BB-*JV* Input configuration (B) Sym-BB-*JV* output configuration [56]

Figure 2.20 shows the resulted input characteristics. We can see a strong nonlinear dependence of the input current from the input voltage V_{top} and a week dependence of the input current from the output voltage V_{BB}. This means the device has a low back-action. The results of applying V_{BB} with negative values are described in Appendix D. Fig. 2.20 shows the result at positive values of V_{BB} only. Another important observation from Figure 2.20 is that the input current is very low at V_{top} = -0.37 V to 0.5 V. We call this range the low-input current range (LIC).

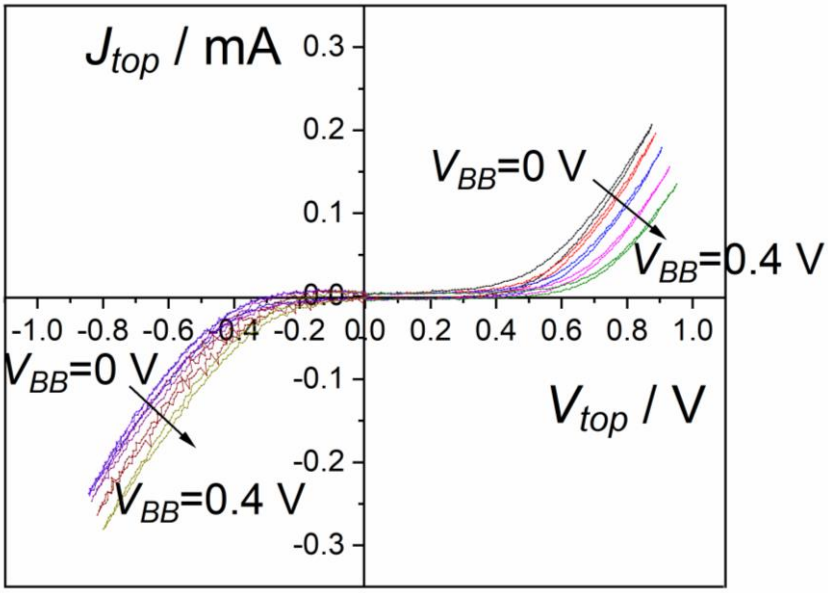

Figure 2.20 *JV* input characterization of a non-optimized IVEST with the Sym-BB configuration. V_{Top} was scanned with the *JV* analyzer, while fixed V_{BB} values were applied from 0 V to 0.4 V. The LIC range is shown in the figure. [56]

To measure the output the configuration shown in Figure 2.19B was used. The resulted output is shown in Figure 2.21. The output characteristics shows nearly a linear behavior and reflects a resistor. Figure 2.21 shows also a dependence of the output on the input. When the top voltage was increased up to -0.8 V the output current increased. The output current showed sensitivity to the change in the input voltage that is more than some of the known ionic devices.[5] When the input voltage is changed from 0 to -0.6 V the output current changes by 0.1 mA at V_{BB} = 0.2 V.

To gain more understanding about the behavior of the device, a transfer curve was calculated. A transfer curve represents the change of the output current in relation to the input voltage at constant output voltage. [66] Figure 2.22 shows the transfer curve of an IVEST, where the output current varies at different V_{top} values. Notably, when V_{top} is increased, particularly above 0.37 V, the output current experiences a significant increase. To further examine the relationship between the top voltage and the output current, the differential transconductance g_m (as defined in Eqn.2.3) was calculated.

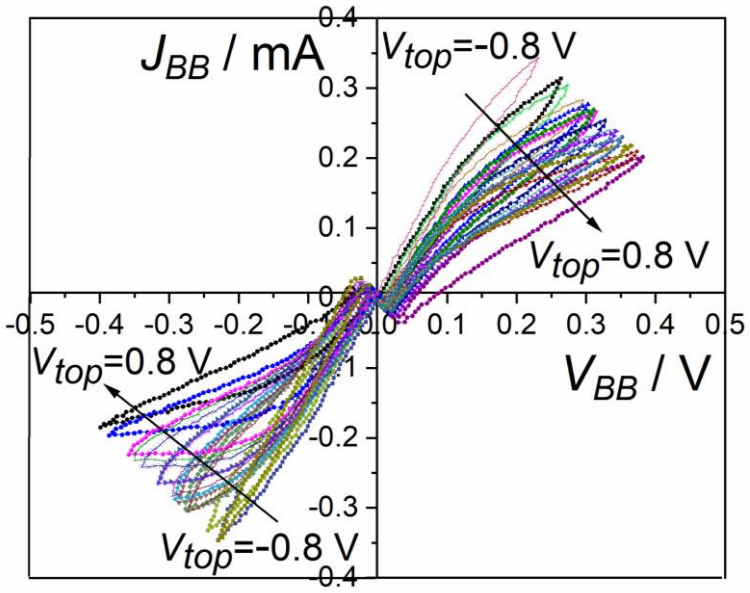

Figure 2.21 Sym-BB output characteristics. V_{BB} was scanned whereas at the input fixed values of V_{top} were applied from -0.8 V to 0.8 V.[56]

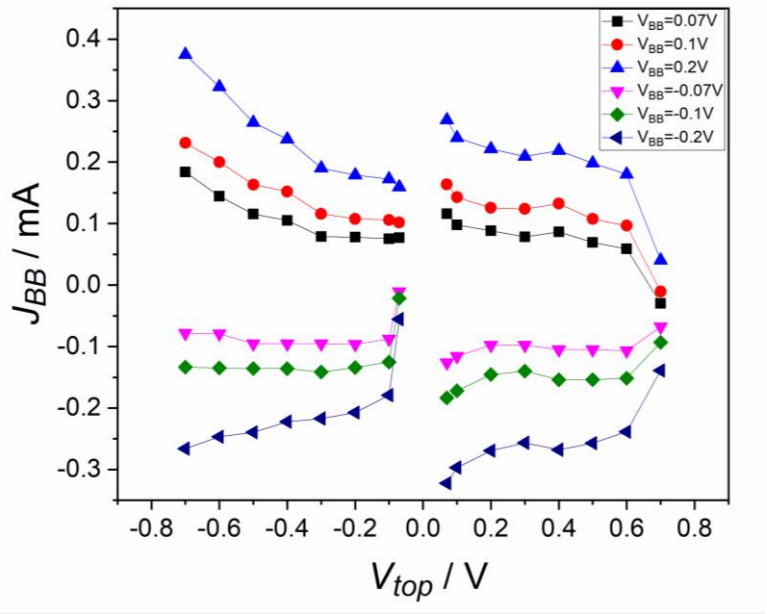

Figure 2.22 Transfer curve. [56]

It is worth mentioning that this calculation slightly deviates from the commonly used Eqn. 2.1.

$$g'_m = \frac{J_{out}}{V_{in}} \qquad (2.1)$$

$$g_m = \frac{\partial J_{BB}}{\partial V_{Top}} \qquad (2.2)$$

$$g_m = \gamma_{BB} \times V_{BB} \qquad (2.3)$$

Where γ_{BB} is a specific transconductance. Figure 2.23 shows the calculated g_m at different values of V_{BB}. The resulted values are significantly higher than the known ionic transistors. For example, the electric double layer transistor has values of 0.024 mS and 0.17 mS [85, 86]. The output voltage has an interesting dependence on the transconductance that can be expressed with Eqn 2.3.

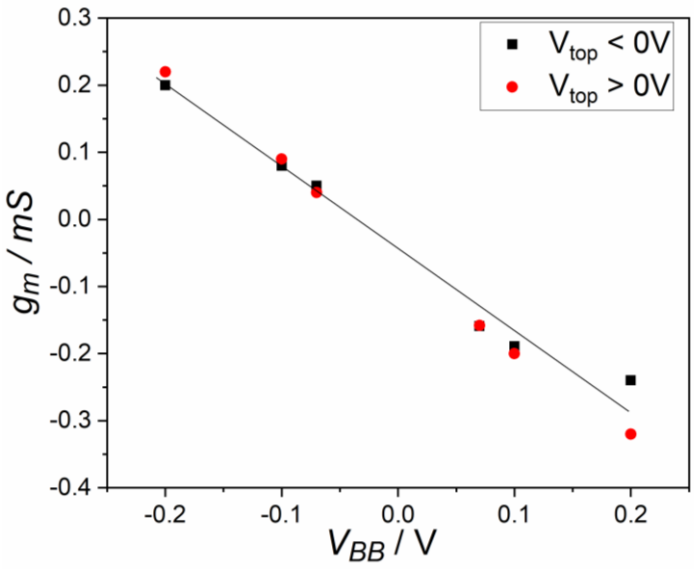

Figure 2.23 Differential transconductance calculated from Eqn 2.2 at small values of V_{BB}. As shown in the appendix D, five similar samples have shown nearly the same characteristics. [56]

2.4.2.2 Resistance control

Figure 2.21 shows an ohmic behavior of the output that resembles a resistor. This leads to the possibility of directly measuring the resistor using an ohmmeter. Using an ohmmeter instead of the *JV* analyzer not only provides a quick and simple way of measurement, but also avoids the problem of possible ground interconnection effects between the different parts of the setup. The configuration shown in Figure 2.24 was used to make the measurements. A fixed voltage was applied to the top electrode and the resistance reading was taken from the ohmmeter. Mostly, a top voltage ranging from 0 to 0.8 V was applied with a step of 0.1 V. Then, the voltage was decreased back to 0 V with a step of 0.1 V. The same process was repeated with a negative voltage up to -0.8 V.

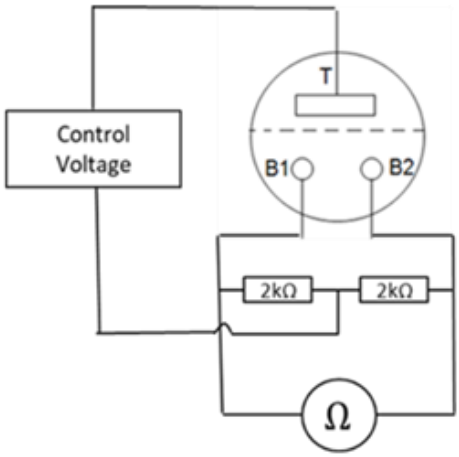

Figure 2.24 Resistance control configuration using a multimeter to measure R_{BB} [56]

In all the measurements, the 0.8 V was not exceeded to assure that there is no chemical reactions taking place on the device. Figure 2.25 shows the resulted curve. When the voltage applied on the top electrode is positive, the resistance between the two bottom electrodes increased to the highest values up to 3 kΩ. When the voltage applied on the top electrode is negative, the resistance R_{BB} decreased to nearly zero.

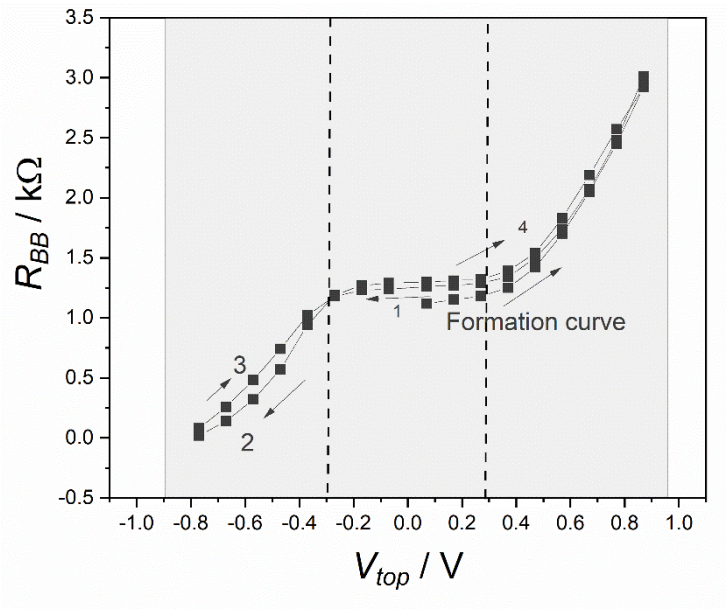

Figure 2.25 The resistance between the two bottom electrodes at permanent top voltage measured in a pulsed manner with about 10 s waiting time after every V_{top} change. When a positive voltage is applied on the top electrode, R_{BB} increases and when a negative V_{top} is applied it decreases. The dashed lines indicate the range of low top-electrode current .[56]

The resulted curve in Figure 2.25 can be divided into two parts the middle part where V_{top} = -0.37 V to 0.5 V and the corresponding outer part. The middle part of Figure 2.25 shows a very small change of the resistance. As shown in Figures 2.20 and 2.21, the input current is very low in comparison to the output current. This relation can be interpreted as the amplification as explained in the next section.

2.5 Amplification behavior

In general, amplification is the ratio between the output values to the input values. [84] The previous section indicated the possibility to use the IVEST as an amplifier. However, this can only work at a specific working point (WP) where the input current is really low in comparison to the output current. This amplification can be called current amplification or *J*-amplification as it is a relation between output and input current. The amplification was investigated based on Eqn. 2.4. Eqn 2.5 describes how the amplification is influenced by the system parameters at a given working point (WP). The deviation of Eqn. 2.5 can be found in Appendix D.

$$\beta_{d,WP} = \frac{\partial J_{out}}{\partial J_{in}} \qquad (2.4)$$

$$\beta_{d,WP} = \gamma_{BB}(V_{top}) \frac{V_{BB}}{G_{d,top}(V_{top})} \qquad (2.5)$$

The resulted amplification from a non-optimized device at WP1= (-0.37 V, 0.25 V). Here, the first value of this pair WP = (V_{top}, V_{BB}) describes the input voltage and the second one the output voltage. The amplification before tuning was around 10. The highest amplification reached after tuning = 52.9. This tuned amplification was achieved through systematic attempts as discussed in the following section.

2.5.1 Amplification tuning

In order to increase the amplification, a series of tuning attempts were made. The IVEST offers a range of tuning possibilities, starting from adjusting the thickness of the TiO_2 layer on the top electrode to changing the electrolyte concentration and the spacer pore size. Regarding the amplification, it was anticipated that two factors would have a significant impact: the dilution of the electrolyte and the thickness of the TiO_2 layer on the top electrode. For the following discussion, a specific working point, namely WP1, was chosen with V_{top} = -0.37 V and V_{BB} = 0.25 V. It is worth noting that at this particular point, we observed the maximum amplification effects among all the values we measured.

The first systematic tuning series involved varying the dilution of the electrolyte. Figure 2.26 illustrates that as the electrolyte is diluted, the resistance increases due to a decrease in the number of ions presents in the electrolyte. Figure 2.26 also shows with increasing the dilution factor, the slope of the curves also changes.

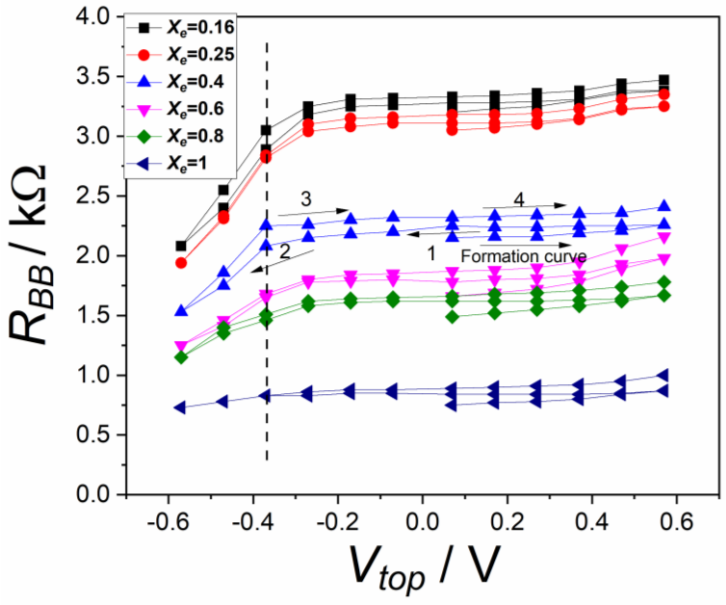

Figure 2.26 Effect of electrolyte dilution on the resistance between the two bottom electrodes.[56]

Figure 2.27 demonstrates the impact of the electrolyte dilution factor X_e on the amplification. The graph shows a trend where the amplification increases with dilution, until it reaches a peak point. Then the amplification undergoes a gradual decrease as the dilution factor continues to rise. This result highlights the relationship between the electrolyte dilution factor and the amplification, emphasizing the delicate balance required to achieve optimal results.

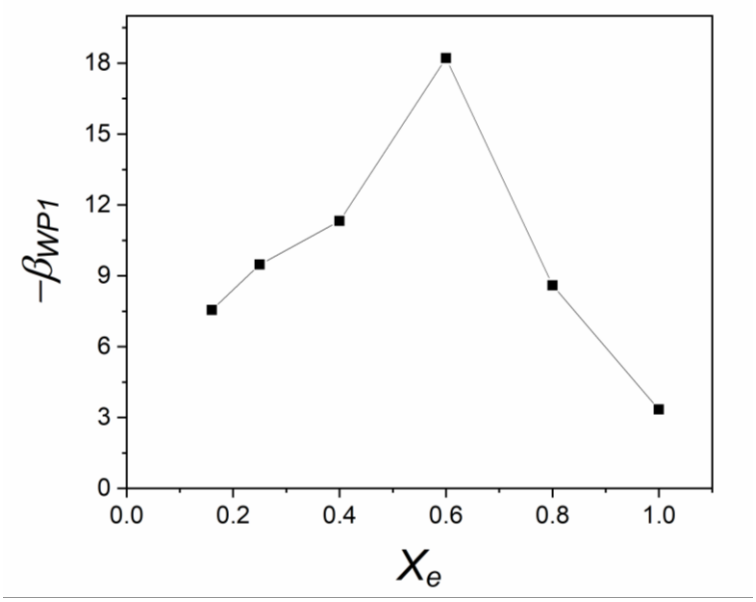

Figure 2.27 Effect of electrolyte dilution on the amplification calculated at WP1 based on Eqn 2.5.[56]

The second factor having an impact on the amplification is the thickness of the TiO_2 layer on the top electrode (X_{TiO2}). When the thickness of the TiO_2 layer on the top electrode decreases, the resulting amplification increases as shown in Figure 2.28. This could be attributed to an excess of TiO_2 particles that are not in contact with the electrode, referred to as the "dead material." However, this dead material is capable of adsorbing electrolyte ions. Since it lacks electrical contact with the top electrode, it may have a negative effect on amplification. These ions are not available for other processes. Thinner TiO_2 layers can be achieved using the method described in section 2.2.

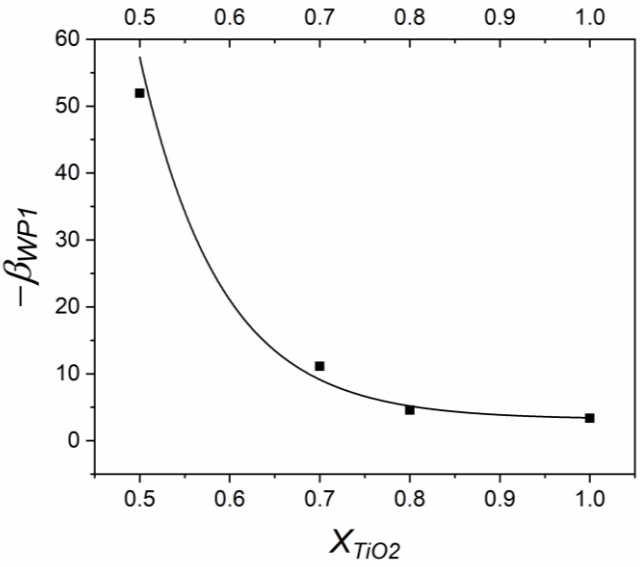

Figure 2.28 Effect of the thickness of the TiO_2 layer on the amplification. The thickness scale was constructed from two SEM investigations of the electrodes.[56]

2.5.2 Amplification mechanism and the working point

The results in the previous section show that the amplification depends on the WP. The highest amplification was reached at WP1 with V_{top} = -0.37 V for the investigated voltages.

When the semiconductor material meets the electrolyte, it can create an electronic depletion zone within the semiconductor material (TiO_2).[87] This depletion zone, similar to a Schottky contact, the Fermi energy of the metal is replaced by the redox couple energy level as shown in Figure 2.29. [88] The presence of this depletion zone near the electrolyte results in a positive charge, which is compensated by the formation of different ionic layers in the electrolyte. These ionic layers contain an excess charge opposite to the positive charge of the semiconductor and also include additional electrolyte ions for charge screening. This concentration of ions near the electrode surface can be seen as a variable storage. The stored ions in this layer affect the B-part of the IVEST, leading to changes in BB-resistance. Altering the potential can modify the depletion layer, causing changes in the ionic adsorption layer and subsequently altering the ion concentration in the B-part of the device, resulting in resistance changes. Since the adsorption/desorption phenomena have minimal current flow, the input current is low, while

the output current is primarily determined by the output voltage. Therefore, the output current is typically not low.

The Mott-Schottky theory can be used for a quantitative evaluation.[24] In addition Eqn. 2.6 is assumed to be the basic equation combining the semiconductor with the electrolyte is:

$$N_E = en_d Aw\gamma \qquad (2.6)$$

Where $N_E$is the total number of additional ions bound near the electrode, γ is the enhancement factor between the number of depleted electrons and the number of ions involved in the charge compensation, and w is the width of the (electronic) depletion zone. The equation presented here illustrates the phenomenon where the reduction in electronic charge is compensated by the presence of ions. These ions are attached to the upper electrode and do not contribute to the conductivity of the electrolyte in regions slightly distant from the upper electrode. In the case of an open separator, these ions directly decrease the ion concentration throughout the electrolyte, resulting in an increase in resistance in the B-part resulting in Eqn 2.7 for $V_{top} > V_{fb}$.

$$G_{BB} = G_0 - \alpha_1(V_{top} - V_{fb})^{1/2} \qquad (2.7)$$

Equation 2.8 can express the specific transconductance. Which is a result of using the flat-band potential V_{fb}, an appropriate constant α_1 and an explicit expression for w was used which has adjusted from the Mott-Schottky theory and with another constant α_2.

$$\gamma_{BB} = \frac{\partial G_{BB}}{\partial V_{top}} = \alpha_2(V_{top} - V_{fb})^{-1/2} \qquad (2.8)$$

From equation 2.8, we can say that the depletion layer vanishes near to the flat band potential. This explanation is similar to the Mott-Schottky formula.[24] This explains the high amplification resulted at the WP1 = -0.37 V which is near to the flat band potential. On the other hand, in this region also the conductivity of the interface rises. Therefore, the optimization of the amplification is a delicate balance between increasing the transconductance and keeping the resistance high. Achieving optimal amplification requires a careful equilibrium between enhancing the transconductance and maintaining a high resistance level as the conductivity of the interface also increases in this particular region.

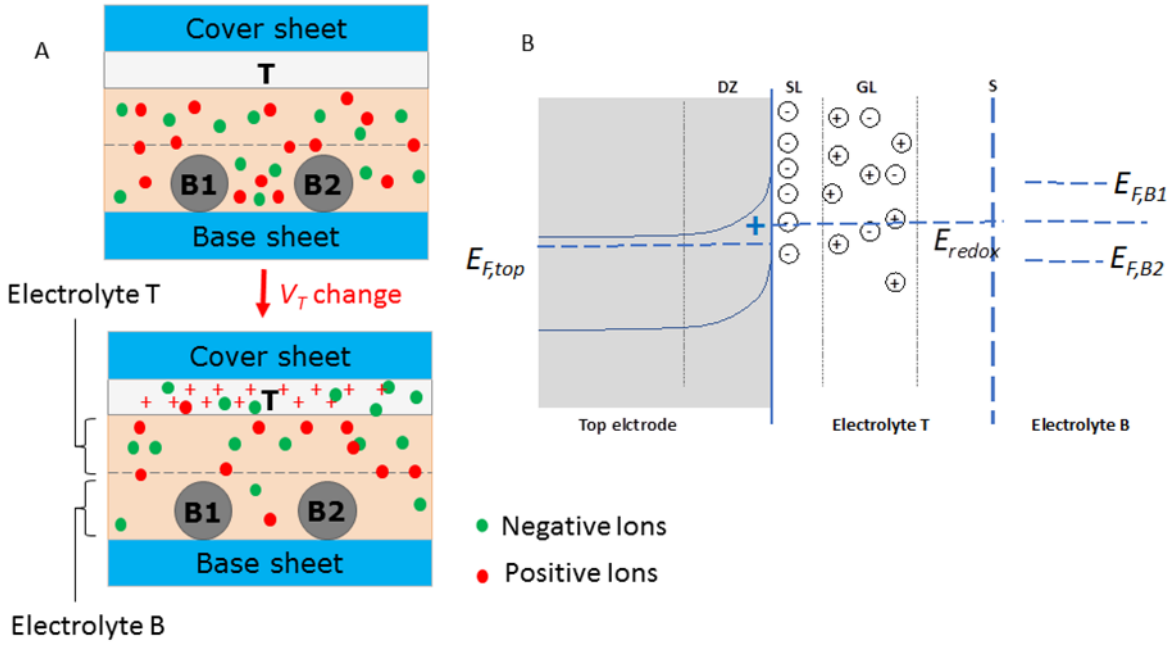

Figure 2.29 Schematic description of the mechanism of the device. (B) Energy levels of the IVEST and ions form the electrolyte. The image shows the electronic depletion zone (DZ), the Stern layer (SL), the Gouy layer (GL), and the separator (S). The left half of Fig. 2.29B shows the classical description of a semiconductor electrolyte interface as e.g. in ref.[88]. The right half shows the proposed coupling to the bottom part of the electrolyte. External voltages generate the Fermi energy offsets.[56]

2.6 The potentiometric effect

The IVEST's main operation modus can be considered as a potentiometer with external control voltage. Figure 2.25 shows the strong nonlinear effect of the control voltage. A part of these effects is instantaneous, and another part can be modified by a waiting time. Based on this result we can ascribe two mechanisms that contribute to the effect. The first one is the ion adsorption on the top electrode. The mesoporous TiO_2 layer on the top electrode can adsorb ions by applying $V_{top.}$ The voltage as discussed in section 2.5.2 can control this adsorption. The second mechanism is the ion transport through the membrane. As the pore size of the membrane goes down it hindrance the ions diffusion. The instantaneous effect can be good to construct an amplifier. Using a relatively long writing period, the transport phenomena become dominating. The nonlinearity of the control current dependent on the control voltage might be considered as a useful feature. It creates an in-build threshold switch or, more generally, an activation function in neural networks. The basic potentiometer characteristics in the output are well suited for perceptrons or neuromorphic networks for realizing signal weighting.

2.7 Memory effects

When we look at the resulting characterizations of the IVEST using both the *JV* analyzer and the ohmmeter in section 2.4, we can see a hysteresis. This hysteresis, at first glance, seems to be a drawback of the device. However, this hysteresis means that there is a delay in the diffusion of the ions; not all the ions can drift back to the original state after each measurement. Enlarging this hysteresis can lead to a significant memory effect. In this section, the memory effect of the IVEST is investigated and tuned.

A special measurement was designed to investigate the memory effect as shown in Figure 2.30. The configuration shown in Figure 2.24 is used to perform this measurement. For the first two minutes the resistance was measured each 20 s. Then a positive voltage V_{top} = 0.8 V was applied on the top electrode for 1 min. After 1 min the voltage was switched off and the resistance was measured each 20 s for 2 min. The resulted resistance was higher than the original resistance before applying any voltage we can say the device became to a high resistance state (HRS). After that a negative voltage V_{top} = -0.8 V was applied for 1 min and after switching off the voltage the resistance R_{BB} was measured each 20 s for 2 minutes.

Clearly, the IVEST can remember the writing and the device can either be in a high or low resistance state as shown in Figure 3.30. Small changes also exists in each state, however the memory effect is not lost. As observed in Figure 2.30 the high and low resistance states are stable with a difference up to ΔR_{BB} = 0.56 kΩ. The memory contrast is the ratio between the high and the low resistance states. It can be used to investigate the quality of the memory effect as shown in Eqn 2.9.

$$\alpha = \frac{H}{L} = \frac{R_{BB}^{H}}{R_{BB}^{L}} \qquad (2.9)$$

For the device represented in Figure 2.30 the memory contrast reached 1.3.This ratio is enough to be utilized in a circuits.[62]

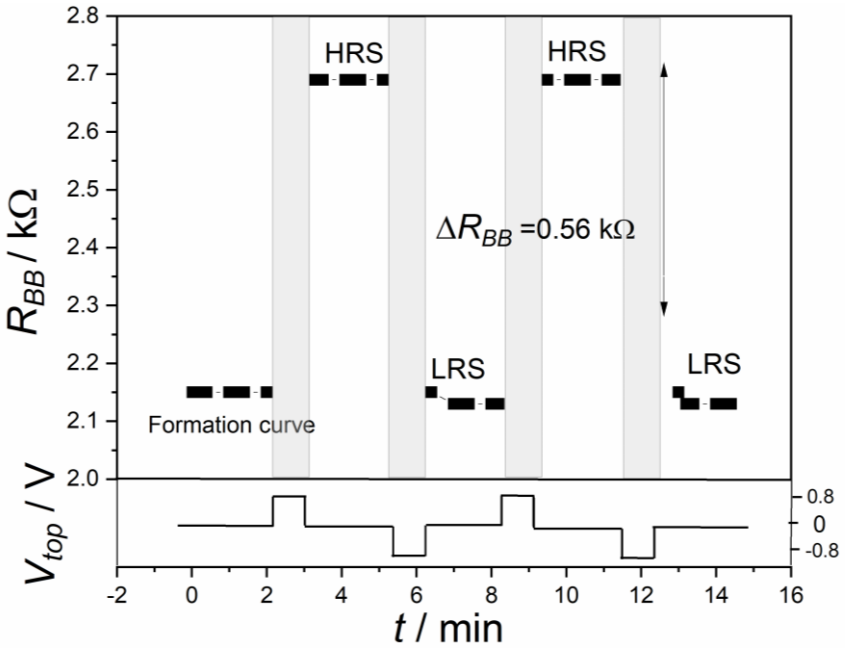

Figure 2.30 Switching measurements with a voltage protocol shown in the lower part of the diagram [56]

2.7.1 Memory tuning

As stated in previous sections, the construction of the IVEST exhibits a wide range of tuning possibilities. To tune the memory effect three key factors were investigated. The first factor that played a role in the tuning of the memory effect is the pore size of the membrane.

Initially, the inclusion of a spacer was imperative to prevent any potential shortcuts between the electrodes. However, upon removing the spacer and employing a membrane with smaller pore sizes, a notable increase in the memory effect was observed. As shown in Figure 3.31A decreasing the pore size of the membrane increased the difference between the high and low resistance states.

The second physical quantity that showed a big improvement with using a smaller pore size membrane is the stability time. Stability time τ_2 is the time the device can stay for either at the high resistance state or the low resistance state. The stability time is discussed in section 2.7.3 in more detail. This increase in the stability time could be a result of the slow redistribution of the ions caused by the presence of the membrane. Figure 2.31B represents the increase in stability time in the relation with the membrane pore size.

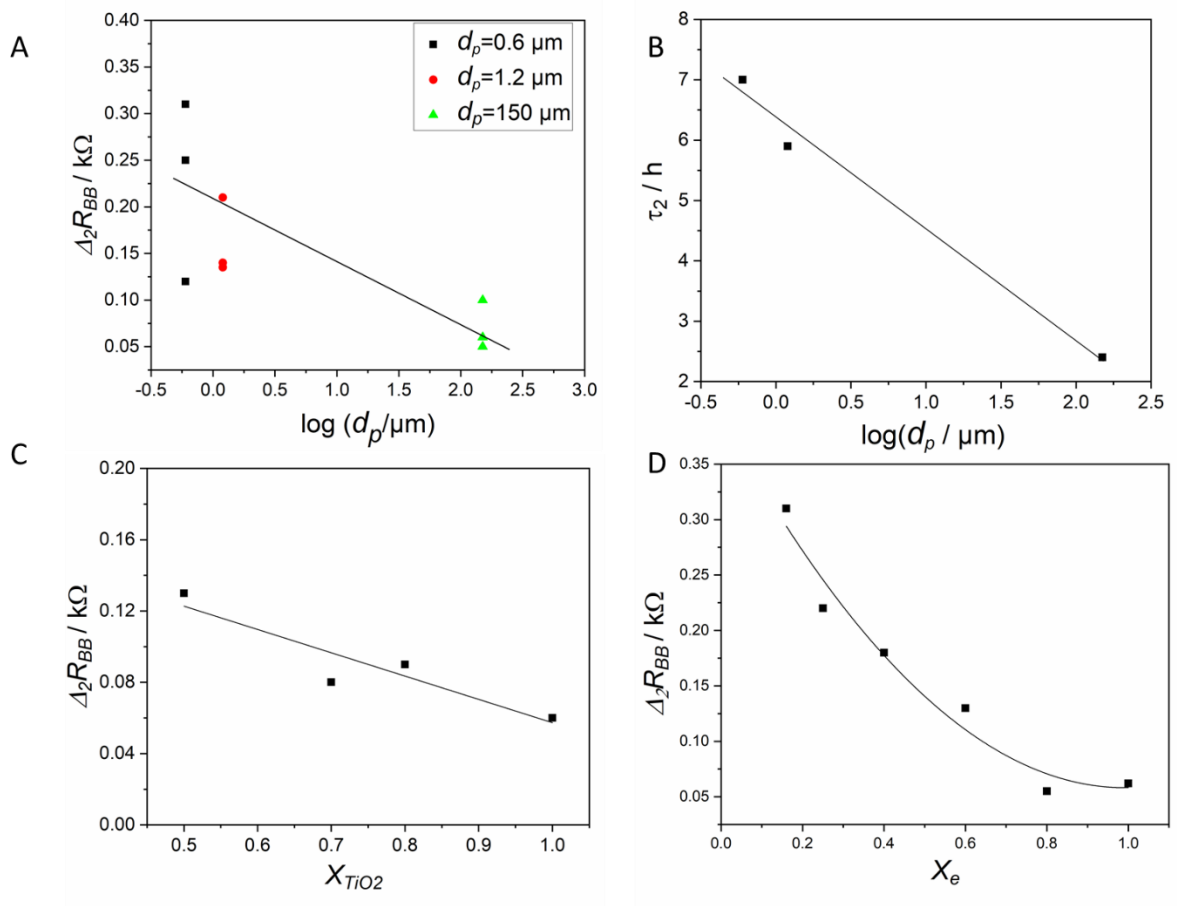

Figure 2.31 (A) Effect of membrane pore size on ΔR_{BB}.Where delta is the difference between HRS and LRS (B) Effect of membrane pore size on the stability time (C) Effect of the thickness of TiO_2 layer on ΔR_{BB} (D) Effect of electrolyte dilution on ΔR_{BB} [56]

Another factor that has an effect on the memory effect is the thickness of the TiO_2 layer on the top electrode. Figure 2.31C shows that, when the thickness of the TiO_2 layer on the top electrode was decreased by diluting the TiO_2 suspension, the difference between the two memory states ΔR_{BB} increased. This could be a result of the dead material on the top electrode as stated in section 2.5.1.

Finally, the last factor investigated to tune the memory effect was the electrolyte dilution factor. As shown in Figure 2.31D, when the electrolyte was diluted ΔR_{BB} increased.

After tuning an optimized device showed ΔR_{BB} = 0.56 kΩ and τ_2 = 5.8 h, leading to a contrast factor of α = 1.3.

2.7.2 Memory effects and the role of membrane

To understand the memory effect in the device, the IVEST can be divided into two parts as shown in Figure 2.32. Part one consisting of the top electrode and the upper part of the

electrolyte (T-part). Part two consisting of the two bottom electrodes and the electrolyte surrounding them (B-part). The main memory effect comes from the difference of ion concentration between T-part and B-part. By applying a voltage on the top electrode, ion gradients are formed in the electrolyte creating a difference of ions concentration between the two parts of the device. These ions need time to redistribute again through the device and this time is called the stability time τ_2. Figure 2.33 shows a brownish color between the two bottom electrodes. This coloration is observed when a voltage $|V_{top}| > 0.6$ V is applied on the top electrode. The observed coloration strongly suggests the accumulation of triiodide or polyiodides near the bottom electrodes. Additionally, it is highly likely that there are depletions of I_3^- and the formation of iodide ion gradients.

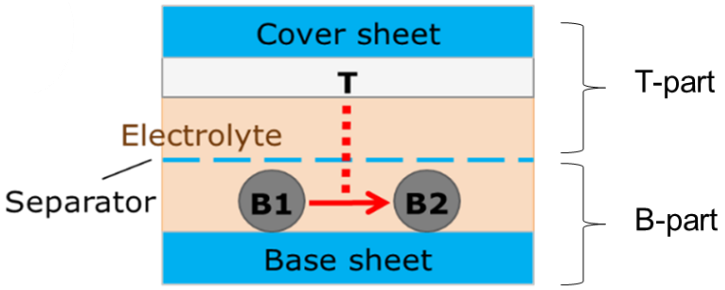

Figure 2.32 Schematic description of the two parts of the IVEST [56]

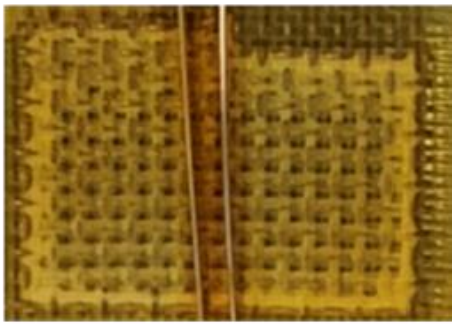

Figure 2.33 Coloration around the two bottom electrodes at $|V_{top}| > 0.6$ V[56]

The top electrode and the membrane both play a role on the memory effect. Despite the membrane pore size has more impact on the memory, the top electrode proved also to play a significant role as shown in Figure 2.31C. When the thickness of TiO_2 layer decreased, ΔR_{BB} increased. On the other hand, membrane slows down the redistribution of ions between the T-part and the B-part of the device. As a result, the lifetime of the non-equilibrium state increases represented by the increase in the stability time as shown in Figure 2.31B. The small pore size

membrane has effect also on ΔR_{BB} represented on Figure 2.31A. When a membrane with pore size 1.2 µm was used ΔR_{BB} increased by a factor of five.

2.7.3 Adaptation, stability time of memory states and physical effects

Both the high and low resistance state are metastable states. In each state, there is two kinetic processes with different time constants as presented in Figure 2.34. The first process is called the adaptation time τ_1, which happens only on the first two minutes directly after the writing process. The gradients created during writing might be responsible for this relatively fast decay. Then after the first two minutes, a second process has a time constant τ_2 that is called the stability time and determines how long the state can be used for storing information take place. To calculate the stability time the difference between the sum and the difference of the two states was fitted using OriginLab as explained in Appendix E. The resulted stability time up to 6 h shows a useful memory device.

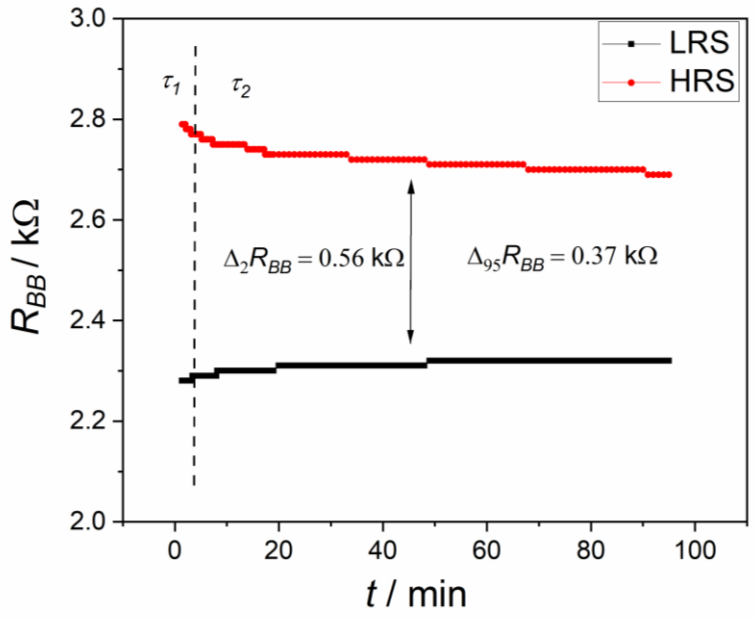

Figure 2.34 The high resistance and low resistance states of the device observed over 95 h. With a separator pore size of 1.2 mm, an electrolyte with Xe = 0.16 and a titania layer with X_{TiO2} = 0.5[56]

To understand the dynamics of both states, the same physical picture as in section 2.6 can be used with focus on the redistribution of I_2. When the concentration changes, the triiodide ions will be depleted in the B-part that consists of part of the electrolyte and the bottom electrodes. It is necessary to take into account that the resistance between two electrodes consists of different parts: the two electrode surfaces including the ion layers in the electrolyte and the volume contribution of the electrolyte. Whereas the volume contribution is not strongly

dependent on the kind of ions, the electrode contributions are very sensitive. The exchange of I_3^- with I^- has a dramatic effect on the redox reactions and, therefore, on the electrode resistance. For a quantitative estimation of such effects, one can use models as e.g. described in ref. [89].

When we apply voltage, triiodide and other polyiodides are generated in the electrolyte, thereby contributing to the overall reaction. However, it is worth noting that triiodide exhibits the most significant impact, which allows us to label the proposed mechanism as 'redox oxidizer depletion'. As we reach the maximum voltage, a process of accumulation and depletion occurs between the two components of the device. Initially, during the readout process, these gradients gradually diminish, and we attribute this phenomenon to the typical time τ_1. As the readout phase progresses, the inter-part gradients become the primary focus, influencing the decay time τ_2. At this point, one might attempt to estimate the stability time based on the size of the membrane pores. However, it is important to consider that our measured dependence encompasses not only variations in pore size but also changes in thickness and material composition. As a result, achieving quantitative agreement becomes challenging. Furthermore, the investigation of other ionic gradients is still under investigation.

2.7.4 Partial Switching

The partial switching is the ability to switch between the achieved high resistance state and low resistance state partially with shorter periods. Possible partial switching of the device by changing the time of the writing was investigated. The partial switching can be used to test the sensitivity of the device by noticing the effect of applying top voltage for a shorter period. Also a multilevel device could be also good for computational applications when the resistance of the device can be changed in small steps this allows for a multi-bit representation.[55]

Figure 2.35 shows the partial switching of the IVEST. In this graph, first a formation curve was measured with applying no voltage on the top electrode. Then two measurement set were made. The first set was measured by applying a positive voltage V_{top} = 0.7 V is applied for 1 min. Then the reading between the two bottom electrodes were measured for 2 min. A negative voltage was then applied for 1 min V_{top} = -0.7 V. Again, the resistance between the two bottom electrodes were measured for 2 min. This measurement were made for 2 cycles. We can see in Figure 2.35 the resulted states (HRS1 and LRS1).

To reach a partial switching the same measurement was made but with writing time of 30 s. Figure 2.35 shows the resulted states of the less writing time (30 s): HRS2 and LRS2. Obviously increasing the writing time results in bigger ΔR_{BB}.

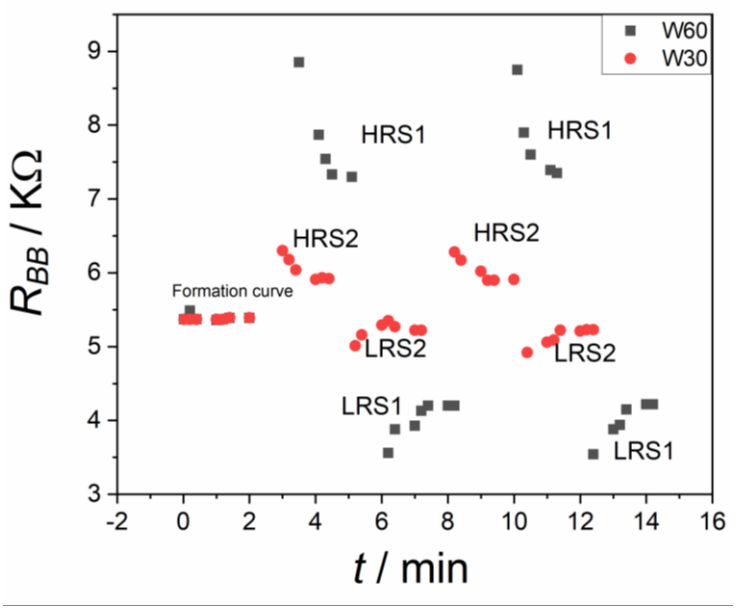

Figure 2.35 Switching between the HRS and LRS using different writing times.

2.8 Conclusion

A new purely ionic soft triode was invented. [56, 73] The IVEST has memory and amplification characteristics. As conclusions of our investigations, we realized two main physico-chemical principles in the device, ion adsorption in a porous electrode and redox oxidizer depletion. A wide range of chemical tuning is enabled by both principles. The main operation scheme of the device is to control the resistance between the two bottom electrodes by varying the voltage on the top electrode.

Different tuning factors were studied. The amplification of the device was optimized and reached a value of β = 52. The memory effect was tuned and reached $\Delta_2 R_{BB}$ = 0.56 kΩ and τ_2 = 5.8 h by using a membrane with a pore size of 1.2 µm, and a diluted electrolyte (16% of our standard) and a thinner TiO_2 layer (of about 10 mm). The high stability time of the device allows it to be used as a memory element in different applications such as sensor systems, [90] health care applications [91] and neuromorphic memories. This device could be a building block for neuromorphic information processing systems and could, therefore, be a step towards a new computational technology.

The IVEST offers numerous advantages when compared to existing devices, including the potential for a green fabrication involving no high-temperature steps, the possibility of incorporation into printable electronics, and the low power consumption of such devices. It is important to note that there is no necessity to use a semiconductor material in order to have a channel between the bottom electrodes, which would lead to an increase in financial and ecologic production costs. Although liquid electrolytes may appear to be a disadvantage, widely used devices such as batteries and electrolytic capacitors demonstrate that the technical requirements can be effectively managed. Furthermore, solid or gel electrolytes can also be used in these devices. From a device perspective, it is intriguing that the IVESTs possess a controllable linear ohmic output. This sets them apart from known devices that exhibit non-linear output characteristics.[56] However, this distinction allows for the implementation of modified circuit layouts.

3. Iontronic memories: Operation protocols

Most of the content of this chapter was published as "Iontronic memories based on ionic redox systems: operation protocols" Mohamed, E., Tchorz, N., & Marlow, F. (2023) Faraday Discussions. The main part of the text, as well as the figures of the following section, are reprinted and reproduced with permission from Royal Society of Chemistry [76]

3.1 Introduction

Different iontronic memristors based on ionic liquids have been previously reported [92, 93]. Liquid electrolyte redox systems can offer promising performance for the devices due to high-speed faradaic reactions and a very high pseudo-capacitance[94]. Such systems may lead to neuromorphic soft materials and a better understanding of the human brain. More investigations for the liquid electrolyte redox systems still need to be performed.

In our system, we cannot measure the same thing twice unless we use a well-defined characterization protocols. A measurement protocol is a uniquely defined series of processes with fixed periods to perform a specific measurement. When e.g. a resistance at a specific point is measured several times, it will gradually change as shown in Figure 3.1. A well-defined protocol is essential to have stable reproducible results and to get higher performance from the device. From the investigations in chapter 2, the IVEST has both amplification and memory characteristics. However, the memory effect seems to be more significant and interesting from the current point of view. In the following chapters, only the memory effect will be further investigated.

The IVEST has a memory that can last up to 6 h. An important drawback of the IVEST's memory is, however, the low memory contrast. Therefore, in this chapter, we aimed to increase the performance of the device and the memory contrast through strict measurement protocols accompanied with a new circuit configuration. This was also achieved by the investigating a modified system (a pentode) instead of the IVEST (a triode). As the construction of the IVEST allows the device to be built with more than two bottom electrodes, it was helpful for understanding the mechanism inside the device to investigate a system with four bottom electrodes as discussed in the following subsections.

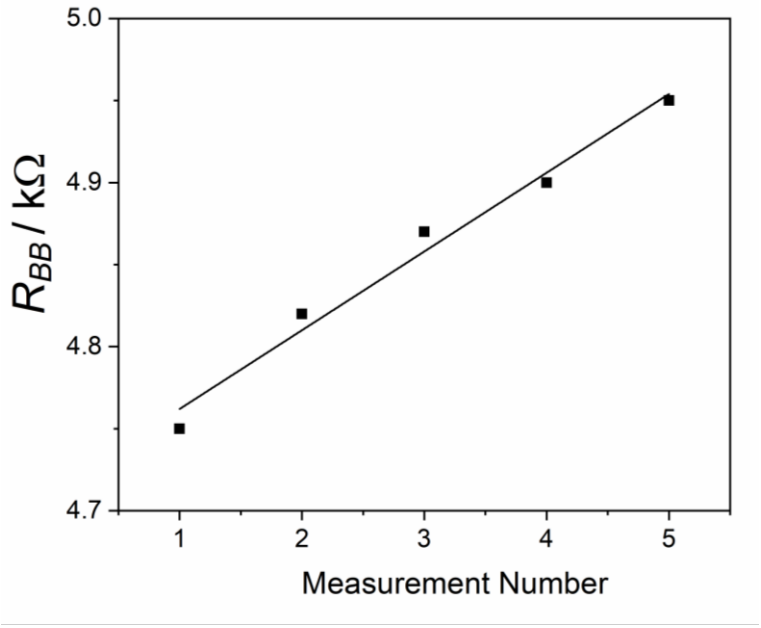

Figure 3.1 R_{BB} measurement in a raw.

3.2 The pentode [95]

The Pentode was constructed in the same way like the IVEST as described in section 2.3.2. The optimized TiO_2 suspension and fabrication method B were used. The only difference is the using of four bottom electrodes instead of two as shown in Figure 3.2. Figure 3.2A shows a schematic description of the pentode with four bottom electrodes and one top electrode. All electrodes are separated with a membrane and after sealing the device, a redox couple electrolyte is injected inside the device using the same technique as in section 2.3.2. Figure 3.2B shows the final look of the pentode after construction and fixing on a top of an electronic breadboard.

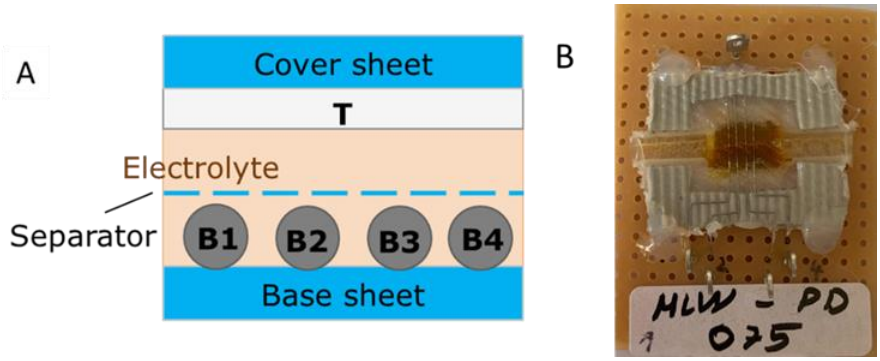

Figure 3.2 (A) Schematic description of the pentode. (B) Final look of the pentode.

3.2.1 Device and measuring setup

To investigate the behavior of the pentode, first, the resistance between each couple of the bottom electrodes was measured. To perform this a multimeter and a special switch are used as presented in Figure 3.3. A special electronic switch (MLW-FB-047 See Appendix F) was added to be able to measure the resistance in a pulsed way with a well defined period of 1.5 s. This defines the charge amount that is injected in every resistance measurement to a fixed amount of 15 µC.

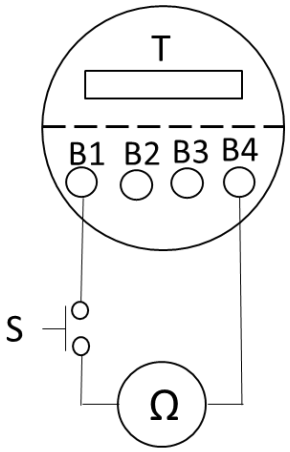

Figure 3.3 Schematic description to the configuration used to measure R_{BB} between the different bottom electrodes of a pentode.

3.2.2 R_{BB} matrix measurements

3.2.2.1 Numerical sequence matrix

The resistance between each bottom electrode pair was measured as described in table 3.1 with a chosen sequence using the circuit shown in Figure 3.3. After connecting the electrodes, the switch is closed for 1.5 s. The red color refers to the electrode connected to the positive terminal of the multimeter and the black color refers to the negative terminal. The resulted R_{BB} measurement from this numerical sequence is shown in Figure 3.4.

Table 3.1 Description of the “numerical” sequence (“num Seq”). The number in the table is the measurement number.

	B1	**B2**	**B3**	**B4**
B1	X	1	2	3
B2	4	X	5	6
B3	7	8	x	9

B4	10	11	12	X

From Figure 3.4, the resistance between each pair of electrodes changes even without applying any voltage to the top electrode. For example, the resistance between R_{B1B2} differs from R_{B2B1}. The distance between each electrode and the next one was fixed to 1 mm. One could expect that when the distance between each pair of electrodes is the same, the resistance between them should be nearly the same. However, this is not the case as shown in Figure 3.4.

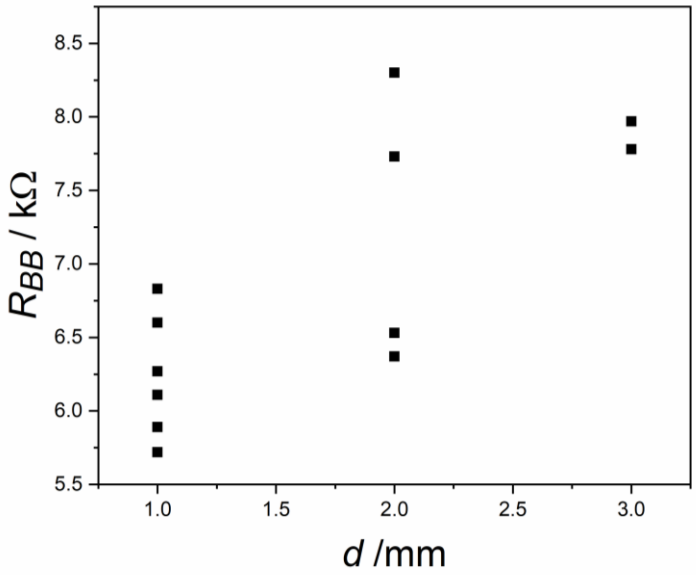

Figure 3.4 R_{BB} measurement using numerical sequence as shown in table 3.1. Representation depending on the distance between the different B electrodes *d*. Used configuration as shown in Figure 3.3.

When we deeply look at Figure 3.4, we see also the change when more than one measurement are applied in a raw between the same bottom electrodes. When we examine the factors that may cause these changes, one can identify three main factors for changes in one pair of electrodes: the number of connection changes (steps), read-out polarity, and memory effects. Furthermore, two factors contribute to variations between different electrode pairs: air bubbles and fabrication inaccuracies. In the upcoming sections, we tried to detangle the results and investigated each factor that can affect the R_{BB} measurements.

3.2.2.2 Interconnection steps and polarity

When the electrolyte is injected in the device, an electric double layer is created around each electrode. To measure the resistance the multimeter injects a specific current the used multimeter injects a charge of 15 µC inside the system then it measures the voltage. From the voltage, it calculates the resistance. This current injected inside the system, can make changes

in these double layers or its surroundings as shown in Figure 3.5. It likely creates a depletion of ions at the involved electrodes. As a result, during the next R_{BB} measurement, the system is not the same any more. There is a disturbance and especially an ionic depletion in the system. The concentration of the ions around each electrode is not symmetric between the electrodes anymore.

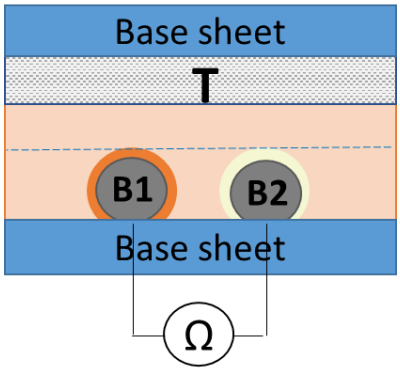

Figure 3.5 Schematic description to the effect of current injected by the multimeter on the bottom electrodes.

When we take a deeper look on the results in Figure 3.4, one can see the relation between the steps made to take the measurement and the resulted R_{BB}. The results with one-step has less difference in R_{BB} values than when more than one step is made. Different measurement sequences can be applied to investigate the effect of the steps. In our case, we have 720 possible sequences (6! = 720). Since it is impossible to test all these sequences, we chose two special sequences that can help investigate the effect of the number of steps and polarity. The first sequence we can call the 9^7 sequence. This name was adapted from the shape resulted from the measurement steps table 3.2. In this sequence, the least number of steps is made when the measurement is switched between each couple of electrodes. In sequence 9^7, the number of steps is decreased, as shown in Table 3.2.

Table 3.2 The 9^7 sequence

	B1	**B2**	**B3**	**B4**
B1	x	1	2	3
B2	8	x	9	4
B3	7	6	x	5
B4	12	11	10	X

To control the polarity effect, another sequence was used which called 8jump sequence. In the 8jump sequence we measure the resistance between two electrodes and then measure again but with opposite polarity. The aim of the 8jump sequence was to cancel the effect made by each measurement by opposing the polarity as shown in Table 3.3.

Table 3.3 The measurement sequence 8jump

	B1	**B2**	**B3**	**B4**
B1	x	1	-	7
B2	2	x	5	-
B3	-	6	x	3
B4	8	-	4	x

Figure 3.6 shows the resulted R_{BB} measurements from 9^7 and 8 jump sequence. One can see in Figure 3.6 that the resulted R_{BB} from the 9^7 and 8 jump sequences has less element variations than the numerical sequence in Figure 3.4. The sequence 8jump seems to suppress the variations in the R_{BB} elements even more.

The results from $\mathbf{R_{BB}}$ matrix indicate small secondary memories for each electrode (We should distinct this from the primary, T-induced memory). Each measurement depends on the history of the device. When the measurement is taken, each electrode remembers this measurement. This memory effect is obvious when we talk about the reproducibility of the measurement. With each measurement, we create a new state.

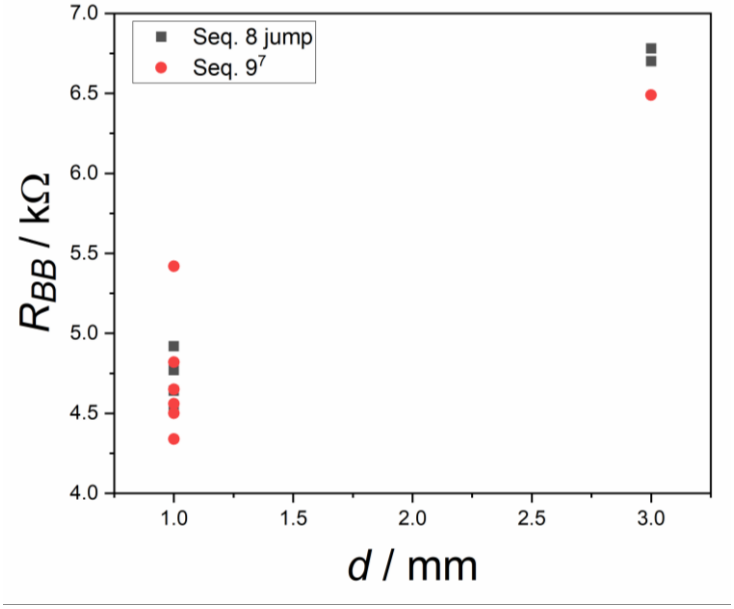

Figure 3.6 R_{BB} measured by the two sequences 8jump and 9^7

To have more control on these memories the secondary memories can be suppressed. One option is to use a short cut between the two bottom electrodes as storing phase to suppress these memories as explained in section 3.3.

3.2.3 $\mathbf{V_{BB}}$ matrix

A voltage measurement is considered a non-destructive method of measurement. There are several advantages to measuring the $\mathbf{V_{BB}}$ matrix. One advantage is that voltage allows us to detect gradients in the electrolyte. The concentration of ions is related to the voltage according to the Nernst equation (Eqn 3.1). From a practical standpoint, we now have an alternative type of readout. When we only have resistance measurements, we apply a current to the system with each measurement, which can alter the state each time. With voltage measurements, we eliminate these state changes and can maintain the state without causing any damage during the measurements. The potential difference between each pair of electrodes originates from changes in the concentration ratio of the redox couple. We begin with a certain concentration ratio of the redox couple and then modify this ratio near the electrodes by depleting or accumulating different ions. The increase in triiodide concentration can be observed through the brownish coloration between the electrodes, particularly at higher potential differences.

In order to measure the voltage matrix, two steps are needed. The first step is to create a disturbance in the system. Then detecting this disturbance by measuring the voltage. To create this disturbance, a resistance between two specific electrodes should be measured several times.

As with each measurement, a current is injected with charge of 15 µC. This current makes changes in the ion concentration around each electrode. At each time, the multimeter (IDM93N, RS PRO GmbH) used for measuring injects a small current that causes a change in the ions concentrations. This resistance measurement was done to a pentode where the resistance between B3 and B4 was measured 5 times as shown in table 3.4.

As one can see in table 3.4 with each time of measuring the resistance increases. At each measurement, more disturbance is generated in the system. Because of the depletion and accumulation of ions.

Table 3.4 R_{BB} repeated measurement

	1	2	3	4	5
R_{B3B4} / kΩ	4.75	4.86	4.95	5.05	5.18

The voltage between B3 and B4 was measured over 1.5 min in a pulsed way each 30 s as shown in table 3.5. This measured potential difference is a proof of the change of ions concentrations.

Table 3.5. Voltage measurement over 120 s after measuring R_{BB} five times in a raw.

t / s	0	30	60	90	120
V_{B3B4} / mV	2.8	2.3	2.1	1.9	1.7

When the entire matrix was measured in numerical sequence, as shown in Table 3.6, it revealed the presence of a measurable voltage between each pair of electrodes. The highest voltage was observed between B3 and B4, as this is where the initial destruction took place and affected the entire system. However, I did not observe any color change during these measurements. The change in concentration in this scenario is not significant enough to cause a visible coloration to the naked eye, as shown in Figure 2.33.

Table 3.6. $\mathbf{V}_{BB}$ matrix after making five R_{BB} measurements.

	B1	**B2**	**B3**	**B4**
B1	X	-0.2	-0.5	0.9
B2	0.1	X	-0.2	0.8
B3	0.5	0.3	x	1.5
B4	-1	-0.9	-1.5	x

The results in table 3.6 shows nearly symmetry against polarity change. We can say that we have a readout method beside the resistance measurement and it is destruction-free. However, it can only detect the secondary memory effects, but not the primary ones. May be a modified version of the voltage readout can be used for that.

3.2.4 Ion concentrations

The Nernst equation (eqn. 3.1) is one of the main equations in electrochemistry.[29] It allows the determination of cell potential under non-standard conditions. It relates the measured cell potential to the reaction quotient Q which is the ratio between the chemical activity of the reductant, R and the oxidant O[29]. During the reaction, the Nernst equation may be used to calculate the cell potential at any time and under any conditions other than the standard state as shown in equation 3.1. [24] .

$$E = E^0 + \frac{RT}{nF} lnQ \qquad (3.1)$$

Where E stands for the electrode potential, R for the gas constant, T for the temperature, F for Faraday's constant, E^0 is the standard potential which represents the power needed for any element or compound to be reduced under standard conditions (298 K, 1 atmospheric pressure) n is the number of electrons transferred in the redox reaction. In our system, a redox reaction occurs via two-electron transfer as shown in equation 3.2. There can be other polyiodides in the electrolyte during measurement but we neglect them here.

$$I_3^- + 2e \rightleftharpoons 3I^- \qquad (3.2)$$

From our measurement of V_{BB}, we have the possibility to calculate the concentration ratio of triiodide between two electrodes described as follows. In our measurement, there is no reference voltage. What is measured is not the potential of each electrode to a reference electrode it is the difference in potential between electrodes B3 and B4. The Nernst equation cannot be used

directly. In the following calculation, the ratio of the triiodide between two bottom electrodes at a specific potential difference is calculated:

$$\Delta E = E3\text{-}E4 = \frac{RT}{nF}\left(ln\ \frac{C_{I_3^-,B3}}{C_{I^-,B3}} - ln\ \frac{C_{I_3^-,B4}}{C_{I^-,B4}}\right) \quad (3.3)$$

$$\Delta E = \frac{RT}{nF} ln\ \left(\frac{C_{I_3^-,B3}}{C_{I^-,B3}} \Big/ \frac{C_{I_3^-,B3}}{C_{I^-,B4}}\right) \quad (3.4)$$

In these calculations, we can assume that the iodide concentration is nearly the same as we have much more than triiodide in our recipe. The iodine redistribution is not visible as it is a colorless ion. What we usually see at high voltages is the triiodide so we calculated what we normally see. Therefore, the final equation can be written as:

$$\Delta E = \frac{RT}{nF} \ln\left(\frac{C_{I_3^-,B3}}{C_{I_3^-,B4}}\right) \quad (3.5)$$

Let us chose a value of the potential difference between B3 and B4, and then calculate the ratio of triiodide concentration between the two electrodes resulting from history of readout processes. If ΔE = 2.3 mV, then

$$2.3\ mV = \frac{\left(8.315\frac{J}{K\,mol}\right)298K}{2(96.485\times10^3\frac{C}{mol})} ln\ \left(\frac{C_{I_3^-,B3}}{C_{I_3^-,B4}}\right) \quad (3.6)$$

$$ln\ \left(\frac{C_{I_3^-,B3}}{C_{I_3^-,B4}}\right) = 0.791 \quad (3.7)$$

$$\frac{C_{I_3^-,B3}}{C_{I_3^-,B4}} = 1.1961 \quad (3.8)$$

Figure 3.7 shows the ratio of the triiodide between B3 and B4 at different voltage values.

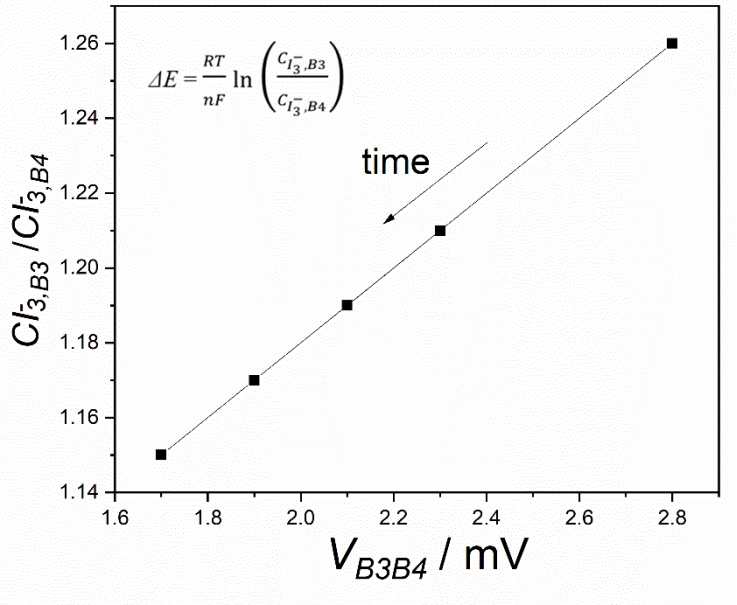

Figure 3.7 The relation between the voltage V_{B3B4} and the ratio of concentration of the ions. Calculated from table 3.5.

The ratio of the triiodide concentrations at the two electrodes at V_{B3B4} = 2.3 mV is not big. This can be attributed to the small potential difference between the two electrodes. In this experiment, no coloration was observed between the two bottom electrodes as the disturbance happened to the system was very gentle. The coloration observed in another experiment was a T-induced effect. When V_{top} > -0.67 V is applied the coloration appears. This coloration is a clear indication of I_3^- or polyiodides accumulated near the two bottom electrodes creating a non-equilibrium state as shown in Figure 3.8. The coloration can be clearly seen by naked eye after disturbing the system for longer periods.

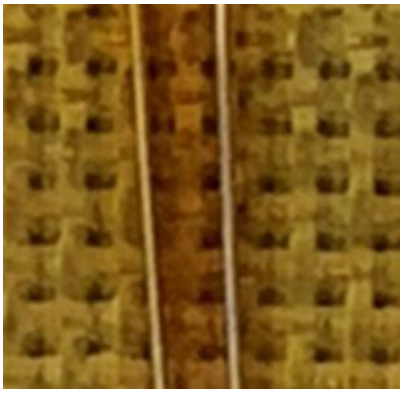

Figure 3.8 Coloration around the two bottom electrodes after applying a top voltage V_{top}=-0.87 V for one minute.

From table 3.5 the voltage between B3 and B4 decreases with time and the ratio between the ions concentration decreases over time as shown in Figure 3.7. That means the system will likely reach an equilibrium state after a specific time. Figure 3.9 shows the change of the voltage over time after the measurement. One can see that the ion concentration consistently explains the voltage effects. Therefore, it is very likely that the ion concentration at the electrodes has a major contribution on the resistance effects. This refers first to the secondary memory, but also to the primary memory. Therefore, also these investigations support the hypothesis that the part of the main memory effect comes directly from the electrodes. Based on that, the key to get higher ΔR_{BB} effects could be the modifying the measurement protocols or the electrodes itself

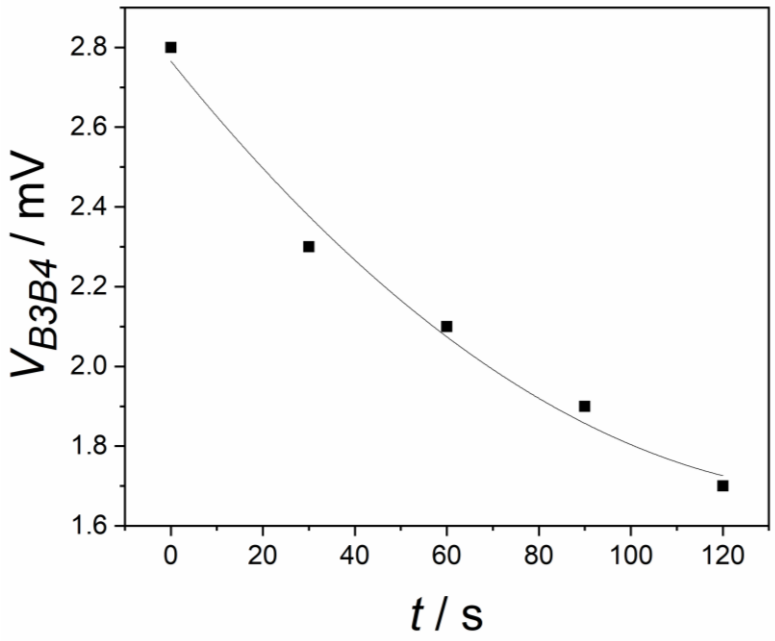

Figure 3.9 The change of voltage measurement over time

3.3 Measurements protocols

From the previous investigations, we concluded that a well defined protocol should be used to have reproducible results. To achieve this a modified configuration with new protocols especially suited for memory operation are used. The layout of the circuit includes a temporary short cut between the two bottom electrodes controlled by switch S3, a control voltage and a multimeter between the two bottom electrodes as shown in Figure 3.10A.

Two versions of a special protocol were used to investigate the memory characteristics of the device. Each of these two versions consists of three different phases: writing (**W**), storing (**S**) and reading (**R**). Each phase has a specific time to have reproducible and controllable results

after a series of such processes. The timeline of these phases is shown in Figure 3.10B. The first protocol is called **W-S-R** and uses cyclic **W-S-R** phases subjected to the IVEST. This protocol is used to measure the basic R_{BB} (resistance between the two bottom electrodes) readouts dependent on writing voltages (V_{top}) or the voltage applied on the top electrode. The second protocol is called **W-(S-R)**$_n$ and uses n repeated **S-R** phases to emulate repeated reading actions as in technical memories where the readings can be taken several times. It is used to investigate the memory contrast between HRS and LRS as well as their dynamics in section 2.7 specifically; we have used the times as visible in Table 3.7. To get a better control during the reading phase, a special electronic switch S2 was added to the circuit (for technical details see appendix F). A switch is an electrical component that can "make" or "break" an electrical circuit, interrupting the current or diverting it from one conductor to another. The switch we used is a special switch made of an electronic circuit that can set the reading time to 1.5 s in this work. We chose the reading time to be 1.5 s because it allows reproducible working with a multimeter and restricts the measurement effects of the multimeter. It can be tuned according to needs.

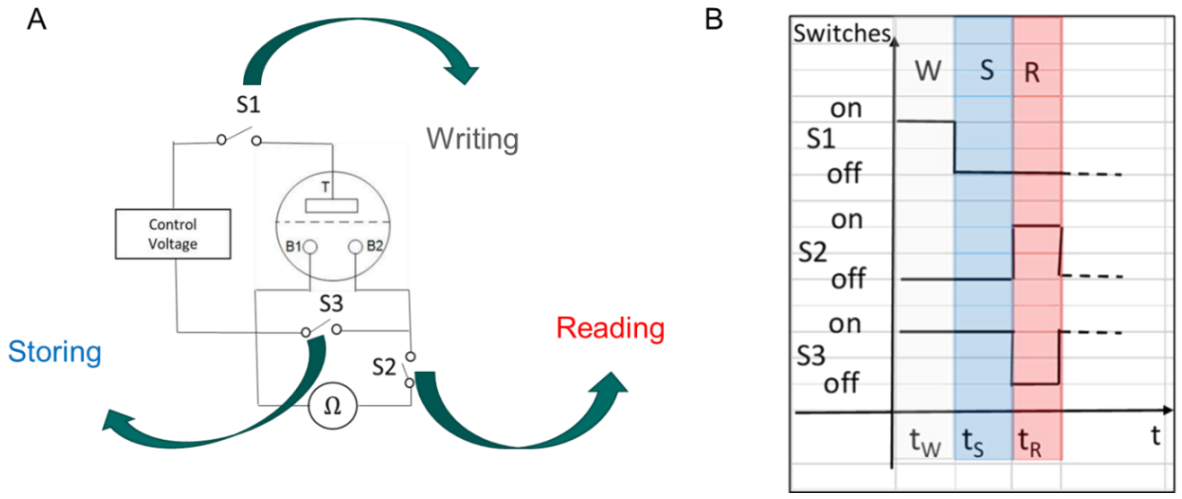

Figure 3.10 (A) Memory configuration with a temporary short circuit instead of the bypass used before. (B) Timeline of the **W-S-R** protocol [76]

Table 3.7. Different protocols used in this chapter. When necessary we add a number to indicate the duration of the specific phase in seconds.

Protocol	t_W / s	t_S / s	t_R / s
W-R	10	0	1.5
S-R	0	20	1.5

W-S-R	10	5	1.5
W-(S-R)$_n$	60	20	1.5

3.3.1 Readout changes

Concluding from the investigations in section 3.2, a shortcut between the bottom electrodes (storing phase) can help suppress the variable resistance resulted from making several measurements in a raw. The new configuration in Figure 3.10A was utilized, and a protocol (**R**1.5-**S**20) was applied. After each reading 1.5 s a storing phase was applied form 20 s. As shown in Figure 3.11, the resistance changes were successfully suppressed. Obviously the short cut between the two bottom electrodes can cancel the effects of the current injected by the multimeter at each measurement.

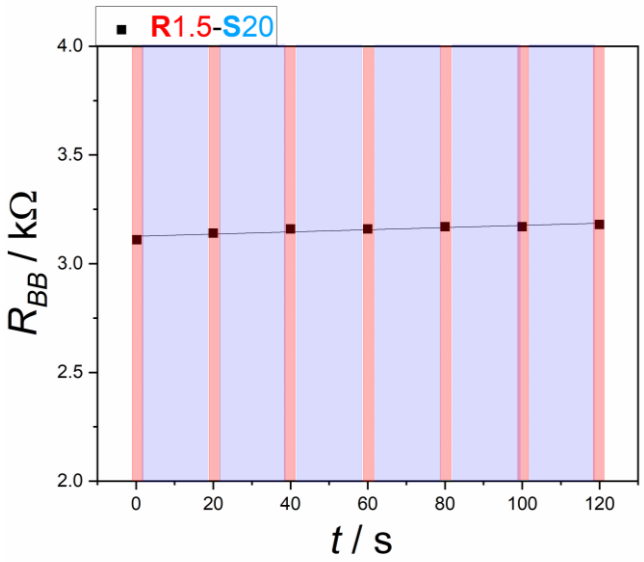

Figure 3.11 R_{BB} measurement with protocol **R**1.5-**S**20. A storing phase with 20 s was applied after each reading phase. [76]

3.3.2 W-S-R protocol

The protocol W-S-R consists of three phases. Each phase has a defined time as shown in Table 3.7. These phases also occur in many other memory operation processes. In Figure 3.12, we investigated the dependence on the writing voltage. This can be used to find out the range of efficient writing voltages and the conditions for storing information. As we can see in Figure 3.12, the device shows a pronounced hysteresis, i.e. the device can be in different states and remembers its history. Quantitatively, Figure 3.12 shows a hysteresis with a width of ΔR_{BB} = 1.06 kΩ (at V_{top} = -0.07 V).

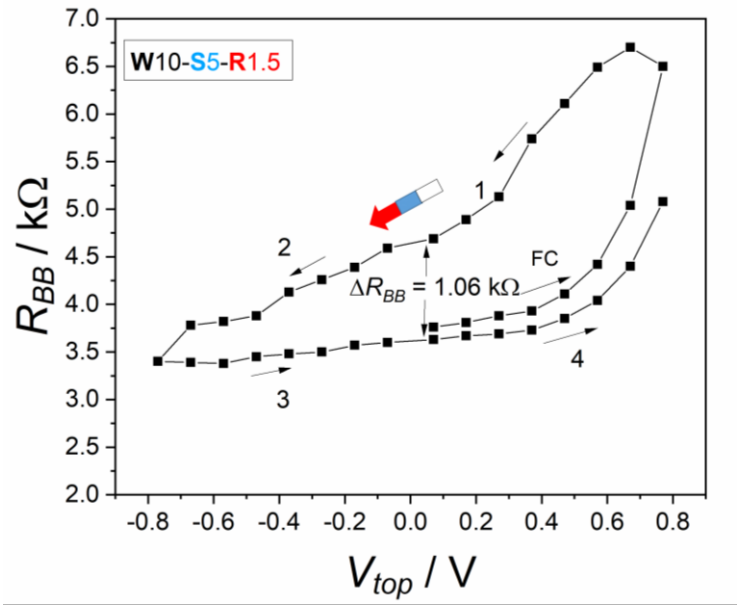

Figure 3.12 Writing-voltage dependence of R_{BB} using the **W**-**S**-**R** protocol. A voltage cycle indicated by the labels FC-1-2-3-4 was measured. The data points of the first application of voltage to the cell, we call formation curve (FC). The colorized arrow as well as the code **W**10-**S**5-**R**1.5 indicate the protocol applied in-between two data points. [76]

However, the interpretation of this result is not completely straightforward. For sure, there is an action of the top-voltage being the desired or primary memory effect. In addition, one must however expect an action of the read-out process. In detail, when the electrolyte is injected in the device, an electric double layer is created around each electrode. [87] To measure the resistance the multimeter injects a current inside the system that cause changes in these double layers or its surroundings. In our protocol, the used multimeter (IDM93N, RS PRO GmbH) injects a charge of 15 µC. Most importantly, the injected charge likely creates a partial depletion of ions at the involved electrodes. As a result, during the next R_{BB} measurement in this measurement cycle, the system is not the same any more. There is a small disturbance and especially an ionic depletion in the system. The concentration of the ions around each electrode is not symmetric anymore.

With each measurement there is an accumulation of such effects (secondary memory) occurs and this affects the main memory process, which we are trying to measure. In protocol **W**-**S**-**R**, the applied short cut between the two bottom electrodes was introduced to suppress this secondary memory. In comparison with chapter 2 results (Figure 2.25), we conclude that mainly the suppression of the secondary memory made the hysteresis visible and big as shown in Figure 3.12. In [56] and chapter 2, a bridge of two additional 2 kΩ resistors was used between the two

bottom electrodes to have the symmetry between them. However, these resistors decreased the memory effect significantly. In addition, the used measurement protocol was not well suited for memory operation. When the resistors were replaced with the short cut and a special memory protocol was applied, the memory effect became more visible during the R_{BB} readout measurement.

3.3.3 Effect of varying the storing time

As discussed in previous sections, each phase of the protocol **W**-**R**-**S** has a defined selectable time. During each phase, the system undergoes distinct processes. In the writing phase, a voltage is applied, leading to a change in the system's state. In the storing phase, it is desirable for the system to undergo minimal changes. However, if any changes occur, gradients will partially equilibrate, thereby suppressing potential secondary memory effects. Finally, in the reading phase the resistance between the two bottom electrodes is measured. Figure 3.13 shows the effect of varying the storing time.

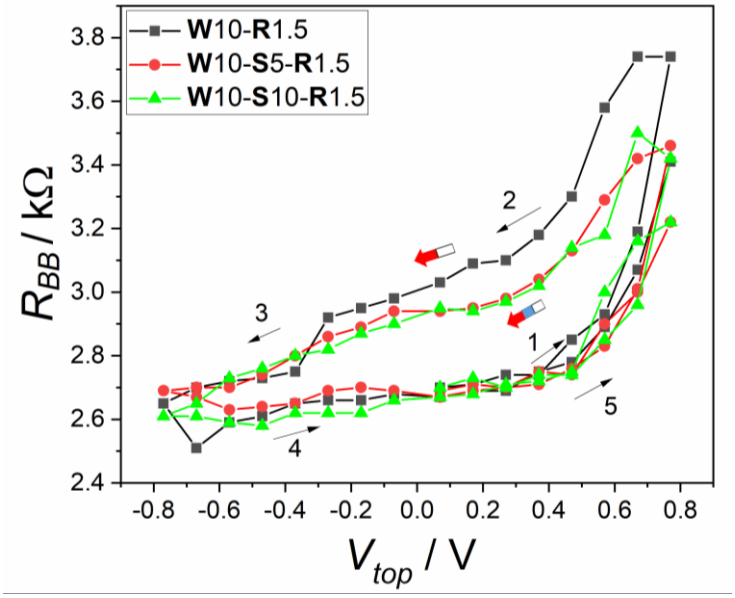

Figure 3.13 Effect of the storing phase (**S**) on the hysteresis. The black curves shows the result of applying a no storing time (indicated by **S**0 in the protocol code), the red curve and the green curve is a result of applying the storing time 5 s and 10 s, respectively. In the three curves, the writing time was fixed 10 s and the reading time at 1.5 s. The used writing-voltage cycle is indicated by 1-2-3-4-5. The colorized arrow as well as the inset codes indicate the protocol applied in-between two interconnected data points.[76]

The black curve in Figure 3.13 was measured by using the protocol **W**-**R** (see Table 3.7) where no storing time was applied after the writing phase. When the storing time was added to the protocol, the hysteresis decreased a little bit (by 0.05 kΩ) as the red and green curves show.

The hysteresis width remains almost unchanged when the storing time is increased from 5 to 10 seconds, as shown in Figure 3.13. This indicates that the signal can be stored in the device with minimal dependence on the storing time.

3.3.4 W(S-R)$_n$ protocol and memory contrast

The memory effect can be characterized with the memory contrast, which is the ratio between (HRS) and (LRS). As shown in the following equation mentioned before in chapter 2 (Eqn.2.9)

$$\alpha = \frac{H}{L} = \frac{R_{BB}^{H}}{R_{BB}^{L}}$$

In chapter 2 the investigation of the memory contrast of the device was found to be 1.3 with ΔR_{BB} = 0.56 kΩ [56], i.e., the resulted memory contrast was not big. To improve the memory contrast of the device the new protocol **W**-(**S**-**R**)$_n$ is used together with the configuration shown in Figure 3.10A. To make this measurement a positive writing V_{top}= 0.78 V was applied on the top electrode for a duration of 60 seconds. The outcome of this measurement is depicted in Figure 3.14. Notably, this adjustment resulted in an enhanced memory contrast, with a value of α = 1.8. Displaying a significant disparity HRS and LRS of ΔR_{BB} = 1.56 kΩ. Although minor changes were observed in both the HRS and LRS, these temporal variations were of negligible magnitude and did not compromise the memory characteristics of the device.

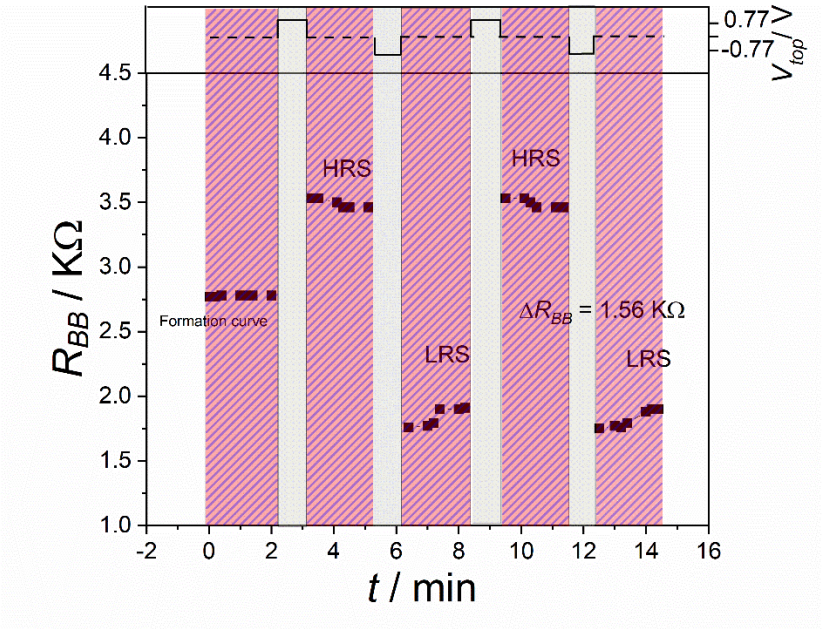

Figure 3.14 A switching measurement with the protocol **W**60-(**S**10-**R**1.5)$_n$. This means that a voltage is applied on the top electrode for 1 min then a storing time for 20 s is applied after that every reading was taken. [76]

3.4 Mechanistic aspects

In the IVESTs, it is expected that various simultaneous processes occur, with their relative importance depending on the operation protocol. These processes include voltage-induced effects and faradaic processes resulting from the flow of current. The voltage-induced effects have been qualitatively discussed in chapter 2 and reference [56]. However, for the writing phase in a memory device, and considering the protocols used in this chapter, the current flow is likely to be of greater importance. During a 1-minute writing phase, approximately 6 mA of the measurement current are transported, as shown in Figure 2.20. This charge flow induces a local change in the number of triiodide ions by 0.03 micromoles (µmol). Assuming that this change remains in the vicinity of the electrodes (within <0.5 mm), concentration changes of 0.9 millimolar (mM) for the top part and 25 mM for the B-part can be expected. As shown in Figure 3.8, such concentration changes have indeed been observed. Here the triiodide accumulated near to the two bottom electrodes is indicated by the coloration after applying a V_{top} = -0.87 V.

The effects on the top-electrode are much less to be observed because of its bigger size resulting in lower local concentration changes. In addition, we remark that the depletion of ions will likely have a bigger effect on the conductivity than accumulation. However, depletion of ions is more difficult to be observed with bare eye. Another aspect of ion transport becomes visible during the readout process. As we have already discussed above, another memory process that we call the secondary memory can be explained by the redistribution of the ions between the two bottom electrodes. When a series of resistance measurements is applied between the two bottom electrodes, each readout gives a little different value. Each value depends on the history of the number of previous readouts. This secondary memory can be interesting as a secondary information storage depending on the readout frequency.

Our focus in this chapter was primarily on the main memory that arises from a non-equilibrium state and the movement of ions within different parts of the device. We achieved suppression of the secondary memory by implementing a specific operation protocol, which involved creating a shortcut between the two bottom electrodes during the writing phase and introducing a storing phase. By suppressing this secondary memory, we observed improved stability, reproducibility, and controllability in the device's performance.

3.5 Conclusion

A specific operation protocol, consisting of writing, storing, and reading phases, has been reported in this chapter. A corresponding new external circuit configuration, with the addition

of a temporal shortcut between the two bottom electrodes, has been used. The **W**-**S**-**R** protocol resulted in a pronounced R_{BB} hysteresis. The memory effect was improved and demonstrated by using the **W**-(**S**-**R**)$_n$ protocol. The memory contrast increased to α = 1.8 with ΔR_{BB} = 1.56 kΩ. The observed processes in the device lead us to the conclusion that, the device has more than one memory process. The applied short cut between the two bottom electrodes managed to suppress the secondary memory to a large extend. The memory inside the IVEST mechanism is mainly controlled by the redox oxidizer depletion, non-equilibrium states of ion concentrations, and the redistribution of the ions between the different electrodes. The suppressing of the additional memories allowed the increase of the main memory effect. Based on these results, it can be concluded that the IVEST holds great potential as both a memory and a building block for neuromorphic applications.

The wide range of chemical tuning options available for the device means that there are numerous opportunities for further enhancements and improvements. Moreover, the construction and characteristics of the device make it a promising candidate for eco-friendly printing, then it can be a sustainable building block for neuromorphic or novel computing systems.

4. Opto-ionic voltage effect soft triode

The content of this chapter was submitted as "Opto-ionic voltage effect soft triode: An optical-to-ionic signal converter" Mohamed, E., & Marlow, F. (2024) to Advanced Materials Technologies. The main part of the text, as well as the figures of the following section, are reprinted and reproduced.

4.1 Introduction

Optoionics is a parallel field to optoelectronics. The word optoionic itself was used sometimes in the past to describe the solar cells or optoionic smart windows[96]. However, the term was not used many times in general until the past few years when iontronics started to gain more attention. Recently the term optoionic is used to describe both the ability of tuning the ionic conductivity using light or converting light signals into a change in the ions concentration or diffusion etc. [97-100] When this change is readable and detectable it is called ionic signals [101-103]. Being able to mimic optoionic transduction mechanisms found in various living organisms, such as plants, microbes, and certain animals, which sense light not only with their retina but also via photosensitive skin or exoskeletons, could lead to new applications like wearable devices [102, 104].

Biological nervous systems learns by sensory systems. An example is the optical nerve connected to the eye. The eye senses the light, and then, send the signal to synapses where the image is recognized and memorized. Our nervous system comprises approximately 100 billion interconnected neurons, which possess the remarkable ability to perform complex computations. Each neuron consists of cell body (soma), axons and dendrites as shown in Figure 4.1A. [105] Synapses are the interconnections between the axon end of the pervious neuron and the dendrites of the next neuron as shown in Figure 4.1B. [106] The term 'weight of synapse' is used in neuroscience and computer science to describe the connection strength between the neurons. This connection can be strengthened or weakened depending on the number of signals transferred through the synapse. [107] Synaptic plasticity refers to the capability of a synapse to modify its weight in response to an external stimulus[108, 109]. Synaptic plasticity is the root for human learning and memorizing [110].

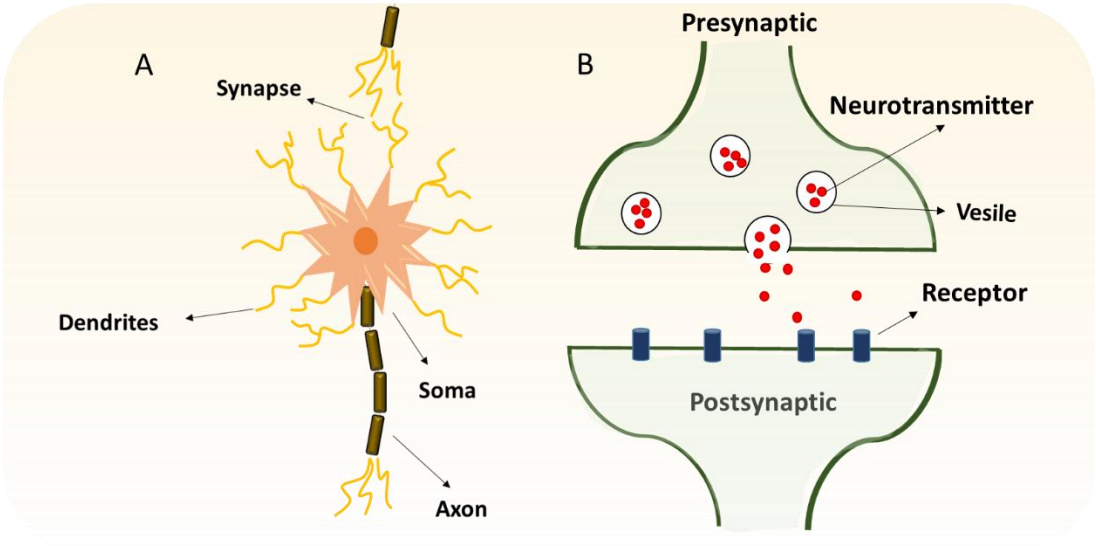

Figure 4.1 (A) Schematic description of a neuron which consists of cell body (soma), dendrites (input) and axon (output) (B) Schematic description of a biological synapse, consisting of a presynaptic terminal, and a postsynaptic terminal. Signals are transmitted from the presynaptic terminal to the postsynaptic terminal via the neurotransmitter

The progress in making optoelectronic synapses for artificial visual systems is increasing[111, 112]. However, building of a purely optoionic synapse device is not heavily studied yet, despite the fact that a purely ionic device would have similar working principles as the biological visual system [113]. In literature, optical signals were used in light gated memresitive devices as input and the resistance states as the output [114]. This can lead to a memlogic device where the signal can be saved and in the same time the device works as a logic gate which could be useful for eliminating the von Neumann bottleneck [114]. Using light as an input can be an advantage by getting rid of the required wires to power or control the devices.

The construction of the IVEST allows different chemical and mechanical tuning possibilities. With the materials used to build the electrodes and the used type of electrolyte, the incorporation of a photosensitizer seemed to be an interesting step. This modification made the device sensitive to light. Not only does IVEST detect light signals, but it also has shown potential to memorize UV illumination. In this chapter, the IVEST as an opto device will be tested. Finally, a theoretical explanation to understand the mechanism inside the device is provided.

As a device with a memory resistor, the IVEST could be used for new computational systems. Moreover, the IVEST has the ability to be in more than two states and each state is dependent on the history of the device unless a kind of reset is applied. Adding a photosensitizer to the

IVEST converts it from ionic device to an optoionic device. An opto-IVEST could give the possibility of operating different devices with only one input (illumination).

This chapter explores the conversion of the IVEST from an ionic device to an opto-ionic device. The study investigates the impact of incorporating a dye into the device's construction. An investigation is conducted to evaluate the performance of the IVEST in relation with the dye.

4.2 Device construction

The construction of the opto-IVEST is the same as the IVEST with a dye attached to the top electrode. All the used parts and solution as the same as mentioned in section 2.3.2 The top electrode was modified by dip coating in a dye after the calcination.

Dye preparation

A 0.026 g of the dye N719 (Di- tetrabutylammonium-cis bis(isothiocyanato)bis(2,2′-bipyridyl-4,4′-dicarboxylato)ruthenium(II), ≥ 90 % HPLC, 95 % NMR) was added to 50 ml pure ethanol to get a 0.5 M dye solution. The solution was stirred until it was homogenous.[21] To attach the dye molecules to the top electrode, the electrode was dip coated for 30 min in the dye solution then dried with a nitrogen stream.

Fabrication process

Figure 4.2 shows a schematic description of the opto-IVEST representing the dye molecules attached to the TiO_2 on the top electrode. To build the opto-IVEST fabrication method B mentioned in section 2.3.2 was used with the including of dyed top electrode.

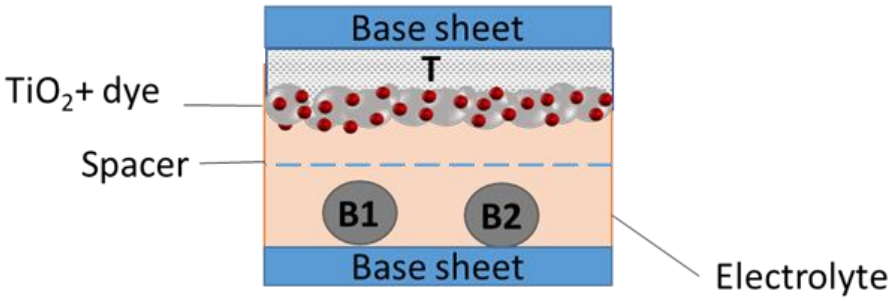

Figure 4.2 Schematic description of the opt-IVEST.

4.3 Measurements: setup and strategy

To characterize the device a special setup and holder were used as shown in Figure 4.3. The holder is especially designed to fit the size of the IVEST (Figure 4.3B). This holder allows the device to have a fixed distance between the illumination source and the device. It allows the device also to fit inside the chamber of the illumination setup as shown in Figure 4.3B.

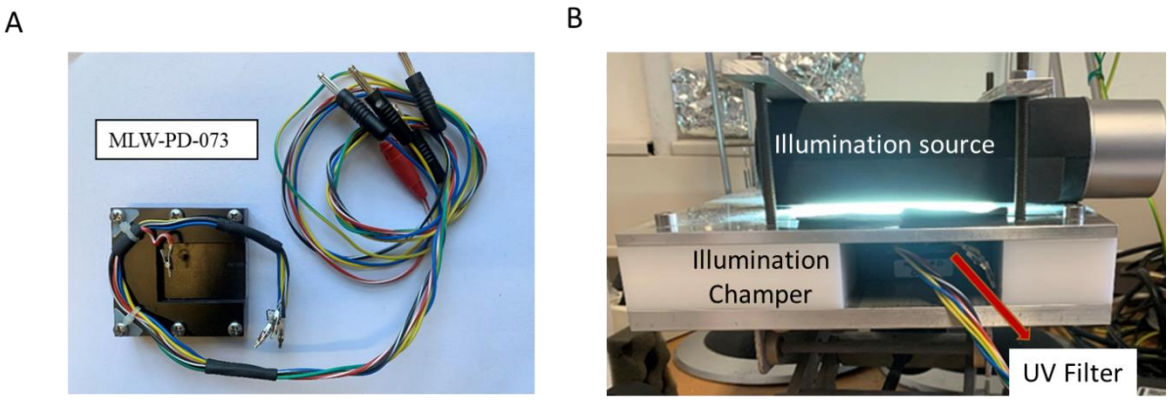

Figure 4.3 (A) Holder used for the opto-IVEST. (B) Illumination setup [74]

The illumination setup consists of a lamp Osram Dulux lamp 20 W/286, and a metal chamber to insert the device in under the lamp. The lamp is fixed on a specific height. A UV filter is used in all the measurement containing light as an input. The UV filter is always fixed on the top of the device before inserting in the illumination chamber.

To characterize the opto-IVEST, nearly the same configuration as in section 3.3 is used. A removable control voltage is connected to the top electrode through a switch (S1). A multimeter (IDM93N, RS PRO GmbH) is connected between the bottom electrodes using a special switch (S2) which allows a restricted time for the reading phase (1.5 s). The two bottom electrodes are connected together through a third switch S3. To this configuration, an illumination source and a shutter are used to control the illumination period as shown in Figure 4.4A.

Chapter 3 and [76] showed that a well-defined measurement protocol is essential for the IVEST characterization. The measurement protocols consists of three phases as mentioned before in the previous chapter: writing (**W**), storing (**S**), and reading (**R**). Each phase has a specific duration to have reproducible and controllable results after a series of such processes. In the writing phase (**W**) an electrical signal is applied to the T electrode of the device controlled by switch S1. In the storing phase, the status of the device is intentionally stored and mainly characterized by a closed short-cut switch S3. In the reading phase (**R**), the output signal is

measured and controlled by a time-programmable switch S2. Light is used as input either during the **S** or the **R** phase. This is indicated by the acronyms **SL** or **RL** as shown in Figure 4.4B and Table 4.1.

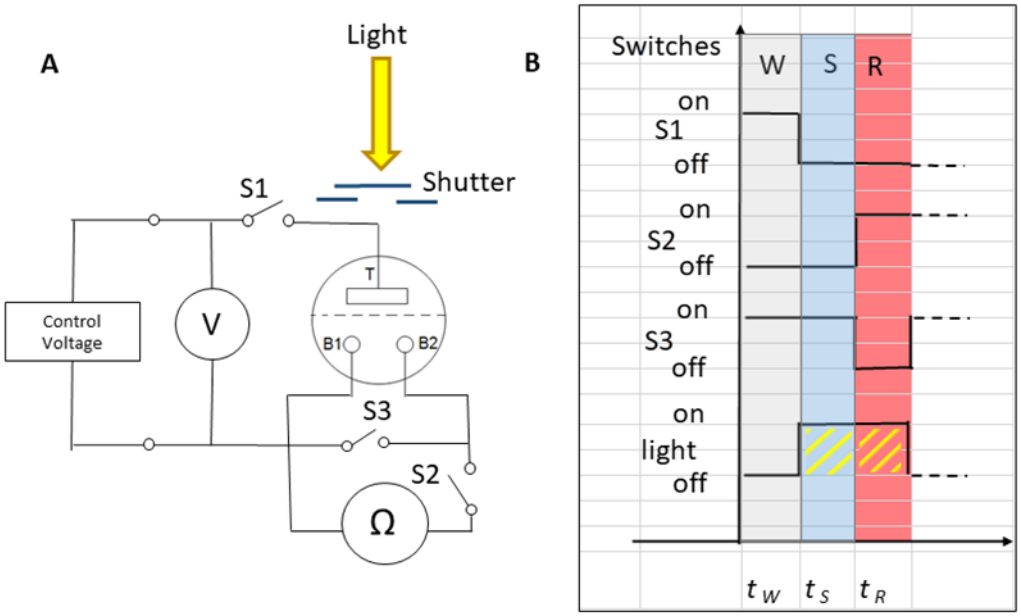

Figure 4.4 (A) Configuration used to characterize the opto-IVEST (B) Timeline of the different protocol parts, which can be assembled in various manner.

Table 4.1: The different phases of the measurement protocols. The colors are used in the following figures as well.

	S1	S2	S3	Light
W	close	open	close	off
R	open	close	open	off
RL	open	close	open	On
SL	open	open	close	On
S	open	open	close	off

There are many possibilities to use the illumination to effect the opto-IVEST. The illumination can be used as the only input or it can be used as a second input with electrical signals. It can also be used during each phase storing, reading and writing or during all phases. In the following sections, some of these possibilities were investigated.

4.4 Illumination as the only input

4.4.1 Effect of illumination during readout and storing phases

To investigate the behavior of the device in dark and during illumination the resistances between the two bottom electrodes in both cases were measured. The resistance was measured first in the dark and then after illumination. Here it is important to mention that no electrical signal was used at the top electrode (S1 open); light was used as the only input. First, the resistance between the two bottom electrodes in dark was measured using protocol (**R**1.5-**S**20)$_n$ with typical cycle numbers n = 7 … 20. The resistance R_{BB} was measured between the two bottom electrodes, then, a storing phase was applied for 20 s. This protocol was repeated over 120 s as shown in Figure 4.5. To test the effect of illumination on R_{BB}, the illumination was applied during the reading phase using the (**RL**1.5-**S**20)$_n$ protocol. Figure 4.5 shows that illumination during readout increases the conductivity between the two bottom electrodes. The resulting effect is not that big however, but detectable. This low effect can be assigned to be a result of the short illumination time during the reading phase, which is only 1.5 s.

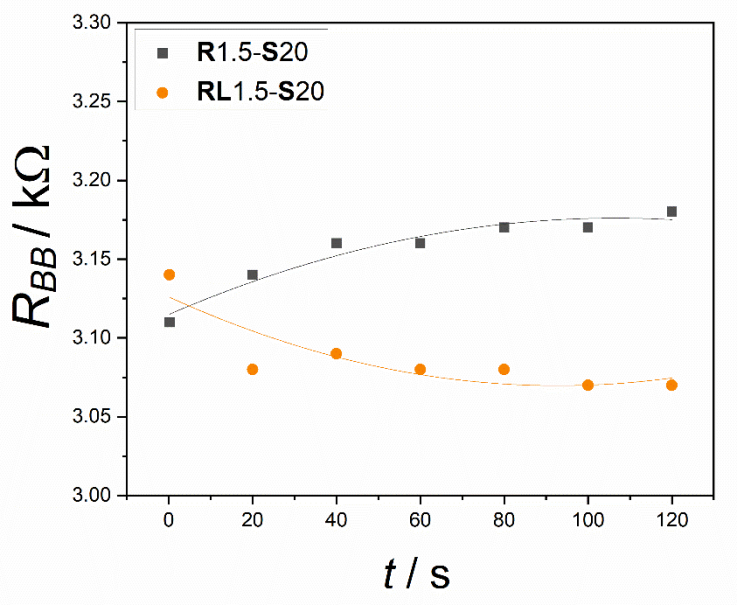

Figure 4.5 Effect of illumination during the readout phase. (Membrane with 1.2 µm pores, X_e = 0.39)

When we take look onto this result, we may see learning behavior according to a Hebb-like rule. The readout in the dark increases with each reading gradually, i.e. the high resistance state experiences a potentiation (as e.g. in [115]). When the light is applied during the readout, the resulting R_{BB} is decreased (i.e. depressed) with each reading. This is a kind of tunable learning,[116] but it needs to be ascribed to a nonassociative category. Nonassociative learning

can be based on one of the two cell activities, presynaptic or postsynaptic (see e.g.[117]) Therefore, a nonassociative postsynaptic learning rule can be actualized by the measured behavior.

As the period of readout phase is fixed to 1.5 s the illumination period in this case is very short. To have a better effect, the illumination during both the reading and the storing phases was tested as shown in Figure 4.6. First, the resistance between the two bottom electrodes in dark was measured using protocol (**R**1.5-**S**10). Then the illumination was applied during the reading phase and the storing phase using protocol (**RL**1.5-**SL**10). In this protocol and from the previous measurements we can say the illumination during the readout phase is nearly negligible. Clearly, ΔR_{BB} increased up to 0.57 k**Ω**. To see if the device can memorize the light signal after detecting it the resistance between the two bottom electrodes was measured in dark afterwards. As shown in Figure 4.6A, the resistance after switching off the light increased with time until it reached a specific value and then it became more stable. Likely, a number of ions are bounded to the semiconductor material at the T-electrode. They are stabilized there, because the electrode is in what we called low input current range (LIC) where the resistance is very high as shown in chapter 2 and ref. [56] In this case, those ions are effectively bounded to an insulator-like material and that makes it difficult to redistribute charges.

This is a clear indication that the device can detect and remember the light signal. After nearly 2.5 min of switching off the light the device can still have ΔR_{BB} =0.38 k**Ω**. The device after switching off the light can retain 66.6% of the initial optical signal.

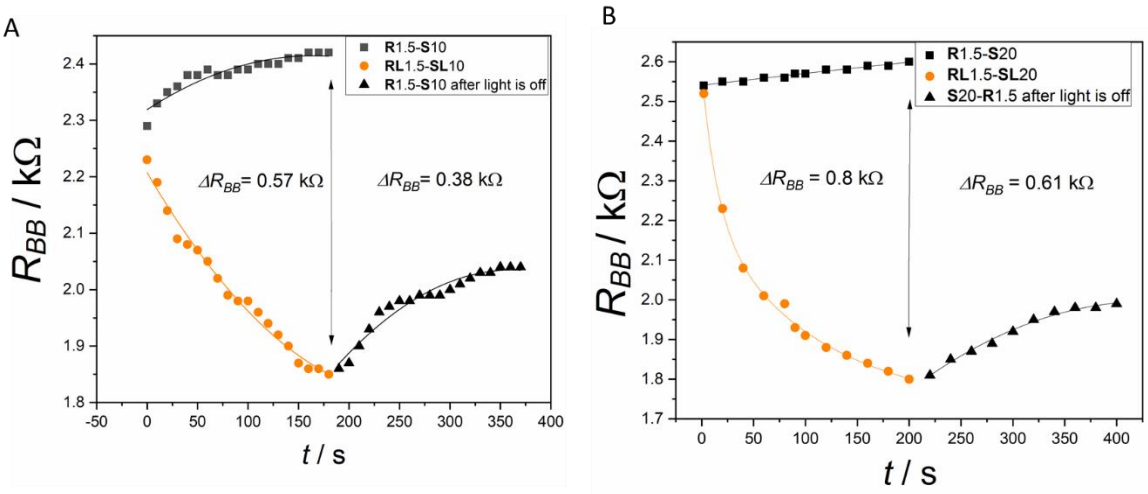

Figure 4.6 (A) Effect of illumination during the readout and storing phases phase on an IVEST with (membrane 1.2 µm, *Xe*=0.39) and (B) Effect of illumination on an IVEST without membrane (*Xe*=0.4, spacer pores 500 µm)

In chapter 2 [56] we realized that construction of the device including a small pore size membrane could give better memory effects. However adding the dye to the IVEST can make a change in the mechanism of the device. If the mechanism inside the device with illumination depends on the adsorption of the ions on the top electrode, then having cell with no membrane should increase the effects. Therefore, we investigated the effect of the membrane pore size on the performance of the device. As shown in Figure 4.6B ΔR_{BB} increased up to 0.8 kΩ, i.e. the optical signal after switching off the light was maintained to 70%, which is higher than with the membrane separator. This quantitative increase is, therefore, very likely a result of using the open separator allowing a better exchange between T and B part of the cell. This clearly points to a mechanism connected with the membrane (the more penetrable the membrane, the higher the effect), which means that the effect is connected to interaction between the T and B parts of the device. These results can be used to understand the mechanism inside the device in section 4.7. This behavior also reminds of the synaptic weight and synaptic plasticity. As each light signal can make a change in the resistance either increasing or decreasing, this reminds of the of the synaptic plasticity that strengthened or weakened depending on its activity .[46]

4.5 Seeking for an efficient RESET

From chapter 3 we have seen that the IVEST has more than one memory process. Each measurement depends on the history of the device and the previous measurements. As a result, a reset process is necessary between each set of measurements. In some cases, the reset is likely not important if the device would be used in applications like a perceptron or synaptic behavior. In other applications like the switching, a reset is essential. A reset here means to put the device again into its initial state after a specific disturbance. To reset the opto-IVEST two reset methods can be used which we call soft reset or hard reset. In the soft reset a short cut between the two bottom electrodes is applied. In the hard reset, a writing voltage will be applied on the device.

To test the possible methods for reset, a *JV* analyzer was used as shown in the configuration in Figure 4.7. In soft reset a short cut between the two bottom electrodes is applied for a specific time with no control voltage (S1 is open).

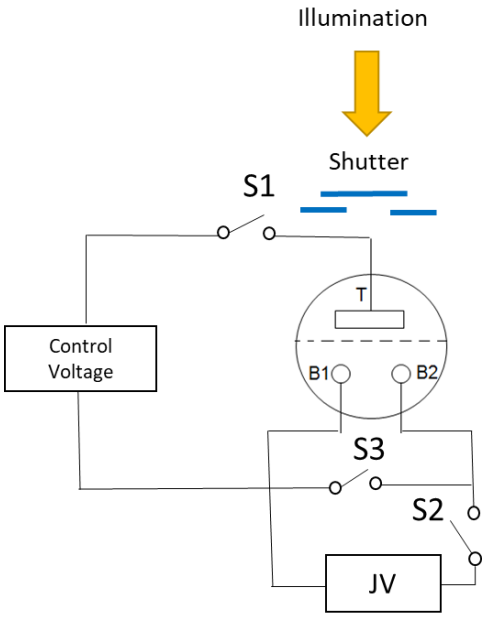

Figure 4.7 configuration used to test the reset with the *JV* analyzer

To test the effect of the soft reset a disturbance was made first by doing two measurement using the *JV* analyzer. First, a measurement was made in dark. Then illumination was applied for 300 s with protocol **SL**300 then a (JV_+, JV_-) measurement between the two bottom electrode in both positive and negative direction. A short cut afterword was applied between the two bottom electrodes (**S**300) and again a *JV* measurement was applied (JV_+, JV_-). As shown in Figure 4.8A the soft reset or the short cut did not make a change and did not erase the history of the device.

Another reset possibility is to use a writing voltage that we called the hard reset. After applying illumination for 300 s (**SL**300), a positive voltage was applied (**W**10, V_{top} = 0.57 V) then the *JV* curve was measured. As shown in Figure 4.8B the resulted curve after applying a positive voltage is shifted downward and the resulted current decreased. When a negative voltage is applied as a reset nearly no change was noticed.

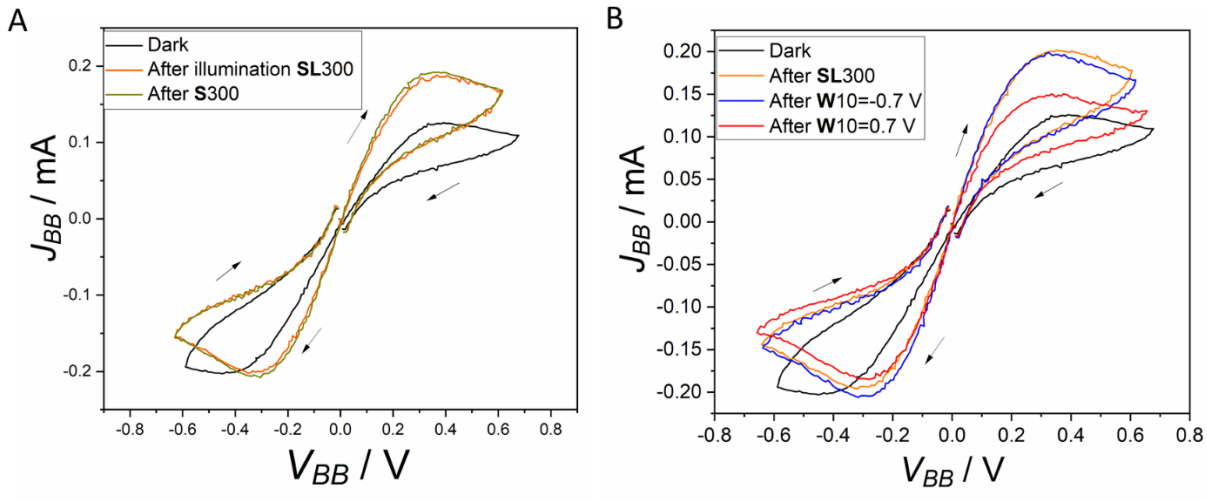

Figure 4.8 (A) Soft reset using short circuit. Protocol: (JV_+, JV_-) - **SL**300 - (JV_+, JV_-) - **S**300 - (JV_+, JV). (B) Hard reset using writing phase with V_{top}= -0.7 V for 10 s and then V_{top}= 0.7 V for 10 s, protocol: (JV_+, JV_-) - **SL**300 - (JV_+, JV_-) – **W**10(-) - (JV_+, JV_-) **SL**300- **W**10+ - (JV_+, JV_-)

It is interesting to note that the *JV* curves of the IVEST look like a memristor characteristics but with a non-pinched hysteresis. [51] This result opens a door for a possible future work to study the memristor like behavior of the IVEST.

4.6 Light as second input

4.6.1 Light gated IVEST: A hybrid logic gate

A mem-logic device or a memory logic device is a device that can make logic operation or work as a logic gate and as a memory at the same time. Mem-computing is a word used to describe systems that compute using a memory.[118]

To have a closer look at possible applications based on the opto-IVEST, a basic logic function that can be used to build a logical expression was tested. As we will show, the IVEST can be operated as a device that can perform a logical “AND” operation. For most logic gates, two variables are necessary as inputs to manipulate one output signal of a device that realizes a logic function. As shown in table 4.2 an AND gate function was tested. When the optical signal and electrical signals are applied, the resistance is in its lowest state. When the signals were applied for less than 15 s the change in R_{BB} was not big enough and a logical gate function was not very clear this is why a longer period of signal should be applied. When the electrical and optical signal time was increased to 15 s, the resulted effect was higher as shown in table 4.2. This can be interpreted as AND gate. We only need to make the assignments:

R_{BB} > 2.78 kΩ => **0** and R_{BB} < 2.36 kΩ => **1** (4.0)

Table 4.2 Truth values and electrical output resistance of an opto-IVEST. All the signals were applied for 15 s. The applied electrical signal = -0.6 V.

Opt.	Elec.	Output R_{BB} / kΩ	logical output (with 4.0)
0	**0**	2.78	0
0	**1**	2.74	0
1	**0**	2.73	0
1	**1**	2.36	1

4.6.2 Memory function with optical and electrical writing

When illumination is applied, the resistance between the two bottom electrodes decreases. This is like when a negative voltage is applied on the top electrode as shown in section 2.7. Illumination can then be used to achieve (LRS) instead of the negative voltage applied on the top electrode. Figure 4.9 represents a switching measurement using illumination (with **SL**) and positive voltage writing on the top electrode.

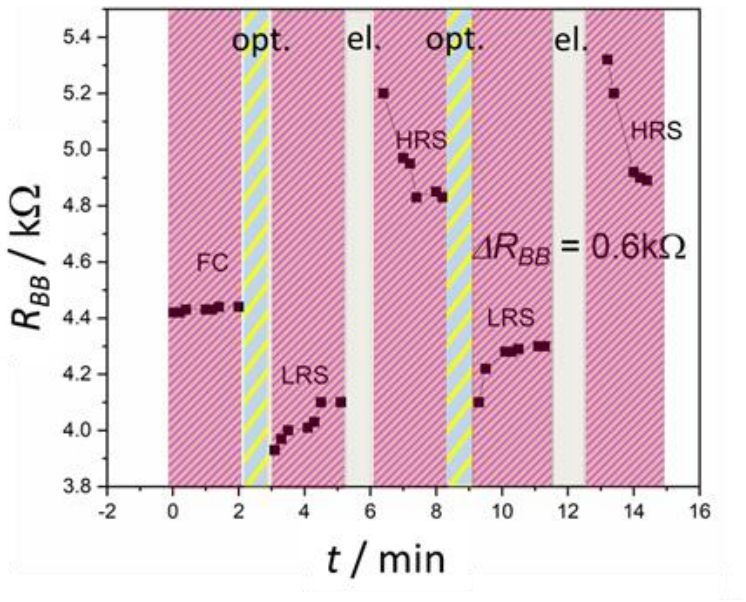

Figure 4.9 Switching between two memory states using electrical (white) and optical (yellow-blue) signals. Protocol: (**S**20-**R**1.5)$_n$-[**SL**60(S20-R1.5)$_n$-**W**$_{0.67V}$60(**S**20-**R**1.5)$_n$]$_2$. Color code according to table 4.1.

Experimentally, the resistance between the two bottom electrodes was measured using protocol (**S**20-**R**1.5) for 2 min (formation curve). Then, the device was illuminated for one minute

(**SL**60). The optical signal was turned off and the resistance was measured using protocol (**R**1.5-**S**20). As shown in Figure 4.9, this illumination resulted in LRS. Then, a positive voltage V_{top} = 0.67 V was applied for 1 min (**W**60) in the dark. Afterwards the resistance was measured using protocol (**R**1.5-**S**20). The writing resulted in a high resistance state with a significant difference from the low resistance state of ΔR_{BB} = 0.6 kΩ. Another possibility is to use both electrical and optical signals to a achieve more than two resistance state or to build a multi-logic device.

In Figure 4.10, when only a positive writing was used, the device was moved to the high resistance state. Then a negative voltage V_{top} = -0.6 V was applied for 1 min and a lower medium resistance state (M1RS) was the result. Again, when the positive writing was applied the device was moved to the higher resistance state. Combining the negative voltage and the illumination resulted in the lowest resistance state. Depending on this result, the device can exist in different states depending on the light or electrical signal applied.

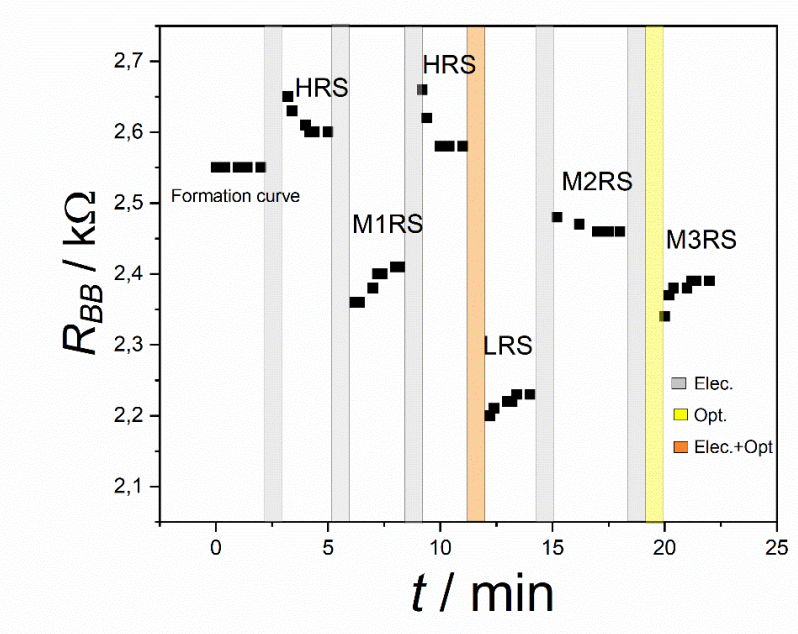

Figure 4.10 Switching between different resistances states using both optical and electrical signals.

4.6.3 Switching cycles

From section 4.6.2, we can state that the optical signal has the capability to switch the device to the low resistance state. The resistance between the two bottom electrodes experiences a decrease when exposed to illumination. Since light can only function in one direction, an electrical signal is required to achieve the high resistance state. In the case of the IVEST, a positive voltage is employed to switch the device to the high resistance state. Figure 4.11

visually demonstrates the device's ability to switch between the high resistance state and the low resistance state repeatedly. In Figure 4.11, the protocol used for each point was (**SL**10-**R**1.5) to reach the LRS, immediately followed by (**W**10-**R**1.5) with no reset. The voltage used during the writing phase was V_{top} = 0.66 V. The reproducibility and stability of the hybrid optical and electrical signal switching between two resistance states is proved by several switching cycles as shown in Figure 4.11.

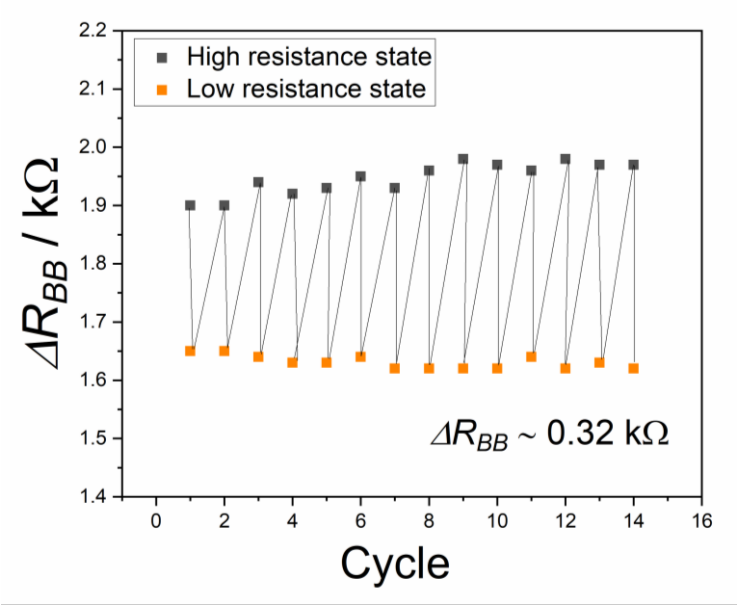

Figure 4.11 The high resistance state (HRS) and low resistance state (LRS) for 14 cycles. The switching between high resistance and low resistance for 14 cycles. Protocol: **S**20-**R**1.5-[**SL**60-S20-R1.5-$\mathbf{W}_{0.67V}$60-**S**20-**R**1.5]$_{14}$

4.7 Mechanism

When the semiconductor layer comes in contact with the electrolyte, a depletion zone with positive charge is created inside the semiconductor material as described in Fig. 2.29. The electrolyte tries to compensate this layer by accumulating ions with opposite charge at the interface of the semiconductor material and the electrolyte. This layer will contain also other ions with positive charge. [56]

There are different hypothesis that can be used to explain the mechanism of the opto-IVEST. The first hypotheses is that what happens during the illumination is a voltage effect depending on the adsorption of the ions on the top electrode. The second hypothesis is that is a current effect. When the top voltage reaches enough value due to illumination, circular current starts to flow between the three electrodes inside the device. To understand the mechanism inside the device and to prove one of these hypotheses, the top voltage, the voltage between the two

bottom electrodes and the resistance between the two bottom electrodes during illumination was measured. A special setup configuration was used to perform this experiment. Figure 4.12 shows the layout of the used configuration.

The used protocol to perform this complex measurement is as follows: **SL**20-**R**1.5-V_{BB}1.5-V_{Top}. First, the illumination is applied on the device with phase (**SL**20). The R_{BB} reading was taken by (**R**1.5). After measuring R_{BB}, the V_{BB} was measured. Finally, S3, S1 and S4 are closed to measure V_{Top} while S2 is opened. Then in dark, the same measurement was repeated using protocol: **S**20-**R**1.5-V_{BB}1.5-V_{Top}. The result of each physical quantity was combined in a separated graph in Figure 4.13 for easier visual representation.

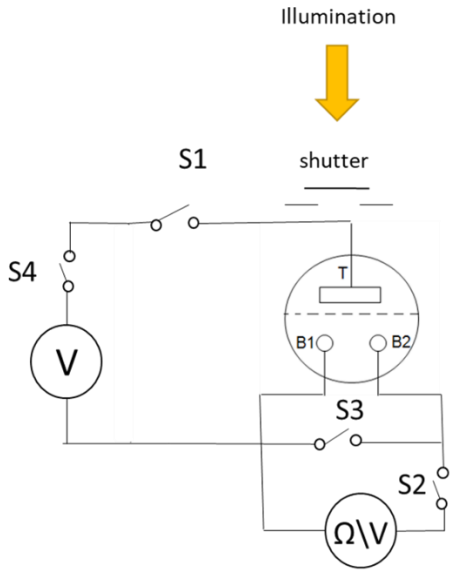

Figure 4.12 Configuration used to measure V_{Top}, V_{BB} and R_{BB}

Figure 4.13A shows that the top voltage increases with increasing the illumination period until it reaches the highest point when protocol **SL**20-**R**1.5 is used. Then it starts to decrease after the light is switched off and protocol **S**20-**R**1.5 is used. When the resistance was measured, the results shown in Figure 4.13B shows less ΔR_{BB} than the previous results, as the measurement contain many steps and longer periods. However, the results show the same behavior where the resistance decreases by increasing the illumination time. When we go further with the measurement and measure the voltage between the two bottom electrodes, we can see that there is a voltage difference between them as shown in Figure 4.13C

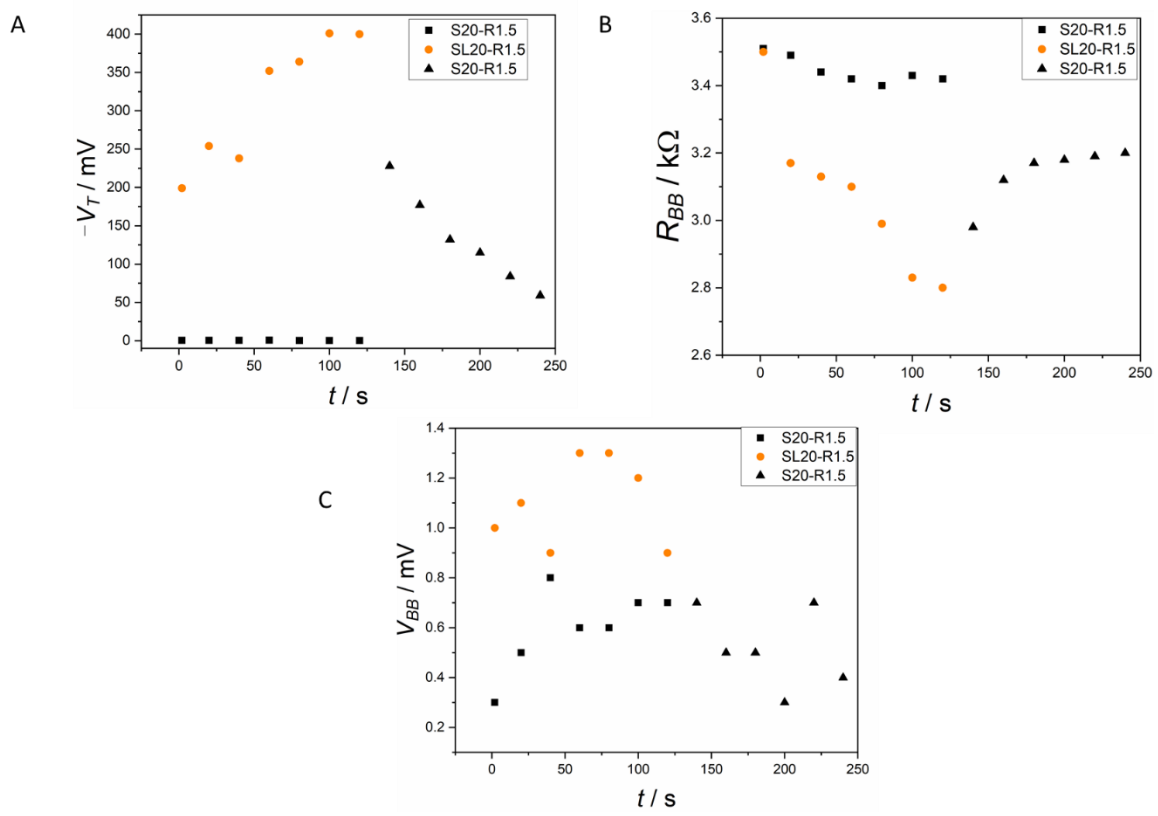

Figure 4.13 (A) Voltage on the top electrode (V_T) resulted from illumination. (B) Resistance between the two bottom electrodes in relation with different protocols in light and in dark (R_{BB}). (C) Voltage between the two bottom electrodes at different protocols (V_{BB}).

In general, when the device is illuminated, the dye get excited. The dye molecule will lose an electron inside the TiO_2 layer and this will change the width of the depletion layer inside the semiconductor. [22] As the width of the electronic depletion zone decreases, the thickness of the compensation layer at the interface between the electrode and the electrolyte will decrease as well. As a result, the conductivity between the two bottom electrodes will increase. We can say that the mechanism inside the device depends on the adsorption of the ions.

Considering the previous results, we can understand the mechanism inside the device as follows. When the semiconductor material is in contact with the electrolyte, an electronic depletion zone is created inside the TiO_2 layer. This zone is positively charged. To compensate and screen these charges, the electrolyte will accumulate ions near to the interface between the semiconductor material and the electrolyte. These ions are bound and cannot contribute to the conductivity between the two bottom electrodes.

To find a quantitative expression for these processes, we have a look at the variable number of electrons Q_e/e that are depleted, inducing the positive charge of the solid. This number is

reduced by the every illumination step. Its temporal change will have consequences on three properties: ion content of the ionic compensation layer, width of the electron depletion zone, and voltage at the T-electrode. Let us start with ion content of the ionic compensation layer which can be described by two equalities both shown in Eqn. 4.1. The total number N_E of additional iodine ions bound near to the electrode is

$$N_E = \gamma \cdot Q_e/e = n_d A w \gamma \quad (4.1)$$

where w is the width of the deplete zone, n_d is the electron density, A is the electrode area, γ is an amplification factor between the electrons compensated and the ions demobilized, and e is the elementary charge. Below it will be used that the conductivity change is controlled by N_E.

The excess ions bounded near to the electrode consists of at least two types of ions, iodide and triiodide. When there is an excess of negative ions on the interface between the electrode and the electrolyte, positive ions will also exist, creating a diffuse layer of ions. The size of this diffuse layer is much bigger than the adsorption layers which is also reflected in the γ factor. It considers that we have more consumed ions than electrons.

When the device is illuminated, the dye will get excited and it can transfer an electron to the semiconductor layer as in DSSCs [18, 22] (indicated in Figure 4.14). With the injected electrons, w will decrease. As the width w decreases, the thickness of the compensation layer at the interface between the electrode and the electrolyte will decrease as well. As a result, the conductivity between the two bottom electrodes will increase. The conductivity depending on the illumination was calculated from a measured R_{BB} as shown in Figure 4.14. At the same time, the top voltage will become more negative with increasing illumination time according to this mechanism. Theoretically, the conductivity changes according to

$$G_{BB} = G_0 - \alpha_2 Q_{e0} + \alpha_2 (J_L \cdot t_L) \quad (4.2)$$

as it can be found by assuming a linear relation between the ion concentrations and the conductivity. Here, α_2 is a constant, J_L is the electron current generated by illumination, and t_L is the illumination time. Such a curve is also included in Fig. 4.14.

In parallel, there is a change on V_T during illumination as shown in Figure 4.13A. According to the mechanism above, the transferred electrons will generate a negative voltage as indeed measured. The functional behavior can be predicted using an approximate description of w according to the Mott-Schottky theory. This leads to

$$V_T = V_{fb} + c1(Q_{e0} - J_L \cdot t_L)^2 \qquad (4.3)$$

With V_{fb} for the flat-band potential and a system-dependent constant $c1$. This description is justified for small V_T values only and breaks down when the flat-band potential is approached.

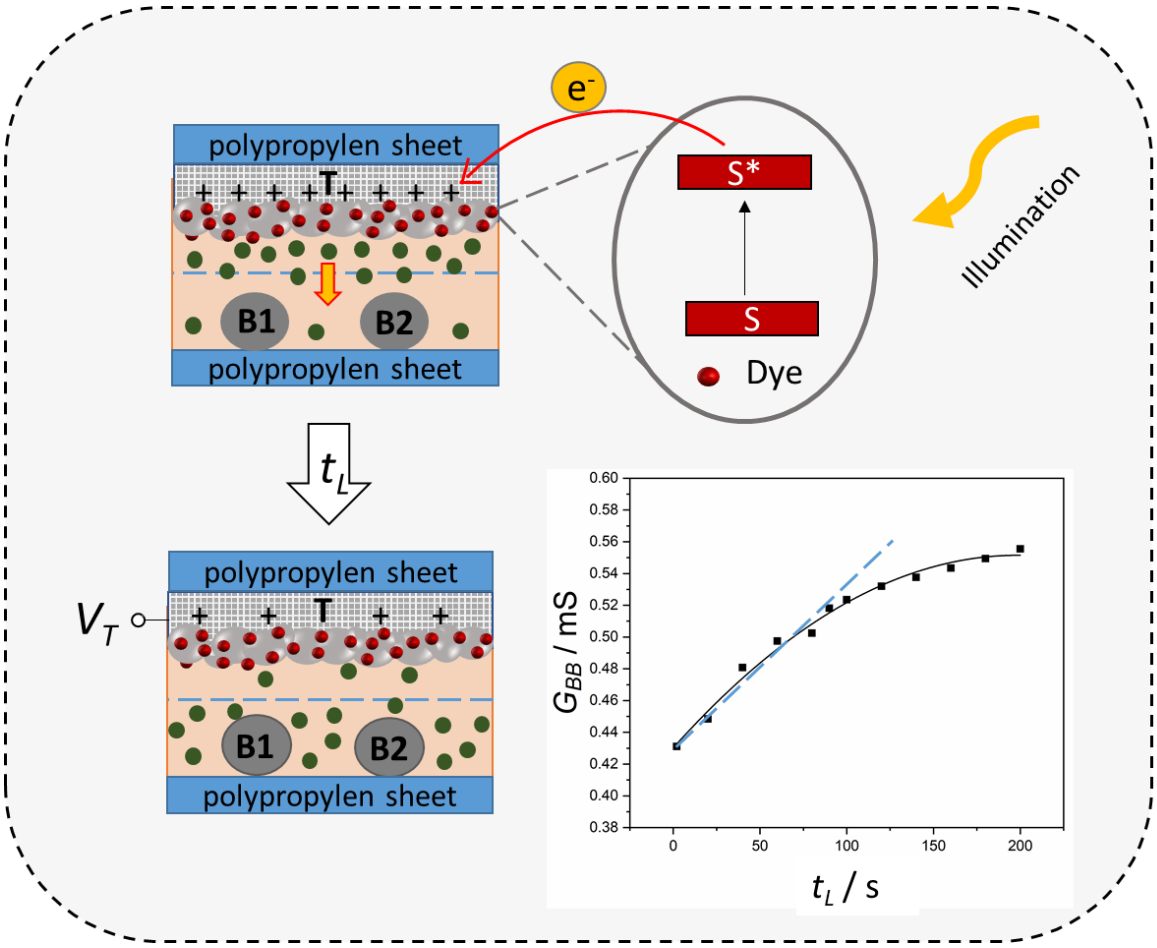

Figure 4.14 Schematic description of the mechanism inside the IVEST before and after illumination (A) Depletion zone inside the TiO_2 layer and the compensation of the electrolyte ions to this layer (B) After illumination charge is injected inside the depletion zone and with illumination the ionic layer on the interface between the TiO_2 layer and the electrolyte decreases (negative V_T).

Figure 4.14 shows a summary of the mechanism inside the opto-IVEST with illumination together with a measurement result, which is well described within the limits of the above approximate theoretical treatment.

4.8 Conclusion

A new optoionic device was built. The main mechanism inside the opto-IVEST at the studied operation protocols is an ionic enrichment near to a semiconductor surface. Illumination was

used as a single and as a complementary input. The device is able to recognize an optical signal and to memorize it and can works as an optical-to-ionic signal converter

The signal can be retained up to 70% of the initial optical signal. Beside this, the behavior can be interpreted as ability of learning expressed by potentiation and depression behavior. The behavior of the opto-IVEST reminds of synaptic plasticity where the conductivity between the two bottom electrodes is decreased or increased depending on the type and the number of signals applied on the device.

It is a purely ionic device working with similar principles as biological systems and it can detect and memorize the signal in the same unit.

The device also shows the possibility of using light as a complementary input with electrical signals. This can be useful as a switch or as a writing and erasing process. Moreover, the opto-IVEST showed AND behavior of a hybrid logic gate by using both electrical and optical signals as inputs. In general, the device also shows the potential to be used in different applications especially in neuromorphic systems.

5. Summary and Future Perspective

The main outcome of this thesis is the invention of a new purely iontronic device called ionic voltage effect soft triode (IVEST). It is an electrochemical cell that consists of three electrodes: a top electrode and two bottom electrodes. The IVEST has advantages over some of the known ionic devices since it is constructed without the need of expensive and sophisticated fabrication method.

In the first part of the thesis, the IVEST was fabricated with different fabrication methods. To characterize the IVEST three main characterization methods were used. The first characterization method is common B1 configuration. It was used to characterize the input and the output of the device. However, this method was difficult to interpret. The benefit of this method was it led us to the conclusion that the sc(m||m) structure is the best. To make the characterization method easier and more understandable another characterization configuration was used. This configuration is called symmetric BB configuration. In this configuration, two 2 kΩ resistor bridge was connected between the two bottom electrodes to assure the symmetry between them in circuits. The output current of the device was high in comparison to the input of the device. In addition, the device has an amplification behavior. This configuration allowed us to see clearly the relation between the voltage and the current of the device. The output of the device was behaving like a resistor. Based on this the last used characterization can be called resistance control characterization method. In this method, the resistance between the two bottom electrodes was measured by using a multimeter in the relation to the voltage change on the top electrode. By investigating the curves resulted from the previous characterization methods, it was found that the IVEST has both amplification and memory characteristics.

To tune the amplification the investigation focused on optimizing the semiconductor layer on the top electrode and diluting the electrolyte. Through this process, the amplification behavior was carefully fine-tuned. As a result, the amplification reached its peak performance, displaying improved signal amplification β = 52. The mechanism of the amplification is based on the adsorption of the ions on the top electrode. Achieving optimal amplification requires a careful equilibrium between enhancing the transconductance and maintaining a high resistance level.

The memory effect of the IVEST was investigated through two main measurements. These measurements included the switching measurement and the study of the stability time of the

device. In the switching measurement, the device was transitioned between a high resistance state and a low resistance state by applying either a positive or a negative voltage to the top electrode. The difference between these two states reached a value of ΔR_{BB} = 0.56 kΩ, with a memory contrast of α = 1.3. The effect of electrolyte dilution was also examined, and it was proven that the memory effect increases when the electrolyte is diluted. Additionally, the membrane within the device was found to play a significant role in the memory effect. By reducing the pore size of the membrane, the memory effect was observed to increase. This can be explained by the fact that the smaller pore size hindrance the diffusion of ions, thereby increasing the stability time of each state.

In the second part of the thesis, a pentode was constructed to understand the device's mechanism, which is an IVEST with four bottom electrodes instead of two. Upon measuring the resistance between each pair of electrodes in the pentode, we discovered that resistances were not equal. Furthermore, upon making multiple consecutive resistance measurements between two electrodes, variations in the readings was observed. To investigate this phenomenon, a rectangular R_{BB} matrix was used and the resistance between each pair of the bottom electrodes was measured. Subsequently, we tried to identify and control the factors that could potentially influence the resistance. Our investigation revealed the existence of four main factors that contribute to this change in resistance values: the number of connection changes (steps), read-out polarity, and memory effects. Furthermore, two factors contribute to variations between different electrode pairs: air bubbles and fabrication inaccuracies. Different matrix sequences were examined. During these investigations, it became apparent that the history of the device influences each measurement. When the measurement is taken, each electrode remembers this measurement. This can be interesting if we linked it to the synaptic behavior or the learning process. In case we want to suppress these memory effects on the bottom electrodes to have more controlling on the main memory between the two parts of the device we can use a short cut between the two bottom electrodes. These results led us to a new configuration for the device containing the short cut between the two bottom electrodes and the use of a specific switch that control the time of measurement to 1.5 s. Another study was conducted by measuring the voltage matrix instead of the resistance. Voltage measurement provides a disturbance-free assessment, and based on the results, we were able to determine the difference in ion concentration between the two bottom electrodes using Nernst's equation. After performing the calculations, we discovered that with five measurements, there was a 20 percent change in the ratio.

To improve the performance of the device a well-defined measurement protocol with a modified measurement layout was used. Two main measurement protocols was used (**W**-**S**-**R**) and **W**(**S**-**R**)$_{n.}$ Each phase of these protocols has a specific time. With the use of the new layout and the new measurement protocols the memory effect was increased to have a contrast of α = 1.8 and ΔR_{BB} = 1.56 kΩ.

In the third part of the thesis, as the IVEST allows different possibilities the IVEST was modified to be an optoionic device. As the top electrode is covered with mesoporous TiO_2 layer the device can be converted to an opto-IVEST by adding a dye to the top electrode. When the dye was added to the IVEST, it was able to detect the light signal. When the device was illuminated the resistance between the two bottom electrodes decreased. Illumination during the readout phase and the storing phase was tested. Besides detecting the light signal, the opto-IVEST showed the ability to memorize the signal after switching off the light. Each illumination was able to make a change on the resistance of the device. Based on this the light signal was used with an electrical signal to switch the device between a high resistance and low resistance states. The device also showed a possibility to be used as AND gate with both electrical and optical signal. The opto-IVEST showed an interesting learning behavior.

In general, the IVEST showed the possibility to be used in memory applications and opened the door for many possible future investigations. It can be used as a building block for neuromorphic information processing systems and could, therefore, be a step towards a new computational technology. In Figure 5.1, a tree is shown displaying some possible applications based on the IVEST. As shown the IVEST roots are iontronics, DSSCs and electrochemistry. With the amplification and memory characteristics, the IVEST can be used as a building block for new computing systems, artificial synapses, applications in optoionics and can be constructed with 3D printing. These possible applications is not all investigated yet, however, they can be interesting topics for future investigations.

Yet going down with the size of the IVEST was not investigated. Using inkjet printing or screen-printing can be possible to build the device in the micro scale. Embedding the device also in a circuit can lead to more understanding of the device. New electrolyte testing with other redox couples is a good direction for future investigations. A new electrolyte with higher viscosity can decrease the leakage and drying out of the current electrolyte. A new redox couple will help in more understanding of the mechanism inside the device. Another important characteristic of the IVEST is the memristor like behavior that needs further investigations.

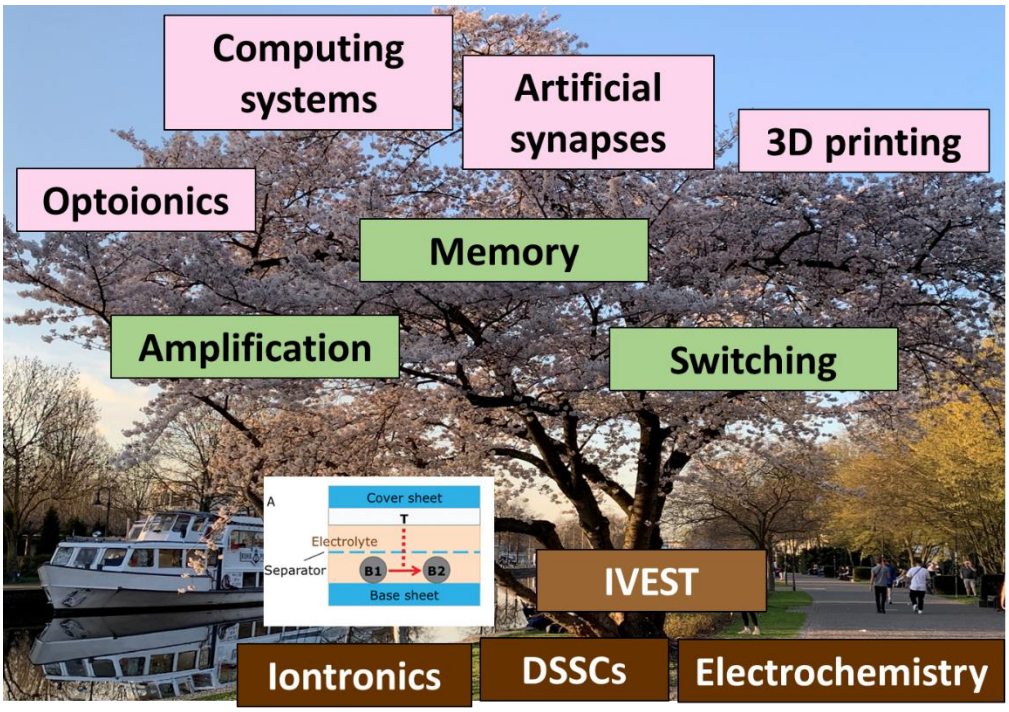

Figure 5.1 IVEST based tree. Possible applications based on the IVEST

6. References

[1] X. Guo, M. Baumgarten, K. Müllen, Designing π-conjugated polymers for organic electronics, Progress in Polymer Science, 38 (2013) 1832-1908.
[2] J. Leger, M. Berggren, S. Carter, Iontronics: Ionic carriers in organic electronic materials and devices, CRC Press, 2010.
[3] T. Arbring Sjöström, M. Berggren, E.O. Gabrielsson, P. Janson, D.J. Poxson, M. Seitanidou, D.T. Simon, A decade of iontronic delivery devices, Advanced Materials Technologies, 3 (2018) 1700360.
[4] T. Fujimotoa, K. Awaga, Electric-double-layer field-effect transistors with ionic liquids, Phys. Chem. Chem. Phys., 15 (2013) 8983-9006.
[5] S.-W. Nam, M.J. Rooks, K.-B. Kim, S.M. Rossnagel, Ionic field effect transistors with sub-10 nm multiple nanopores, Nano Letters, 9 (2009) 2044-2048.
[6] B. Xie, T. Xiong, W. Li, T. Gao, J. Zong, Y. Liu, P. Yu, Perspective on nanofluidic memristors: from mechanism to application, Chemistry–An Asian Journal, 17 (2022) e202200682.
[7] D.C. Gadsby, Ion channels versus ion pumps: the principal difference, in principle, Nature reviews Molecular cell biology, 10 (2009) 344-352.
[8] B. Glancy, R.S. Balaban, Role of mitochondrial Ca2+ in the regulation of cellular energetics, Biochemistry, 51 (2012) 2959-2973.
[9] A. Zhang, C.M. Lieber, Nano-bioelectronics, Chemical reviews, 116 (2016) 215-257.
[10] J. Zhang, W. Liu, J. Dai, K. Xiao, Nanoionics from biological to artificial systems: An alternative beyond nanoelectronics, Advanced Science, 9 (2022) 2200534.
[11] M.U. Khan, J. Kim, M.Y. Chougale, R.A. Shaukat, Q.M. Saqib, S.R. Patil, B. Mohammad, J. Bae, Advancement in Soft Iontronic Resistive Memory Devices and Their Application for Neuromorphic Computing, Advanced Intelligent Systems, 5 (2023) 2200281.
[12] S.Z. Bisri, S. Shimizu, M. Nakano, Y. Iwasa, Endeavor of Iontronics: From Fundamentals to Applications of Ion-Controlled Electronics, Adv. Mater., 29 (2017) 1607054-1607102.
[13] J. Yin, X. Li, J. Yu, Z. Zhang, J. Zhou, W. Guo, Generating electricity by moving a droplet of ionic liquid along graphene, Nature nanotechnology, 9 (2014) 378-383.
[14] X. Miao, S. Tongay, M.K. Petterson, K. Berke, A.G. Rinzler, B.R. Appleton, A.F. Hebard, High efficiency graphene solar cells by chemical doping, Nano letters, 12 (2012) 2745-2750.
[15] M. Li, C. Wang, Z. Chen, K. Xu, J. Lu, New concepts in electrolytes, Chemical reviews, 120 (2020) 6783-6819.
[16] G. Boschloo, A. Hagfeldt, Characteristics of the iodide/triiodide redox mediator in dye-sensitized solar cells, Accounts of chemical research, 42 (2009) 1819-1826.
[17] M. Wang, C. Grätzel, S.M. Zakeeruddin, M. Grätzel, Recent developments in redox electrolytes for dye-sensitized solar cells, Energy & Environmental Science, 5 (2012) 9394-9405.
[18] M. Grätzel, Solar energy conversion by dye-sensitized photovoltaic cells, Inorganic chemistry, 44 (2005) 6841-6851.
[19] S.O. Abdellatif, S. Josten, A.S.G. Khalil, D. Erni, F. Marlow, Transparency and Diffused Light Efficiency of Dye-Sensitized Solar Cells: Tuning and a New Figure of Merit, IEEE Journal of Photovoltaics, 10 (2020) 522-530.
[20] P. R. F. Barnes, K. Miettunen, X. Li, A. Y. Anderson, T. Bessho, M. Grätzel, B.C. O'Regan, Interpretation of Optoelectronic Transient and Charge Extraction Measurements in Dye-Sensitized Solar Cells, Advanced Materials 25 (2013) 1881–1922.

[21] S. Josten, T. Koehler, F. Marlow, Dye-sensitized solar cells on stainless steel, Solar Energy, 247 (2022) 346-354.
[22] F. Marlow, A. Hullermann, L. Messmer, Is the Charge Transport in Dye-Sensitized Solar Cells Really Understood?, Advanced Materials, 27 (2015) 2447-2452
[23] W. Schmickler, E. Santos, Interfacial Electrochemistry, Second Edition ed., Springer, 2010.
[24] A.J. Bard, L.R. Faulkner, ELECTROCHEMICAL METHODS: Fundamentals and Applications, Wiley New York, 1980.
[25] E.J. Dickinson, A.J. Wain, The Butler-Volmer equation in electrochemical theory: Origins, value, and practical application, Journal of Electroanalytical Chemistry, 872 (2020) 114145.
[26] R.G. Compton, C.E. Banks, Understanding voltammetry, World Scientific, 2018.
[27] R. Zhang, J.W. Weidner, Analysis of a gas-phase Br_2–H_2 redox flow battery, Journal of Applied Electrochemistry, 41 (2011) 1245-1252.
[28] S.O. Kasap, Principles of electronic materials and devices, McGraw-Hill New York, 2006.
[29] R.E. White, C.G. Vayenas, M.E. Gamboa-Aldeco, Modern Aspects of Electrochemistry, No. 45, Springer, 2009.
[30] S. Supramaniam, Fuel Cells: From Fundamentals to Applications, Springer Science \& Business media, 2006.
[31] I. Gorelov, S. Ryasenskii, S. Kartamyshev, M. Fedorova, A solid-state ion-selective electrode with an ionic-electronic transducer for determining chlordiazepoxide, Journal of Analytical Chemistry, 60 (2005) 65-69.
[32] P. Simon, Y. Gogotsi, Perspectives for electrochemical capacitors and related devices, Nature materials, 19 (2020) 1151-1163.
[33] L.L. Zhang, X. Zhao, Carbon-based materials as supercapacitor electrodes, Chemical society reviews, 38 (2009) 2520-2531.
[34] Brattain Walter, H.Gibney, R. B, Three-electrode circuit element utilizing semiconductor materials (Patent US2524034A), in, USA, 1948.
[35] P. Bergveld, Development of an ion-sensitive solid-state device for neurophysiological measurements, IEEE Transactions on biomedical engineering, (1970) 70-71.
[36] J.D. Yuen, A.S. Dhoot, E.B. Namdas, N.E. Coates, M. Heeney, I. McCulloch, D. Moses, A.J. Heeger, Electrochemical doping in electrolyte-gated polymer transistors, Journal of the American Chemical Society, 129 (2007) 14367-14371.
[37] R. Misra, M. McCarthy, A.F. Hebard, Electric field gating with ionic liquids, Applied Physics Letters, 90 (2007).
[38] J. Lee, M.J. Panzer, Y. He, T.P. Lodge, C.D. Frisbie, Ion gel gated polymer thin-film transistors, Journal of the American Chemical Society, 129 (2007) 4532-4533.
[39] H. Du, X. Lin, Z. Xu, D. Chu, Electric double-layer transistors: a review of recent progress, Journal of Materials Science, 50 (2015) 5641-5673.
[40] W. Cai, J. Wilson, A. Song, Present status of electric-double-layer thin-film transistors and their applications, Flexible and Printed Electronics, 6 (2021) 043001.
[41] D. Kimovski, N. Saurabh, M. Jansen, A. Aral, A. Al-Dulaimy, A.B. Bondi, A. Galletta, A.V. Papadopoulos, A. Iosup, R. Prodan, Beyond von neumann in the computing continuum: Architectures, applications, and future directions, IEEE Internet Computing, (2023).
[42] S. Kundu, P.B. Ganganaik, J. Louis, H. Chalamalasetty, B.P. Rao, Memristors Enabled Computing Correlation Parameter In-Memory System: A Potential Alternative to Von Neumann Architecture, IEEE Transactions on Very Large Scale Integration (VLSI) Systems, 30 (2022) 755-768.
[43] X. Zou, S. Xu, X. Chen, L. Yan, Y. Han, Breaking the von Neumann bottleneck: architecture-level processing-in-memory technology, Science China Information Sciences, 64 (2021) 160404.

[44] X. Huang, C. Liu, Y.-G. Jiang, P. Zhou, In-memory computing to break the memory wall, Chinese Physics B, 29 (2020) 078504.
[45] S. Mittal, A survey of ReRAM-based architectures for processing-in-memory and neural networks, Machine learning and knowledge extraction, 1 (2018) 75-114.
[46] P. Monalisha, A.P. Kumar, X.R. Wang, S. Piramanayagam, Emulation of synaptic plasticity on a cobalt-based synaptic transistor for neuromorphic computing, ACS Applied Materials & Interfaces, 14 (2022) 11864-11872.
[47] D. Marković, A. Mizrahi, D. Querlioz, J. Grollier, Physics for neuromorphic computing, Nature Reviews Physics, 2 (2020) 499-510.
[48] Z.W. Yibo Li, Rivu Midya, Qiangfei Xia and J Joshua Yang, Review of memristor devices in neuromorphic computing: materials sciences and device challenges, Journal of Physics D: Applied Physics, 51 (2018).
[49] C.D. Schuman, S.R. Kulkarni, M. Parsa, J.P. Mitchell, P. Date, B. Kay, Opportunities for neuromorphic computing algorithms and applications, Nature Computational Science, 2 (2022) 10-19.
[50] N.K. Upadhyay, H. Jiang, Z. Wang, S. Asapu, Q. Xia, J. Joshua Yang, Emerging memory devices for neuromorphic computing, Advanced Materials Technologies, 4 (2019) 1800589.
[51] D.B. Strukov, G.S. Snider, D.R. Stewart, R.S. Williams, The missing memristor found, nature, 453 (2008) 80-83.
[52] A. Sebastian, M. Le Gallo, R. Khaddam-Aljameh, E. Eleftheriou, Memory devices and applications for in-memory computing, Nature nanotechnology, 15 (2020) 529-544.
[53] C. Du, W. Ma, T. Chang, P. Sheridan, W.D. Lu, Biorealistic implementation of synaptic functions with oxide memristors through internal ionic dynamics, Advanced Functional Materials, 25 (2015) 4290-4299.
[54] M.U. Khan, J. Kim, M.Y. Chougale, C.M. Furqan, Q.M. Saqib, R.A. Shaukat, N.P. Kobayashi, B. Mohammad, J. Bae, H.-S. Kwok, Ionic liquid multistate resistive switching characteristics in two terminal soft and flexible discrete channels for neuromorphic computing, Microsystems & Nanoengineering, 8 (2022) 56.
[55] J.J. Yang, D.B. Strukov, D.R. Stewart, Memristive devices for computing, Nature nanotechnology, 8 (2013) 13-24.
[56] E. Mohamed, S. Josten, F. Marlow, A purely ionic voltage effect soft triode, Phys. Chem. Chem. Phys., 24 (2022) 8311–8320.
[57] I. Vourkas, G.C. Sirakoulis, Emerging memristor-based logic circuit design approaches: A review, IEEE circuits and systems magazine, 16 (2016) 15-30.
[58] K. Tybrandt, K.C. Larsson, A. Richter-Dahlfors, M. Berggren, Ion bipolar junction transistors, Proceedings of the National Academy of Sciences, 107 (2010) 9929–9932.
[59] F. Wang, P. Stepanov, M. Gray, C.N. Lau, M.E. Itkis, R.C. Haddon, Ionic liquid gating of suspended MoS2 field effect transistor devices, Nano Letters, 15 (2015) 5284-5288.
[60] Y. Hou, X. Hou, Bioinspired nanofluidic iontronics, Science, 373 (2021) 628-629.
[61] M.T. Ghoneim, M.M. Hussain, Review on Physically Flexible Nonvolatile Memory for Internet of Everything Electronics Electronics 4(2015) 424-479.
[62] R. Waser, R. Dittmann, G. Staikov, K. Szot, Redox-Based Resistive Switching Memories –Nanoionic Mechanisms, Prospects, and Challenges, Advanced Materials, 21 (2009) 2632-2663.
[63] E. Madai, B. Matejczyk, A. Dallos, M. Valisko, D. Boda, Controlling ion transport through nanopores: modeling transistor behavior, Physical Chemistry Chemical Physics, 20 (2018) 24156--24167.
[64] H. Zhang, C. Cheng, H. Zhang, R. Chen, B. Huang, H. Chen, W. Pei, Physical mechanism for the synapse behaviour of WTiOx-based memristors, Phys. Chem. Chem. Phys. , 21 (2019) 23758-23763.

[65] H.-S.P. Wong, S. Salahuddin, Memory leads the way to better computing, Nature nanotechnology, 10 (2015) 191-194.
[66] V.K. Sangwan, M.C. Hersam, Neuromorphic nanoelectronic materials, Nature nanotechnology, 15 (2020) 517-528.
[67] Y. Shan, Z. Lyu, X. Guan, A. Younis, G. Yuan, J. Wang, S. Lia, T. Wu, Solution-processed resistive switching memory devices based on hybrid organic–inorganic materials and composites, Phys.Chem.Chem.Phys., 20 (2018) 23837-23846.
[68] W. Zhang, R. Mazzarello, M. Wuttig, E. Ma, Designing crystallization in phase- change materials for universal memory and neuro- inspired computing Nature, 4 (2019) 150-168.
[69] S. Menzel, S. Tappertzhofen, R. Waserab, I. Valov, Switching kinetics of electrochemical metallization memory cells, Phys.Chem.Chem.Phys., 15 (2013) 6945-6952.
[70] Z. Wang, K.L. Wang, H. Wu, Q. Xia, G.W. Burr, J.J. Yang, C.S. Hwang, Resistive switching materials for information processing Nature reviews, 5 (2020) 173-195.
[71] A. Chen, Solid state electrochemistry II: electrodes, interfaces and ceramic membranes, John Wiley & Sons, 2012.
[72] T. Kamsma, W. Boon, T. ter Rele, C. Spitoni, R. van Roij, Iontronic Neuromorphic Signaling with Conical Microfluidic Memristors, Physical Review Letters, 130 (2023) 268401.
[73] Frank Marlow, Elalyaa Mohamed, S. Josten, Ionic Voltage Effect Triode Cell, in: E.P.A.N. EP22155655.8 (Ed.), 2022.
[74] S. Josten, Farbstoffsensibilisierte Solarzellen auf Edelstahlsubstraten, Fakultät für Chemie der Universität Duisburg-Essen (2024).
[75] S. Abdellatif, S. Josten, P. Sharifi, K. Kirah, R. Ghannam, A.S.G. Khalil, D. Erni, F. Marlow, Optical investigation of porous TiO_2 in mesostructured solar cells, in, International Society for Optics and Photonics, 2018, pp. 105260A.
[76] E. Mohamed, N. Tchorz, F. Marlow, Iontronic memories based on ionic redox systems: operation protocols, Faraday Discussions, 246 (2023) 296-306.
[77] K. Fan, M. Liu, T. Peng, L. Ma, K. Dai, Effects of paste components on the properties of screen-printed porous TiO_2 film for dye-sensitized solar cells, Renewable Energy, 35 (2010) 555-561.
[78] S. Chung, K. Cho, T. Lee, Recent progress in inkjet-printed thin-film transistors, Advanced science, 6 (2019) 1801445.
[79] J. Fan, C. Montemagno, M. Gupta, 3D printed high transconductance organic electrochemical transistors on flexible substrates, Organic Electronics, 73 (2019) 122-129.
[80] S. Chen, A. Surendran, X. Wu, S.Y. Lee, M. Stephen, W.L. Leong, Recent technological advances in fabrication and application of organic electrochemical transistors, Advanced Materials Technologies, 5 (2020) 2000523.
[81] J.-Y. Lee, J. An, C.K. Chua, Fundamentals and applications of 3D printing for novel materials, Applied materials today, 7 (2017) 120-133.
[82] N. Shahrubudin, T.C. Lee, R. Ramlan, An overview on 3D printing technology: Technological, materials, and applications, Procedia Manufacturing, 35 (2019) 1286-1296.
[83] https://shop.bb-sensors.com/en/Humidity/Humidity-sensors/Electrolytic-humidity-sensor-EFS-10.html.
[84] P. Horowitz, W. Hill, The art of electronics, Cambridge Univ. Press, 1989.
[85] H. Yuan, H. Shimotani, A. Tsukazaki, A. Ohtomo, M. Kawasaki, Y. Iwasa, High-Density Carrier Accumulation in ZnO Field-Effect Transistors Gated by Electric Double Layers of Ionic Liquids, Advanced Functional Materials, 19 (2009) 1046-1053.
[86] L. Herlogsson, X. Crispin, N.D. Robinson, M. Sandberg, O.J. Hagel, G. Gustafsson, M. Berggren, Low-voltage polymer field-effect transistors gated via a proton conductor, Advanced Materials, 19 (2007) 97-101.

[87] S. Srinivasan, Fuel cells: from fundamentals to applications, Springer Science & Business media, 2006.
[88] X.G. Zhang, Electrochemistry of Silicon and its Oxide, Springer 2007.
[89] J. Akilavasan, F. Marlow, Electrochemical Impedance Spectroscopy at Redox-Type Liquid|Liquid Interfaces: The Capacitance Lag, The Journal of Physical Chemistry C, 124 (2020) 4101-4108.
[90] A. Chhetry, J. Kim, H. Yoon, J.Y. Park, Ultrasensitive interfacial capacitive pressure sensor based on a randomly distributed microstructured iontronic film for wearable applications, ACS Applied Materials & Interfaces, 11 (2018) 3438-3449.
[91] B. Nie, R. Li, J. Cao, J.D. Brandt, T. Pan, Flexible Transparent Iontronic Film for Interfacial Capacitive Pressure Sensing, Advanced Materials, 27 (2015) 6055-6062.
[92] P. Zhang, M. Xia, F. Zhuge, Y. Zhou, Z. Wang, B. Dong, Y. Fu, K. Yang, Y. Li, Y. He, Nanochannel-based transport in an interfacial memristor can emulate the analog weight modulation of synapses, Nano Letters, 19 (2019) 4279-4286.
[93] B. Sun, S. Ranjan, G. Zhou, T. Guo, C. Du, L. Wei, Y.N. Zhou, Y.A. Wu, A True Random Number Generator Based on Ionic Liquid Modulated Memristors, ACS Applied Electronic Materials, 3 (2021) 2380-2388.
[94] E. Frackowiak, M. Meller, J. Menzel, D. Gastol, K. Fic, Redox-active electrolyte for supercapacitor application, Faraday Discussions, 172 (2014) 179-198.
[95] E. Mohamed, F. Marlow, Ionic voltage effect soft pentode, (2024) manuscript.
[96] A. Hartridge, M.G. Krishna, A. Bhattacharya, A study of nanocrystalline CeO_2/PrOx optoionic thin films: temperature and oxygen vacancy dependence, Materials Science and Engineering: B, 57 (1999) 173-178.
[97] A. Senocrate, E. Kotomin, J. Maier, On the way to optoionics, Helvetica Chimica Acta, 103 (2020) e2000073.
[98] F. Podjaski, B.V. Lotsch, Optoelectronics meets optoionics: Light storing carbon nitrides and beyond, Advanced Energy Materials, 11 (2021) 2003049.
[99] H. Kasap, C.A. Caputo, B.C. Martindale, R. Godin, V.W.-h. Lau, B.V. Lotsch, J.R. Durrant, E. Reisner, Solar-driven reduction of aqueous protons coupled to selective alcohol oxidation with a carbon nitride–molecular Ni catalyst system, Journal of the American Chemical Society, 138 (2016) 9183-9192.
[100] G.Y. Kim, A. Senocrate, T.-Y. Yang, G. Gregori, M. Grätzel, J. Maier, Large tunable photoeffect on ion conduction in halide perovskites and implications for photodecomposition, Nature materials, 17 (2018) 445-449.
[101] B. Chen, Z. Suo, Optoionic Sensing, Small, 18 (2022) 2103882.
[102] J. Cai, W. Zhang, L. Xu, C. Hao, W. Ma, M. Sun, X. Wu, X. Qin, F.M. Colombari, A.F. de Moura, Polarization-sensitive optoionic membranes from chiral plasmonic nanoparticles, Nature nanotechnology, 17 (2022) 408-416.
[103] F. Sun, Q. Lu, L. Liu, L. Li, Y. Wang, M. Hao, Z. Cao, Z. Wang, S. Wang, T. Li, Bioinspired flexible, dual-modulation synaptic transistors toward artificial visual memory systems, Advanced Materials Technologies, 5 (2020) 1900888.
[104] X.-Y. Yin, Y. Zhang, X. Cai, Q. Guo, J. Yang, Z.L. Wang, 3D printing of ionic conductors for high-sensitivity wearable sensors, Materials Horizons, 6 (2019) 767-780.
[105] S. Cohen-Cory, The developing synapse: construction and modulation of synaptic structures and circuits, Science, 298 (2002) 770-776.
[106] C. Li, T. Xiong, P. Yu, J. Fei, L. Mao, Synaptic iontronic devices for brain-mimicking functions: Fundamentals and applications, ACS Applied Bio Materials, 4 (2020) 71-84.
[107] B. Barbour, N. Brunel, V. Hakim, J.-P. Nadal, What can we learn from synaptic weight distributions?, TRENDS in Neurosciences, 30 (2007) 622-629.

[108] T. Guo, J. Ge, B. Sun, K. Pan, Z. Pan, L. Wei, Y. Yan, Y.N. Zhou, Y.A. Wu, Soft biomaterials based flexible artificial synapse for neuromorphic computing, Advanced Electronic Materials, 8 (2022) 2200449.
[109] L.G. Appelbaum, M.A. Shenasa, L. Stolz, Z. Daskalakis, Synaptic plasticity and mental health: Methods, challenges and opportunities, Neuropsychopharmacology, 48 (2023) 113-120.
[110] D.V. Buonomano, W. Maass, State-dependent computations: spatiotemporal processing in cortical networks, Nature Reviews Neuroscience, 10 (2009) 113-125.
[111] Y. Park, M.-K. Kim, J.-S. Lee, 2D layered metal-halide perovskite/oxide semiconductor-based broadband optoelectronic synaptic transistors with long-term visual memory, Journal of Materials Chemistry C, 9 (2021) 1429-1436.
[112] F. Liao, Z. Zhou, B.J. Kim, J. Chen, J. Wang, T. Wan, Y. Zhou, A.T. Hoang, C. Wang, J. Kang, Bioinspired in-sensor visual adaptation for accurate perception, Nature Electronics, 5 (2022) 84-91.
[113] L. Gu, S. Poddar, Y. Lin, Z. Long, D. Zhang, Q. Zhang, L. Shu, X. Qiu, M. Kam, A. Javey, A biomimetic eye with a hemispherical perovskite nanowire array retina, Nature, 581 (2020) 278-282.
[114] H. Tan, G. Liu, H. Yang, X. Yi, L. Pan, J. Shang, S. Long, M. Liu, Y. Wu, R.-W. Li, Light-gated memristor with integrated logic and memory functions, ACS nano, 11 (2017) 11298-11305.
[115] H. Han, Z. Xu, K. Guo, Y. Ni, M. Ma, H. Yu, H. Wei, J. Gong, S. Zhang, W. Xu, Tunable synaptic plasticity in crystallized conjugated polymer nanowire artificial synapses, Advanced Intelligent Systems, 2 (2020) 1900176.
[116] S. Royer, D. Paré, Conservation of total synaptic weight through balanced synaptic depression and potentiation, Nature, 422 (2003) 518-522.
[117] J.H. Byrne, R.D. Hawkins, Nonassociative learning in invertebrates, Cold Spring Harbor perspectives in biology, 7 (2015) a021675.
[118] M. Di Ventra, MemComputing: fundamentals and applications, Oxford University Press, 2022.

7. Appendices

Appendix A: List of abbreviations and symbols

IVEST	Ionic Voltage Effect Soft Triode
CPU	Central processing unit
ALU	Arithmetic logic unit
R_{BB}	Resistance between the two bottom electrodes
V_{BB}	Voltage between the two bottom electrodes
V_{top}	Voltage on the top electrode
J_{Top}	Top electrode current (input current)
J_{BB}	Current between the two bottom electrodes (Output current)
X_{TiO2}	Number of TiO_2 layers on the top electrode
X_e	Dilution factor of the electrolyte
SYM-BB	Symmetric BB configuration
LIC	Low input current
$\boldsymbol{g_m}$	Differential transconductance
$\boldsymbol{\gamma_{BB}}$	Specific transconductance
WP	Working point
$\beta_{\boldsymbol{d,WP}}$	Amplification at a specific working point
$\boldsymbol{G_{BB}}$	Conductance between the two bottom electrodes
$\boldsymbol{G_{d,top}}$	Differential conductance of the top electrode
HRS	High resistance State
LRS	Low resistance state
$\boldsymbol{\alpha}$	Memory contrast
$\boldsymbol{\tau_1}$	Adaptation time
$\boldsymbol{\tau_2}$	Stability time

$\boldsymbol{d_p}$	Membrane pore size
$\boldsymbol{d}$	Distance between the electrodes

Appendix B: List of figures

Appendix C: ELNA entries

FIGURE, TABLES, PROCEDURES	LAB JOURNAL CODE
Figure 2.2	MOF-MA-417, 189 and MLW-PE016
Figure 2.9	MLW-PD-097
Figure 2.11B	UNA-UA-218
Figure 2.13 and 2.14	MOF-MA-030
Figure 2.15 and 2.16	MOF-MA-027
Figures 2.17 and 2.18	MOF-MA-111
Figures 2.20, 2.21,2.22 and 2.23	MOF-MA-156
Figure 2.26 and 2.27	MOF-MA-249 to 262
Figure 2.28	MOF-MA-271 to 274
Figure 2.30	MOF-MA-285
Figure 2.31	MOF-MA-271 to 276
Figure 2.34	MOF-MA-285
Figure 2.35	MOF-MA-404-02
Figure 2.36	MOF-MA-285
Fabrication method A	MOF-MA-014
Fabrication method B	MLW-AC-148.1
Figure 3.1	MOF-MA-382-01
Figure 3.4	MOF-MA-382-10
Figure 3.6	MOF-MA-382-08
Figure 3.7	MOF-MA-382-14
Figure 3.9	MOF-MA-382-03
Figure 3.11	MOF-MA-418-03
Figure 3.12	MOF-MA-396-04
Figure 3.13	MOF-MA-407-01
Figure 3.14	MOF-MA-396-03
Table 3.4, 3.5 and 3.6	MOF-MA-382
Figure 4.5	MOF-MA-418
Figure 4.6A	MOF-MA-423
Figure 4.6B	MOF-MA-429

Figure 4.8	MOF-MA-423
Figure 4.9	MOF-MA-416-04
Figure 4.10	MOF-MA-392
Figure 4.11	MOF-MA-432
Figure 4.13	MOF-MA-431
Table 4.2 and 4.3	MOF-AM-392-03

Appendix D: Fabrication details and Amplification Calculations

Most of the content of this Appendix was published as "A purely ionic voltage effect soft triode" supplementary information. Mohamed, E., Josten, S., & Marlow, F. (2022) Phys. Chem.Chem. Phys, 24(14), 8311-8320. The main part of the text, as well as the figures of the following section, are reprinted and reproduced

SD-1) Fabrication details of the (non-optimized method)

Fig. SD-1 shows the IVEST after a large number of electrical measurements. Its appearance has not changed by the measurements.

Table SD-1 Special samples. In addition, systematic variations of the X and d parameters have been made (not shown in the table).

Sample type	**Remark**	X_e	X_{TiO2}	d_S / µm	**Sample numbers**
Ib19	basic sample type 2019	1	1	150	156, 156, 169, 174, 177, 180, 217, 237, 242, 271
IoA	optimum sample for amplification	0.6	1	150	274
IoM	optimum sample for a memory	0.16	0.5	1.2	285

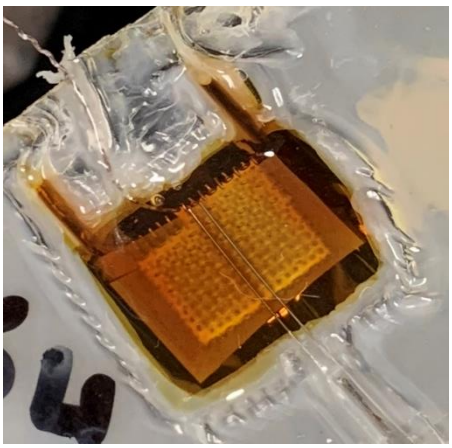

Fig. SD-1 Optical picture of an IVEST. MOF-MA-264 [56]

Table SD-2 Comparison of different samples

Sample	R_{BB} / kΩ	G_{BB} / mS	g_{BB}/ mS/V
156	1.17	0.85	0.43
169	0.87	1.15	0.32
174	1.35	0.74	0.49
177	1.3	0.77	0.48
180	1.34	0.74	0.49
217	0.87	1.15	0.32
237	0.84	1.19	0.31
242	1.23	0.81	0.45
271	0.82	1.22	0.30

SD-2) Device symmetry and reproducibility

a) Device symmetry. For all measurements, we have used a sym-BB configuration. To test the symmetry of the device, the same measurements were done with positive and negative V_{BB}. Fig. SD-2 shows the comparison and reveals a good device symmetry

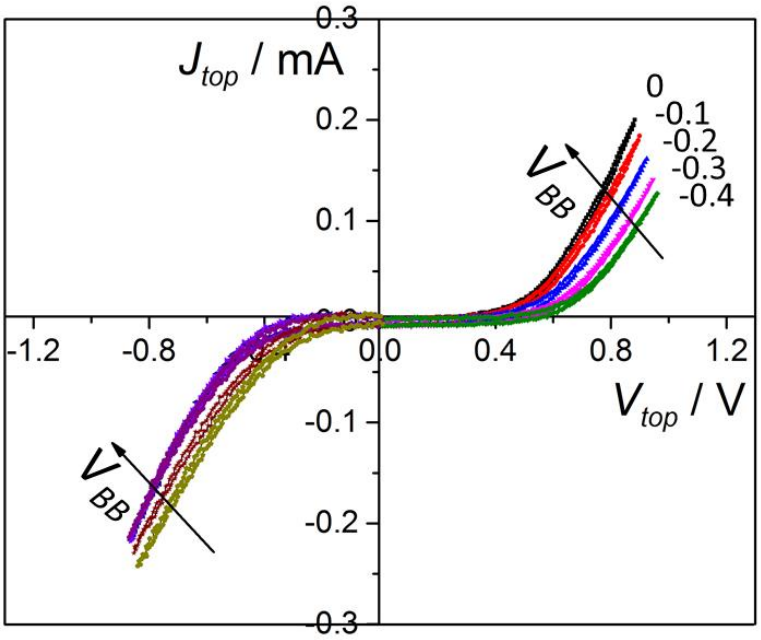

Fig. SD-2 Symmetric-BB-*JV* input characterization at negative read-out voltages. The top electrode was connected to the *JV* analyzer. Fixed V_{BB} voltages were applied between -0.4 V and 0 V as indicated by the curve labels (investigated IVEST: 156). [56]

b) Reproducibility. All the measurements were repeated several times with different samples. All samples with same fabrication conditions have shown qualitatively the same behavior at all characterization methods. There was a clear nonlinear dependence of the input current from the

input voltage V_{top} and a week dependence of the input current from V_{BB}. For the output measurements, all the samples have shown an increase in R_{BB} by increasing V_{top} as shown in Fig. SD-3.

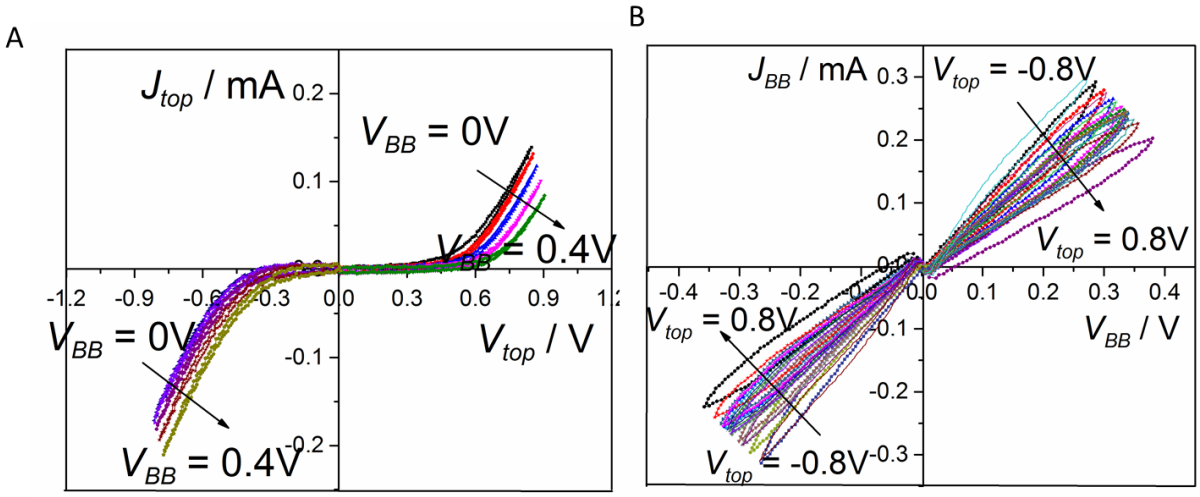

Fig. SD-3 Another example of an IVEST device (Sample 177). (A) Sym-BB input characteristics. The top electrode was connected to the *JV* analyzer and fixed V_{BB} values were applied from 0 V to 0.4 V. (B) Sym-BB output characteristics. V_{BB} was scanned by the *JV* device while fixed values of V_{top} were applied from -0.8 V to 0.8 V. [56]

The following table shows different samples with same fabrication conditions (where $X_e = 1$, $X_{TiO2} = 1$) at WP1. Fabrication fluctuations induce some differences in the resistance (± 20%) and in the transfer parameter (± 20%).

SD-3) Amplification Calculations

a) General Formula. Differences of our device to standard transistors are the offset of the output current and the highly nonlinear characteristics. Therefore, the description by a modified parameter seems to be more appropriate than the standard description by amplification. Here, the differential amplification factor

$$\beta_{d,WP} = \frac{\partial J_{out}}{\partial J_{in}} \qquad \text{(SD-1)}$$

is used. It describes the small signal behavior and it equals the normal amplification factor for the transistor having a nearly linear transfer characteristics. From the different amplification factors used for transistors, the factor for the common-emitter configuration is the nearest

analogue. Since the IVEST output is nearly ohmic, it is useful to re-write the output current as

$$J_{BB} = \frac{V_{BB}}{R_{BB}} = V_{BB} G_{BB} \quad \text{(SD-2)}$$

leading to the differential

$$\partial J_{BB} = V_{BB} \gamma_{BB} \, \partial V_{top} \quad \text{(SD-3)}$$

with the specific differential transconductance

$$\gamma_{BB} = \frac{\partial G_{BB}}{\partial V_{top}} \quad \text{(SD-4)}$$

This definition is equivalent to the eqn 1 and 2 in the main text. Moreover, using the definition of the differential conductance of the top electrode one finds:

$$\partial J_{top} = G_{d,top} \, \partial V_{top} \quad \text{(SD-5)}$$

Here, one should underline that this differential conductance is strongly voltage dependent. Combining eq S1, S3 and S4 the final result is obtained:

$$\beta_{d,WP} = \gamma_{BB}(V_{top}) \frac{V_{BB}}{G_{d,top}(V_{top})} \quad \text{(SD-6)}$$

For explicit calculation, we chose the working point WP1: V_{top}= -0.37 V, V_{BB}= 0.25 V. This working point results in the highest amplification among our data. It is a compromise of maximizing γ_{BB} (big G_{BB} slope) and minimizing $G_{d,top}$.

b) Differential conductance. To determine the differential conductance, the setup in Fig. S4A was used. The J_{top} values one gets from:

$$J_M = U_M / (R_M (U_o - U_M)) \quad \text{(SD-7)}$$

The resulting curve can be fitted with a parabolic curve as shown in Fig S4B. To determine the differential conductance at the working point WP1 = -0.37 V, the tangent at the averaging curve (black curve in Fig. S4B) was used resulting in 0.0217 mS.

c) Amplification calculation. The specific differential transconductance γ_{BB} can be determined from Fig. SD-3A. At working point WP1 it results in an amplification of

$$\beta = \gamma_{BB}(V_{top}) \frac{V_{BB}}{G_d(V_{top})}$$

$$\beta_{d,WP1} = (-4.57 \frac{\text{mS}}{\text{V}})(\frac{0.25V}{-0.0217\text{mS}}) \text{ = -52.6}$$

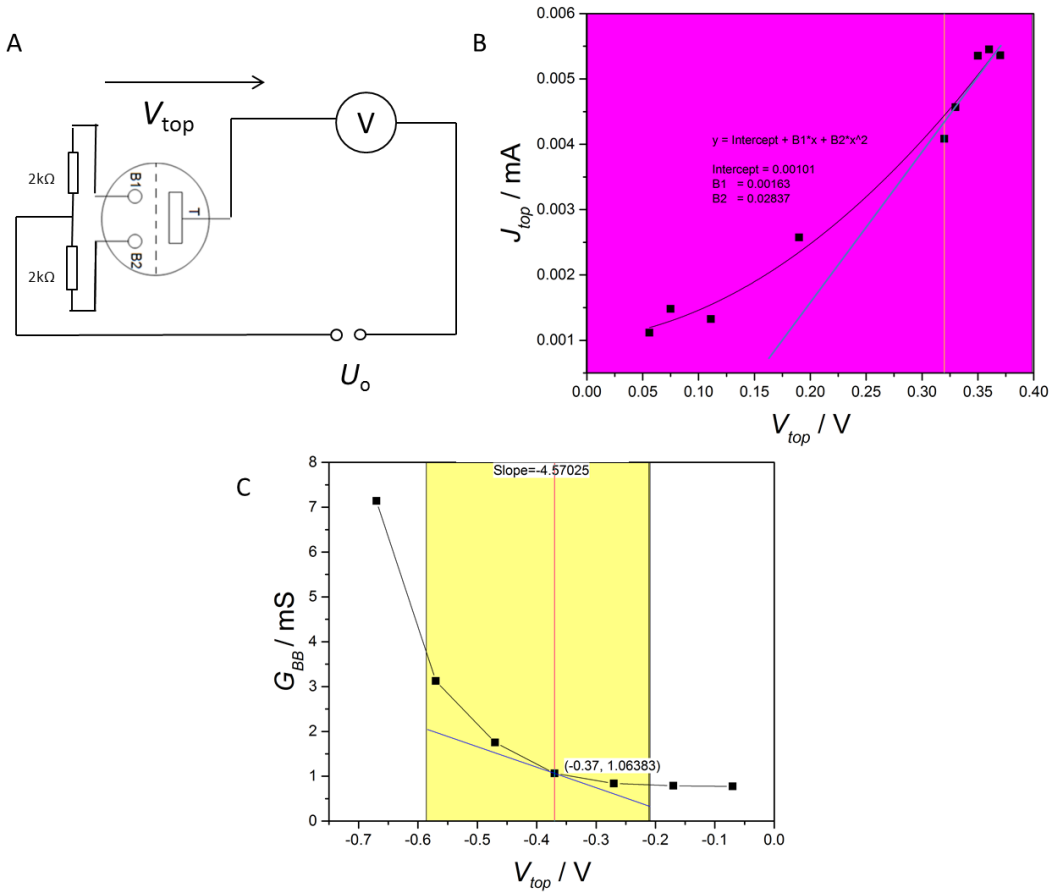

Fig. SD-4 (A) Set-up used to measure R_{sh}. The inner resistance of the *V*-meter was 10 MOhm. (B) Relation between J_{top} and V_{top}, and a parabolic curve fitted by Origin. The black curve is an average determined by Origin with function Y = intercept+B1X+B2X^2. (C) The dependence of G_{BB} from V_{top} measured for the IVEST device 274. The specific differential transconductance was calculated using the tangent function at WP1 (at $V_{top} = -0{,}37$ V, $V_{BB} = 0.25$ V) with Origin [56]

Appendix E: Adaptation and stability time calculations

Most of the content of this Appendix was published as "A purely ionic voltage effect soft triode" supplementary information. Mohamed, E., Josten, S., & Marlow, F. (2022) Phys. Chem.Chem. Phys, 24(14), 8311-8320. The main part of the text, as well as the figures of the following section, are reprinted and reproduced

Adaptation and stability time calculations

Two meta-stable states are visible in the measurements. They represent the high resistance state (HRS) and low resistance state (LRS). After long times both states are assumed to reach the same resistance R_{BB}^{∞}. It is also assumed that the two states have the same characteristic time τ_2 describing the slow processes. This is considered in the following fitting formulas:

$$L(t) = A_1^L e^{-t/\tau_1^L} + A_2^L e^{-t/\tau_2} + R_{BB}^{\infty} \quad \text{(SE-1)}$$

$$H(t) = A_1^H e^{-t/\tau_1^H} + A_2^H e^{-t/\tau_2} + R_{BB}^{\infty} \quad \text{(SE-2)}$$

To avoid the simultaneous fitting of two data sets, the problem is converted to a sequential fitting process for the difference and the sum of the two resistance data. The value for τ_2 is found from fitting the difference with:

$$H(t) - L(t) = A_1^D e^{-t/\tau_1^D} + A_2^D e^{-t/\tau_2} \quad \text{(SE-3)}$$

The value for R_{BB}^{∞} is found from fitting the sum using the pre-determined value for τ_2:

$$H(t) + L(t) = A_1^S e^{-t/\tau_1^S} + A_2^S e^{-t/\tau_2} + 2R_{BB}^{\infty} \quad \text{(SE-4)}$$

Eqn S8 and S9 represent the exponential decay at the adaptation and stability time in each state.

Origin2015G was used to analyze the appearing times of the memory states quantitatively as shown in Fig. S4. The fitting of eqn S10 and S11 to the measured data resulted in the adaptation time where $\tau_1 < 2$ min and in the stability time with $\tau_2 > 2$ min. The time τ_2 resulting from eqn S10 was used as a constant in eqn S11 to calculate R_{BB}^{∞}.

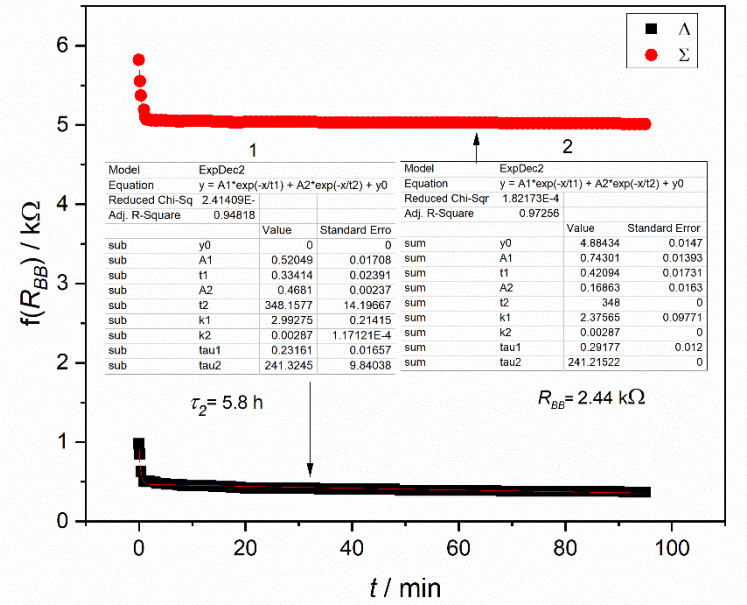

Fig. SE-1 Analysis of the metastable states. The sum and the difference of the resistance are fitted using Origin2015G. Two characteristic times can be concluded as described in the text. Investigated sample: 285 [56]

Appendix F: S2 switch

This special switch we called S2 was used starting from chapter 3. A special electronic circuit was used to build a switch with a timer as shown in Figure SF-1This special switch was used to define the charge amount that is injected in every resistance measurement to a fixed amount. It limited the reading time to 1.5 s.

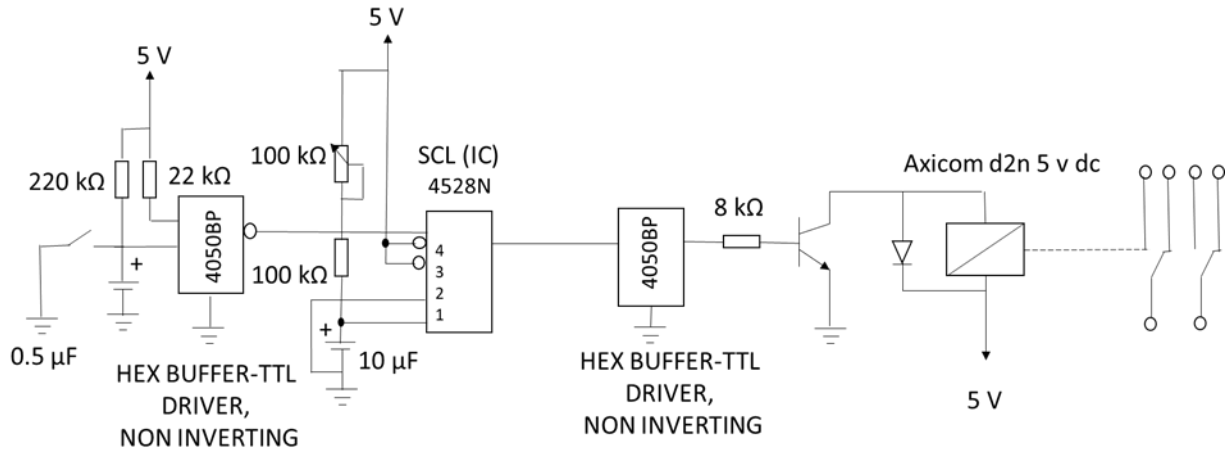

Fig. SF-1 Schematic description of the electronic circuit used to build switch S2.

List of publications

1) Marlow, F.; Mohamed, E.; Josten, S., Ionic Voltage Effect Triode Cell, in: E.P.A.N. EP22155655.8 (Ed.), 2022
   Contribution to this patent: Experimental work and part of the writing.

2) Mohamed, E.; Josten, S.; Marlow, F., A purely ionic voltage effect soft triode. Phys. Chem. Chem. Phys. 2022, 24 (14), 8311-8320.
   Contribution to this paper: Experimental work, and most of the writing.

3) Mohamed, E., Tchorz, N., & Marlow, F. Iontronic memories based on ionic redox systems: Operation protocols. Faraday Discussions. 2023, (246). 296-306
   Contribution to this paper: Experimental work, and most of the writing.

4) Mohamed, E., & Marlow, F. Opto-ionic voltage effect soft triode: An optical-to-ionic signal converter, Advanced Materials Technologies (2024), 2400685
   Contribution to this paper: Experimental work, and most of the writing.

5) Mohamed, E., in: "Iontronic dynamics: general discussion." Faraday Discussions 246 (2023): 322-355. Contains the discussion in the Faraday conference.

DOI: 10.17185/duepublico/82377
URN: urn:nbn:de:hbz:465-20240830-105507-7